1994

An examination of triassic cyclostratigraphy in the Newark Basin from shallow seismic profiles and geophysical logs

Gregory S. Baker
Lehigh University

AUTHOR:

Baker, Gregory S.

TITLE:

An Examination of Triassic Cyclostratigraphy in the Newark Basin from Shallow Seismic Profiles and Geophysical Logs

DATE: May 29, 1994

AN EXAMINATION OF TRIASSIC CYCLOSTRATIGRAPHY IN THE NEWARK BASIN FROM SHALLOW SEISMIC PROFILES AND GEOPHYSICAL LOGS

by

Gregory S. Baker

A Thesis

Presented to the Graduate Committee

of Lehigh University

in Candidacy for the Degree of

Master of Science

in

Geological Sciences

Lehigh University

1994

This thesis is accepted and approved in partial fulfillment of the requirements for the degree of Master of Science.

5/17/94

(date)

Advisor

Chair of Department

Acknowledgements

The most important contributor to my education during tenure as a graduate student at Lehigh was my advisor, Anne Meltzer. Her high expectations forced me to strive for and achieve an high quality of work. I also would not have enjoyed and survived my stay at Lehigh were it not for the constant intellectual (and not-so-intellectual) interactions with my peers and elders, including, but not exclusively, Norm, Julie, Andrew, Tina, Jodie, Ken, Amy, Spigot-head, Newf, Ed, Kris, Lori, Bobb, Lori, P.B., Jeff & Marci, H, Richard, the brothers of Phi Sig, Kyle, Lauren, Ma, Pop, and the folks from home. I must also mention that the ride would have been much more treacherous were it not for the frequent favors and assistance of Nancy, Laurie, George & Scott. Thanks all.

Table of Contents

List of Figures

List of Tables

Abstract

During the early Mesozoic breakup of Pangea a series of rift basins formed along the eastern coast of present-day North America. The Newark Basin in New York, Pennsylvania, and New Jersey, is the largest of these Triassic rift basins. The equatorial location and monsoonal climate of the Newark Rift Basin during the Triassic provided the setting for orbital forcing functions to effect climate, which in turn effected lake levels, and the associated sedimentary facies, within the basin . The Newark Basin Drilling Project, run by Lamont-Doherty Earth Observatory in 1991, drilled six cores throughout the Newark Basin to collect a continuous stratigraphic section of the Triassic rocks. Several shallow seismic profiles in the vicinity of the Titusville, Nursery Road, and Princeton coring sites were to be used to examine the lateral continuity of facies between the cores. However, a complex near-surface weathering zone prevented successful imaging of coherent reflections. Synthetic seismograms generated from geophysical logs collected at these same core sites demonstrate that there is relatively high reflectivity in the subsurface at these locations. The synthetics suggest that if the near-surface problem is overcome, good shallow seismic profiles can be collected. Cyclostratigraphy within the Newark Basin, consisting of Van Houten cycles of 21,000 years, the associated beat cycles of 100,000 and 400,000 years, and the obliquity cycle of 41,000 years are observed in spectral analyses of reflectivity series from the Titusville, Nursery Road and Princeton geophysical logs. High reflectivity is correlated to the transition from the low velocity thick, black shale sequences, representing the deepest-water facies, to the higher velocity shallow water/playa facies. The sedimentation rates within the Newark Basin, estimated by fixing the 413 ky cycle peaks of the reflectivity series, show variation between 0.5643 ft/ky and 0.9416 ft/ky during its 25 My history, but an overall average of 0.7316 ft/ky agrees with the rate of 0.7283 ft/ky used in this study and previously in the literature.

Introduction

During the Triassic breakup of the supercontinent Pangea, several rift basins were formed along the eastern coast of North America (**Figure 1**). The Newark Basin of New York, New Jersey, and Pennsylvania is the largest and best exposed of these Triassic rift basins (**Figure 2**). The Triassic sequence within the basin consists of three main, non-marine stratigraphic units. The basal unit is the fluvial-deltaic Stockton Formation. The middle unit is the Lockatong Formation, consisting of deep water lacustrine mudstones. The Passaic Formation, composed of shallow water lacustrine facies, is the uppermost unit. These Triassic strata show a cyclicity related to changes in lake level caused by climate modulation which was, in turn, induced by orbital forcing (Olsen, 1986). The lake level fluctuation due to climatic change correspond to periods of roughly 21,000, 41,000, 100,000, 400,000 and 2,00,000 years (Olsen, submitted).

The purpose of this study is to examine Triassic Cyclostratigraphy within the Newark Basin. Two geophysical methods are used. First, geophysical logs from three core locations within the basin are examined to determine reflectivity (by generating synthetic seismograms from the sonic and density logs) and look for evidence of cyclicity at these borehole sites. Second, five high-resolution seismic reflection profiles collected at the borehole sites are used to examine the seismic expression of the stratigraphy at the sites.

The results of this study demonstrate: 1) A complex near-surface layer makes seismic imaging difficult; 2) Synthetic seismograms generated from the

geophysical logs demonstrate that boundaries between members of the Passaic, Lockatong and Stockton Formations typically are good reflecting interfaces; and 3) Analysis of reflectivity series generated from the borehole geophysical logs, demonstrates that cyclicity matches orbital forcing functions, including the 41,000 year cycle of obliquity, and sedimentation rates at the borehole sites average to 0.7283 ft/ky (22.3 cm/ky).

Geological Setting

During the Triassic, there was only one major continent, Pangea, more or less symmetrically distributed about the equator but extending from pole to pole (**Figure 3**). The breakup of Pangea during the Triassic numerous rift basins to form along the present-day coast of North America. Included among these rift basins is the Newark Rift Basin. Paleomagnetic studies indicate the Newark Basin was centrally located in Pangea, at about 3.5° north paleolatitude during the initial stages of deposition, and drifted north more than 10° during the Triassic (Kent and Olsen, 1992).

The rocks in the Newark Rift Basin (the Newark Supergroup) form a classic half-graben, bounded to the northeast by a series of basinward-dipping normal faults (the border fault system), and otherwise lay unconformably on older Paleozoic strata (Schlische and Olsen, 1988). Several intrabasinal faults and transverse folds are observed in the basin. At least some of the internal faulting and folding appears to be synchronous with deposition (Schlische and Olsen, 1988; Olsen et al., 1989).

The lacustrine and fluvial-deltaic strata of the Newark Supergroup dip, on average, 5° to 15° toward the boarder fault system (Schlische, 1990; **Figure 4**),

so that sequentially older strata crop out away from the boarder fault. The Triassic stratigraphic section is marked by two distinct depositional patterns, a lower fluvial deltaic section and an upper lacustrine section (Schlische and Olsen, 1990), which record 25 My of late Triassic development of the Newark Basin.

The lower section is a sequence of red and brown fluvially deposited sands, named the Stockton Formation. This lower sequence contains features typical of a hydrologically open basin (Olsen, 1988). The Stockton is characterized by basinwide channel systems and large- to small-scale lenticular bedding (Schlische and Olsen, 1990). Additionally, conglomeratic intervals that can span the basin, and paleocurrent patterns that are often axial or that are dominated by one direction across the basin (indicating through-going drainage), are present (Schlische and Olsen, 1990). There is an absence of evidence for the formation of large lakes within the Newark Basin during the deposition of the Stockton Formation, although some pond or paludal deposits have been found (Schlische and Olsen, 1990).

The upper section is composed of deep water lacustrine mudstones, (representing, in some instances, lake depths in excess of 120 m), and shallow-water/marginal lacustrine mudstones, representing the Lockatong and Passaic Formations, respectively (Olsen, 1986). This second depositional pattern is typical of a hydrologically closed basin system, and is characterized by: a systematic increase in grain size toward all basin boundaries, paleocurrent patterns directed away from the basin's boundaries, local provenance of coarse-grained strata near the basin margins, the presence of evaporites, and cyclicity of fine-grained sedimentary rocks in the central portion of the basin (Schlische and Olsen, 1990). Within the central basin, cyclical lacustrine beds

have considerable lateral continuity, while the basin margins are dominated by deposits of fluvial-deltaic sequences and alluvial fans (Olsen, 1988).

Cyclostratigraphy

Tectonic processes were responsible for the geometry of the Newark Basin, which controlled the maximum attainable lake depth during the basin's history. However, high-frequency fluctuations in lake depth (relative to a tectonic time scale) were largely controlled by climate (Olsen, 1988). The depositional environment of the Newark Basin during the early Mesozoic was influenced by the arrangement of land masses, the geographic location of the basin and global climatic conditions.

The climatic conditions during the depositional phase of the Newark Basin are described as "hot house", with no evidence of polar ice (Frakes and Francis, 1988), and deposition of coals in sub-polar regions (Cornet and Olsen, 1992). These climatic conditions led to the development of strong monsoonal weather patterns similar to that of equatorial Africa today (Kutzback and Street-Perrott, 1985). Several authors have argued for a "super-monsoonal" climate system of equatorial Pangea which affected lake levels within the Newark Basin (Crowley and North, 1991; Crowley et al., 1992). Orbital forcing effects upon the "super monsoonal" system involved changes in the intensity of maximum insolation at the Earth's equatorial region, which ultimately resulted in altered global precipitation patterns (Webster, 1985). The amplitude of the climatic changes, resulting in large fluctuations in lake level within the equatorial Newark Basin, was most likely due to the immense size of the Pangean land-mass (e.g. Crowley et al., 1992).

Fluctuations in lake levels are expressed in the Newark Basin strata as changes in facies through time. These facies fluctuations, referred to as cyclostratigraphy, have been correlated in the Newark Basin to celestial mechanical periodicities (e.g. Van Houten, 1964; Olsen, 1986). Van Houten (1962) was the first to suggest that meter-scale fluctuations in the sedimentary facies within the Newark Basin are related to changes in lake depth caused by climatic variations. Van Houten (1962) also attributed the fluctuations (now called Van Houten cycles) to the 21 ky cycle of climatic precession (**Figure 5**). More recently, extensive studies on outcrops, and cores from the Newark Basin Coring Project, have shown the existence of the larger-period composite Van Houten cycles (beat cycles of eccentricity) of climatic precession (Olsen, 1986; Olsen, submitted).

The proxy used to indicate lake depth and thus climatic cycles are depth ranks (Olsen, 1986). Depth ranks are a classification of sedimentary structures and bedding characteristics arranged in order of increasing water depth from playa-like conditions (rank 0) to deepest lake deposits (rank 6; **Table 2**). Depth is converted to age in Olsen's (1986) outcrop study assuming a constant sedimentation rate of 0.7831 ft/ky (22.2 cm/ky). Results from spectral analyses performed on the depth ranks of sections of outcrop within the Newark Basin show evidence of orbital forcing effects (Olsen, 1986; **Figure 6**). Similar analyses performed on drill cores from the Newark Basin Coring Project show even stronger correlation between lake depth and orbital forcing functions (Olsen, submitted; Reynolds, 1994; **Figure 7**). The results of the outcrop study (Olsen, 1986) prompted the Newark Basin Coring Project, which provided the opportunity for the seismic and geophysical log examinations which are the basis of this study.

Orbital Forcing Functions

The Milankovitch modulation frequencies (orbital forcing functions) that effect climate are predicted on the basis of celestial mechanics. Inherent in the rotation of the Earth is a precessional constant. The interaction of the fundamental eccentricity frequencies of Venus, Mars, Jupiter, and the Earth with the precessional constant generate four periods of climatic precession (which average to form the 21,000 year period of the Van Houten cycles). Interaction of these four non-synchronous periods of climatic precession generates higher order beat cycles of climatic precession at 96,000, 127,000, 404,000, and 2,000,000 years. The major astronomical periods comprised of the periods and beat cycles of climatic precession affect the intensity of incoming solar radiation which in turn affects the climate. It is predicted that today's precessional constant of 23,694 years was 5-15 % smaller during the Triassic (Lasker, 1990; Berger et al., 1992) because of lunar recession. Thus an uncertainty exists in the exact values of todays orbital periodicities extrapolated to the Triassic. Variations in the obliquity of the earth's axis to the sun (with a predicted periodicity of 41,000 years) have a strong effect upon seasonal variations at the mid-latitudes, but minimal effects at the equator. Kent and Olsen (1992) suggest that the effect of the obliquity cycle is minimal in the Newark Basin because of its equatorial position in the Triassic.

Newark Basin Coring Project

The Newark Basin Coring Project was initiated in 1991 to acquire a continuous record of the Triassic cyclostratigraphy in the Newark Basin in order to study the effects of orbital forcing functions (Olsen and Kent, 1990; **Figure 8**). By locating drilling sites progressively closer to the border fault system, a series of six 1 km deep cores sampled 5.4 km (over 20,000 ft) of section. There is a 15 % overlap in coverage between adjacent cores for correlation (Olsen and Kent, 1990; **Figure 9**).

Shallow reflection profiles were collected at Newark Basin Coring Project sites in order to tie reflections to specific lithologies in the geophysical logs. The three sites chosen for analysis in this study are Titusville, Nursery Road, and Princeton. Titusville and Nursery Road were chosen because the lower portion of the Passaic Formation and the Lockatong Formation, which crop out and are located in the subsurface at these sites, contain the most prominent cyclostratigraphy within the Newark Basin. Princeton was chosen because we hoped to image the Stockton Formation onlapping Paleozoic basement. Physical properties, including sonic velocity and density, were logged at each of these core sites as part of the Newark Basin Coring Project and are used in this study.

High-Resolution Reflection Profiles

In an attempt to examine the lateral continuity of strata in the vicinity of the Newark Basin Coring Project sites, a series of high-resolution reflection

profiles were collected. Synthetic seismograms constructed from the geophysical log data were to be used to tie specific lithologies to the seismic data. This study examines five of the reflection profiles, two profiles at the Titusville site and three profiles at the Princeton site, collected in the summer of 1991. The reflection profiles are referred to as Washington Crossing Lines (WCL) 1 & 2, and Princeton Lines (PRL) 2, 3 & 4.

The data were collected using a BISON 24-channel DIFP 9024 seismograph and 30 Hz geophones. The source was a BISON Elastic Wave Generator (EWG), which uses a large elastic band to accelerate a 750 lb weight onto a metal plate. The EWG source is capable of accurate repeatable strikes, and for the reflection profiles collected in the Newark Basin 10 strikes were recorded and summed to enhance signal at each source location. The record length (time) is 1 second, and the sampling rate is 0.5 ms. Data were recorded in the field in a trace sequential format and transferred from the BISON onto micro floppy disks for storage.

The shot-receiver geometry for each shot of the five seismic lines is an off-end spread with a near offset of 360 ft, a far offset of 1050 ft, and a group interval (with one geophone per group) of 30 ft (**Figure 10**). Using a roll box to switch the geophones to the appropriate channels for the seismograph, a continuous sequence of shots was recorded along each of the seismic line transects, with a shot spacing of 30 ft. The result for each seismic line is a 12-fold common midpoint (CMP) profile with a midpoint spacing of 15 ft (**Figure 11**).

Data processing is done using GALAXY seismic data processing software by Halliburton Geophysical on an Apollo/Hewlett Packard workstation. The conventional processing scheme detailed in **Figure 12**, is modified for

processing the Washington Crossing and Princeton profiles, to compensate for problems specific to each set of profiles.

Washington Crossing Lines 1 & 2

The Washington Crossing lines are located in Washington Crossing State Park at the Titusville site. Washington Crossing Line 1 (WCL1) is 2220 ft in length, runs parallel to the regional strike of the strata in the Newark Basin (about N45E), and intersects the Titusville core site between shotpoints 54 and 55 (**Figure 13**). The near-trace display shows shallow refractions between 0.05 to 0.28 sec and the high-amplitude air wave at 0.31 to 0.33 sec (**Figure 14**). Discontinuities in the near-surface refractions occur because of a complicated near surface layer. There is a noticeable lack of coherent reflections.

The processing scheme for WCL1 is detailed in **Figure 15.** The raw field records are adjusted for topography (from transect survey information) by correcting with a velocity of 1850 ft/sec determined by inverting the slope of the direct arrival. Electronic noise recorded prior to the first arriving refraction is muted. Bad or noisy traces, identified on the field records, are edited (scaled to zero).

To correct for the amplitude attenuation observed in the raw records, the data are scaled. If amplitude analysis of any kind is to be attempted on the data, a scaling method must be chosen to preserve the relative amplitudes. However, this study is only concerned with generating a stacked section, so a simpler method, called automatic gain control (AGC), is used. Automatic gain control is a method of scaling the amplitudes of the data through the use of a

"sliding" analysis window. At each position of this window, the average amplitude within the window is calculated, and a gain factor is applied to the data, relating the amplitude within the window to an average amplitude over the entire trace. Thus, the entire trace is scaled to a similar amplitude. Unless otherwise specified, the AGC window length used on the data is 0.13 seconds.

Amplitude spectra across WCL1 are similar, and typically contain signal between 5 and 240 Hz (**Figure 16**). Above 240 Hz, amplitude drops off. The amplitude spectrum is used to design a band-pass filter. The four specified points of the filter define a "scaling trapezoid", in which the frequencies below the first point and higher than the fourth point are scaled to zero. Frequencies between the second and third points are scaled 100 % (i.e. unchanged from the original amplitude). The ramp zone between the first and second point is scaled from 0 to 100 %, and the ramp zone between the third and fourth points is scaled from 100 to 0 % of original amplitude. For WCL1, the band-pass filter points are 5, 10, 200 and 320 Hz.

The prominent air wave is visible in all of the WCL1 field records. The best method to eliminate coherent dipping noise (e.g. an air wave) is by filtering in the frequency-wavenumber (f-k) domain. A sloping mono-frequency signal in the time-offset (t-x) domain plots as a single point in the f-k domain by simple Fourier conversion. Energy with a constant velocity in t-x space plots as a straight line in f-k space. The multi-frequency air wave plots as a line in f-k space (with a slope related to velocity of sound in air in t-x space), and can be filtered without disturbing signal in t-x space with differing slopes. An attempt is made to attenuate the air wave in WCL1 by filtering a swath in f-k space with a slope of 1200 Hz/wavenumber, and a vertical (frequency) width of +/- 10 Hz. **Figure 17** shows the results of the f-k filter, and attenuation of the air wave.

However, there are still no observable reflections. **Figure 18** shows the expected geometry of reflection hyperbola at several moved-out velocities.

Deconvolution is a process which compresses the source wavelet , and attenuates short period multiples. The purpose of compressing the source wavelet is to increase temporal resolution by shortening the wavelength (increasing the frequency). Deconvolution is achieved by applying an inverse filter to the data. The inverse filter is calculated from a filter length and a lag time. The filter length is equivalent to the wavelength of the source wavelet. The lag time equals the length in time desired for the output (compressed) wavelet. The filter length is initially selected at the second zero crossing of an autocorrelation curve (**Figure 19**), which approximates the length in time of the source wavelet. The lag length is adjusted to generate the 'cleanest compression' of the signal without introducing excessive high-frequency noise. The best improvement in the WCL1 data is observed using a deconvolution lag of 0.006 seconds, an operator window of 0.04 seconds, and a variable analysis window. The analysis window is variable across the length of the profile, and was picked a large as possible below the first arrival and above the air wave (**Figure 20**).

After sorting to common midpoint (CMP) geometry, the gathers are examined by several methods of velocity analysis to correct for normal moveout (NMO) and thus flatten reflection hyperbola for stacking. Two methods for obtaining stacking velocities for WCL1 are used. In both methods, a constant velocity correction for normal hyperbolic moveout with offset is applied to the analyzed gathers, and a mute is applied to avoid stacking in refractions as signal (**Figure 21**) . The fist method, a velocity scan, calculates the semblance (amplitudes) across a single record stacked at several velocities. **Figure 22** is

an example velocity scan in which the traces in CMP gather 77 were corrected for NMO and summed at velocities from 4000 to 16000 ft/s with a 100 ft/s increment. The resulting "smeared" look suggests that no reflection hyperbola stack to form a coherent signal at any of these velocities. The second method is a velocity analysis using constant velocity stacks. Constant velocity stacks are generated by performing normal moveout at a constant velocity for the entire length of a gather, for several CMP gathers, and displaying the stacked traces. Normally, constant velocity stacks are generated for a group of traces at spaces intervals along the line. Because of the small dataset size of the WCL1 (and the other four profiles), the entire set of CMP gathers are used to generate a series of constant velocity stacks. **Figure 23** is an example of a constant velocity stack of WCL1 at a velocity of 14000 ft/s. Plots of this type are generated for a range of velocities from 4400 to 22400 ft/s at a spacing of 200 ft/s. The resultant constant velocity stacks show the lack of any coherent reflectors.

Washington Crossing Line 2 (WCL2) is a dip line 3300 ft in length, beginning at roughly station 36 of WCL1 (**Figure 13**). Similar problems as those seen in WCL1 are observed in the near trace display of WCL2 (**Figure 24**); namely a prominent air wave and high amplitude refractions.

WCL2 is processed using the same scheme detailed for Line 1. The results are shown in **Figures 25** through **31**. The result of velocity analysis using the same two methods detained above for WCL2 yields no evidence of coherent reflections.

Princeton Lines 2, 3 & 4

The Princeton seismic lines are located near Princeton, N.J., at the Princeton core site. Princeton Line 2 (PRL2) is 2970 ft in length and runs from NE to SW (**Figure 32**). Inspection of the near-trace display of PRL2 (**Figure 33**) shows immediate contrasts to the Washington Crossing Lines. The first arriving refraction is much more defined, as seen by the clean break at the beginning of the traces, and the air wave is not as predominant. The processing scheme for PRL2 (and the other Princeton lines; **Figure 34**) differs from the scheme used in the Washington's Crossing lines in that an f-k filter is not used (it is found to be to destructive to the data, in this case). Additionally, near-surface refracted arrivals, which are more clearly observed in the Princeton seismic lines, are used to correct for residual static time shifts, due to the complex near-surface, through a refraction statics correction technique.

The processing steps and parameters for PRL2 are detailed in **Figures 34** through **40**. Velocity analyses are performed on PRL2 by the two methods described under Washington Crossing processing, and similar results are seen. **Figure 41** is a typical example of a velocity scan of a PRL2 common midpoint gather. No coherent reflections are observed by either method.

Princeton Line 3 runs 2610 ft from SW to NE, intersecting PRL4 at station 1, and the Princeton borehole site at station 43 (**Figure 32**). The near trace display of PRL3 shows the similarities with PRL2 (**Figure 42**). A similar processing scheme is used, and the results are shown in **Figures 43** through **48**.

Princeton Line 4 runs parallel to PRL2 (NE to SW) and is 3170 ft in length (**Figure 32**). The near trace display of PRL4 shows the similarities with the two

previous Princeton seismic lines (**Figure 49**). A similar processing scheme is used, shown in **Figures 50** through **55**.

Near-Surface Problems

The results of processing the Washington Crossing and Princeton lines demonstrate a distinct near-surface problem at both locations. The complex near-surface is revealed by the both the varying arrival times of the first breaks, which suggests changing layer thicknesses, and the varying slopes of the first breaks, which suggests lateral velocity variations. A complex near-surface layer causes trace-to-trace static time shifts which have a detrimental effects upon reflection hyperbola generated from deeper interfaces (**Figure 56**). However, given good velocity estimates and control on the geometry of the near surface layers from a near-surface model, times shifts calculated by applying a refraction statics correction technique can be applied to correct for variations in the thickness and velocity of near-surface layers. By accounting for these time shifts, the refraction statics correction technique is used to computationally correct the source and receivers of the seismic experiment to a datum *below* the near-surface layer.

The first step toward resolving the near-surface problem is the generation of a near-surface model. **Figure 57** shows the best interpretation of the six layers in the near-surface of Princeton Line 2. Several different sets of information used to construct this cross-section. First, time-distance pairs are selected from approximately every sixth record of PRL2 (**Figure 58**) for layers 1 and 2 (see **Figure 57** for layer identification). These time-distance pairs are

used to generate velocities, intercept times, and layer thicknesses (**Table 3**). The 1D solutions of layer 2 (interface between Layer 1 & 2 and between 2 & 3) are plotted with distance (**Figure 59**), to generate an approximate 2D model of the layer boundaries (assuming constant layer velocities). The layer velocities are the average velocity of each layer.

Next, time-distance pairs of refractions from the six layers from every tenth record are inverted to get apparent velocities (**Table 4**). These apparent velocities are then plotted versus distance across PRL2, to show variations in velocity along each interface (**Figure 60**).

A plot of the velocity of first arrivals calculated by regression on digitized first break time-offset picks shows two trends in velocity (**Figure 61**) at 12,000 ft/s and 20,000 ft/s. The two deviations from 'good' straight line refractions by the first arrival seen in the field records - the short wavelength perturbation seen in the field records from station 4 through 16, and the break in slope from 12 kft/s to 20 kft/s - are seen in the plot of the correlation coefficient of the regression lines from the digitized picks (**Figure 62**). The 'fit' is not as good in the vicinity of the short wavelength perturbation and the change in slope due to a lateral velocity change. Thus, the first-breaks are modeled as the refracted arrivals associated with the lateral velocity change from two isovelocity layers, 5 & 6.

2-Dimensional raytracing via the MacRay program (Luetgert, 1992) constrains a depth model of layers 5 & 6. By this iterative method of raytracing, a model of the first arrival in PRL2 is obtained. An interface is generated, with the velocity gradient corresponding to the 12,000 to 20,000 ft/s lateral shift in velocity seen in the field records. A constant velocity of 4800 ft/s, calculated from apparent velocities of layers 1 through 4, is used for the upper layer.

Travel times are calculated through the model and compared with the observed travel times in the field records (e.g **Figure 63**). If a poor match is observed, the model is adjusted and the travel times are recalculated for another comparison. The final 2D raytracing model shows a solution of the depth and geometry of the layer 5/6 (first break) boundary (**Figure 64**).

The near-surface model of PRL2 (**Figure 57**) is a compilation of velocities and interface geometries, described above, with the assumption that all layers are isovelocity layers, i.e. there are no lateral velocity gradients within layers. First, the upper surface is shown from the surveyed elevation data, plotted versus the corrected datum. Next, layers 1 and 2 are modeled in 2D by extending the 1D model results laterally, with the lower interface of layer 2 terminating at the interface of layer 5 because refractions from layer 2 are not seen in that section of PRL2. Third, the depth to the interface from the upper layers to layers 5 & 6 (first arrival) is modeled as per the 2D raytracing model. The shapes of the remaining interfaces are constrained by examining plots of apparent velocities and assuming an increasing trend in apparent velocity suggests an upward sloping isovelocity interface and a decreasing trend suggests a downward slope of the same isovelocity layer. Finally, depths to these remaining interfaces are constrained by the location of the interfaces of the bounding layers.

The next step in correcting for the near-surface is to use the near-surface model and digitized first-break time picks in a refraction statics correction. Subweathering velocities at each station of PRL2 are estimated by fitting a regression line through each set of time-offset pairs corresponding to the first arrival (**Table 5**). The inverse of the slope of this regression line is the velocity

of the layer in which the energy is refracted. Weathering velocities are generated by calculating an average velocity to the first-break interface from the near-surface model at every tenth station and linearly extrapolating to stations in between. Calculations from the near-surface model are made every tenth station because the near-surface model is only a coarse-scale representation and not expected to be accurate at the scale of station (trace) spacing.

A diminishing residual matrix algorithm is utilized as the method of refraction statics correction on Princeton Line 2. In the case of PRL2, the first arriving refraction is used as a datum, and the set of digitized time-offset pairs for each trace expressing the first break are used to calculate time shifts. The diminishing residual matrix algorithm decomposes a matrix, generated with rows corresponding to receiver station positions and columns corresponding to shot station positions, into shot and receiver delay time profiles. The technique gives a solution which minimizes, in the least-squares sense, the differences between overlapping portions of shot and receiver delay time profiles.

The final corrections for the near-surface layer of PRL2 (the total static shifts applied to each trace) are calculated from delay times associated with each shot and receiver station (from the diminishing residual matrix technique) and the weathering and subweathering velocities (calculated by regression on the digitized time picks and from the near-surface model). This method of refraction statics does a good job of correcting for the weathering layer (i.e. everything above the first arriving interface; **Figure 65**) by datuming the source and receivers in each gather to the layer 5/6 interface. The long-wavelength variations are noticeably corrected on a near-trace display of the corrected dataset (**Figure 66**).

Even with the additional static corrections, coherent reflection hyperbola still are not recognizable with PRL2. Velocity analysis performed on the corrected data yielded no new results. An example of a constant velocity stack, this time for common midpoint records 72 through 80 stacked at constant velocities from 4400 to 22400 ft/s, demonstrate the lack of coherent reflections (**Figure 67**). Princeton Line 2 is better or equal in quality compared to the other seismic lines examined in this study, and it is concluded that no reflection data can be obtained from any of the seismic profiles, and continued processing on the Washington's Crossing and Princeton lines would be futile.

Geophysical Logs and Synthetic Seismograms

The Titusville, Nursery Road, and Princeton core holes were geophysically logged as part of the Newark Basin Coring Project. The measurements included sonic velocity and density, and were recorded at 2 ft (0.61 m) intervals. The upper 300 to 400 ft (90 to 120 m) of the cores penetrate a weathered zone with noisy logging results (Reynolds, 1994). This is consistent with the seismic data. The upper 400 ft of log data were removed by Lamont workers.

The product of sonic velocity and density is impedance. Thus, the sonic velocity and density logs from the core holes are used to generate an impedance array (or reflectivity series) for each core hole (**Figs. 68, 69 & 70**). The reflectivity series, when converted to time by summing all of the pieces of two-way traveltime for each interval represents, an ideal seismic response

(synthetic seismogram) to the lithologies represented by the sonic velocities and densities.

Synthetic seismograms are filtered, to create synthetic seismograms to match different typical seismic sources. For plotting purposes, the synthetics had to be scaled using a constant gain factor, which varies depending on the filter, but is consistent from core to core figures so that comparisons can be made. There are six synthetic seismograms for each core (**Figs. 71, 72 & 73**). The first synthetic in each figure represents the unfiltered synthetic seismogram, which has a frequency content up to the Nyquist frequency of the synthetics (at 0.5 ms) of 1000 Hz. The next three synthetics in each figure are filtered and contain frequencies of typical sources: a low frequency source with a 5 to 120 Hz frequency content (e.g. Vibroseis), medium frequency source with 10 to 240 Hz frequency content (e.g. Elastic Wave Generator), and high frequency source with a 50 to 420 Hz frequency content (e.g. Betsy Seisgun). The fourth and fifth synthetics in **Figures 71, 72 & 73** are generated to match the Washington Crossing and Princeton reflection profiles. Although the source for the experiment is an Elastic Wave Generator (with idealized frequency components of 10 to 240 Hz), these two additional synthetics are filtered from 10 Hz to 180 Hz to better represent the response of the EWG source to the rocks at the sites specific to the experiment (as seen in the amplitude spectra). The fourth synthetic in each figure represents an idealized case (no noise). The fifth represents the synthetics in the 5 to 180 Hz spectrum with added random noise generating a S/N ratio of 2. The presence of observable reflections in this fifth synthetic, for each of the three sites, suggests that the lack of reflections in the seismic profiles is not due to the lack of reflectivity.

Cyclostratigraphy and Sedimentation Rates from Reflectivity Series

To determine whether an orbital forcing function can be extracted from the reflectivity series, a relationship must be established between the seismic reflectivity and orbital periodicities. It has been established that a relationship exists between orbital periodicities and the cyclicity of lake depth within the Newark Basin (e.g. Van Houten, 1964; Olsen, 1986). One of the main assumptions of conclusions drawn from the sediment record is that climatic forcing effects can be seperated from tectonic effects. As previously mentioned, there are many intra-basinal faults throughout the Newark Basin thought to have been syn-depositional. Syn-depositional faulting of previously deposited Triassic sediments within the basin and also of the Paleozoic bacement forming the basin itself, would have had substantial influence upon the sediment record by altering sediment sources and changing the geometry of the basin (e.g. making a deep lake more shallow). Both of these effects of syn-depositional tectonics would effect the rate of sedimentation and facies deposited within the basin. The assumption that climatic forcing effects can be seperated from tectonic effects is validated if the tectonic effects are random. Because spectral analyses respond to fixed periodic events, orbitally forced effects upon sedimentary facies would show up in a spectral analyses, whereas random tectonic effects upon sedimentation rates and facies would not. Thus, for the purpose of correlating orbital forcing functions to reflectivity series, if we assume tectonic effects are non-periodic and the relationship between orbital forcing

and lake depth established in the literature is valid, a relationship must be set between lake depth and the reflectivity series.

Relating Lake Depth to Seismic Reflectivity

By examination of the cores from the Newark Basin Coring Project, Olsen (personal comm.) generated digitized sections representing lake depth by rank (Olsen, 1986) for the Titusville (**Figure 74**), Nursery Road (**Figure 75**), and Princeton (**Figure 76**) cores. By comparing the reflectivity series (which is the product of rock velocity and density, and is a function of grain size, matrix lithology, cementation and compaction) to the ranked lake depth sections, the relationship between reflectivity and lake level is qualitatively observed (**Figs. 77, 78 & 79**).

Reynolds (1994) suggests that in the Passaic Formation, carbonate and silicate cements are present in the deeper-water facies and thus produce an increase in velocity relative to the arid facies, thus deeper facies have lower sonic velocity and higher reflectivity values. During deposition of the Lockatong Formation, mean lake depth was greater than during the Passaic Formation deposition, and the shallow-water facies of the Lockatong Formation contains carbonate and dolomite cements producing a higher velocity (Reynolds, 1994). Reynolds (1994) also noted that the deepest-water facies in all cases are characterized by thick, black shales with a high total organic content, which have a significantly lower velocity than the cemented material which encases them. Thus the deepest-water layers in all instances are characterized by low velocity and high reflectivity contrasts. This is observed directly in **Figures 80, 81 & 82** by correlating the synthetic seismograms generated in this study with

the litho-stratigraphy from Olsen (personal comm.) using the depth scale of the geophysical logs. Although thickness of the units, lithology, and cements are all changing through time, the cyclical pattern of fluctuating lake depth caused by orbital forcing functions remains constant, and is preserved in the sediment record as cyclostratigraphy. Thus, the reflectivity series, which responds to the facies changes from shallow to deep lake depth, is a good indicator orbital forcing functions, and spectral analyses examining the periodicities of the fluctuations are meaningful.

Analysis of the Reflectivity Series

A composite reflectivity series is generated by correlating tie points of the Titusville, Nursery Road, and Princeton cores. Detailed stratigraphic, palynofloral, and paleomagnetic study of the overlapping sections of the cores (Olsen, submitted) has yielded the tie points for the reflectivity series. The Titusville (at 2745.0 ft) and Nursery Road (at 432.6) records match at the Tumble Falls Member of the Lockatong Formation. The Nursery Road (at 2664.0 ft) and the Princeton (at 448.6 ft) records match at the Scudders Falls Member of the Lockatong Formation.

Spectral analysis is performed on a composite core reflectivity series without converting to age (**Figure 83**). Converting depth to age using a constant sedimentation rate of 0.7283 ft/ky (from Olsen, 1986) yields close ties to orbital parameters:

Peak (ft)	Period (ky)	Cycle (ky)
344.8	*473.4*	413
128.2	176.0	
78.7	*108.0*	100
64.1	88.0	
29.2	*40.1*	41
26.2	*36.0*	41
20.5	28.1	
16.0	*22.0*	21
14.2	*19.5*	21

Estimates of Sedimentation Rates

The accuracy of sedimentation rate average used to generate the age model for the spectral analysis can be examined by manipulating the data contained in the reflectivity series of the Titusville, Nursery Road, and Princeton sites. In order to eliminate noise from smaller cycles and variations in general, smoothed reflectivity series are generated by running an averaging window down the length of the cores. The length of the smoothing window is found to effect the reflectivity series by removing the short wavelength modulations (as per a frequency filter), and does not affect the presence or absence of peaks or troughs. There are three averaging window lengths used to filter out sequentially longer frequency variations. The 30 ft smoothing window (run by averaging 15 impedance values from the 2 ft intervals every 2 ft) shows the 130ky cycle, which repeats every 95 ft with a sedimentation rate of 0.7283 ft/ky. The 100 ft smoothing window shows the very prominent 400 ky cycle, which has a thickness of 300 ft with a 0.7283 ft/ky sedimentation rate. And the 300 ft smoothing window, which shows the 2 My cycle in the Nursery Road and Princeton but is questionable in the Titusville, with a thickness of 1450 ft with a sedimentation rate of 0.7283 ft/yr. As previously mentioned, the deepest-water

facies in all instances within the Newark Basin show high reflectivity, specifically the 2 My and 400 ky cycles (Reynolds, 1994), but the 130 ky cycles are also seen with the smoothed curves (**Figs. 84, 85 & 86**). The compound borehole reflectivity series also clearly exhibits the 413 ky cycles (100 ft smoothing window), and the 2 My cycles (300 ft smoothing window; **Figure 87**).

Using the 413 ky cycles in the compound corehole reflectivity series, estimates of the sedimentation rates in the Newark Basin throughout the Triassic can now be made. For each of the cores, the time-depth pairs associated with the 413 ky peak are noted, and sedimentation rates are then calculated between 413 ky cycles (**Table 6**). This is done for the Titusville (**Figure 88**), Nursery Road (**Figure 89**) and Princeton (**Figure 90**) reflectivity series, showing the variations in sedimentation rates throughout the depositional history. Additionally, a linear regression is calculated for the 413 ky time-depth pairs for each core (**Table 6**). The highest sedimentation rate of 0.8254 ft ky (25.16 cm/yr) is in the Princeton core, which correlates with the fluvial-deltaic Stockton Formation. The smallest sedimentation rate of 0.6822 ft/ky (20.76 cm/yr) is in the Nursery Road core, which contains all of the deep-water lacustrine Lockatong Formation. The Titusville core has an intermediate sedimentation rate of 0.7703 ft/ky (23.48 cm/ky), correlating with the Passaic Formation. A linear regression of the compound sequence (**Figure 91**), representing the average rate of sedimentation throughout the 10 My history recorded by the Titusville, Nursery Road, and Princeton reflectivity series, yields a rate of 0.7316 cm/ky. This rate, generated by fixing the 413 ky cycle peaks in the reflectivity series, is only 0.45 % larger than the rate of 0.7283 ft/ky (22.2 cm/ky; Olsen, 1986) used to convert the spectral analysis peaks of this study from depth to age.

Summary

The poor results of the Washington Crossing and Princeton seismic profiles are a result of a complex near surface layer. At the Princeton site, this complex near-surface consists of six different layers, with undulating interfaces, extending to 60 ft. Similar near-surface conditions are expected to exist at the Washington Crossing site. Detailed processing was attempted, but without coherent reflections, no reasonable stack sections can be produced.

Synthetic seismograms show significant reflectivity at the sites of the Washington Crossing and Princeton lines. Even the lower section of the Titusville core, with the lowest impedance contrasts of the three cores examined in this study, yields good reflections with a S/N ratio of 2. Thus good shallow reflection profiles should be attainable if a way to overcome the near surface problem is found.

Cyclostratigraphy within the Newark basin's Triassic section can analyzed by examining reflectivity series generated from sonic velocity and density logs. Facies variations due to cyclical fluctuations in lake depth generate corresponding cyclical fluctuations in the reflectivity series. Titusville, Nursery Road and Princeton sites of the Newark Basin Coring Project are examined in this study. Spectral analysis on the composite reflectivity series generated from these three sites demonstrates the existence of prominent periodicities. The cycles observed in the spectral analyses have 21,000, 41,000, 100,000, and 413,000 year durations when assuming a constant sedimentation rate of 0.7283 ft/ky throughout the 10 My history of deposition

recorded in the three sites.

The constant sedimentation estimate of 0.7283 ft/ky (from Olsen, 1984) used in the spectral analyses of this study is corroborated by fixing the 413 ky cycle peaks in the reflectivity series and calculating a regression line through the resultant sedimentation rate values. However, variations in sedimentation rates seen by fixing 413 ky cycle peaks are significant, and explain the 'smearing' of the cycle variations in spectral analyses.

Origin of the Major Astronomical Periods

fundemental frequencies of the solar system	cycles / yr	period	average periods	average periods
g2, Venus	5.7530246E-06	173,822		
g3, Earth	1.3398682E-05	74,634		
g4, Mars	1.3823690E-05	72,340		
g5, Jupiter	3.2784068E-06	305,026		
precessional constant				
k	3.8919592E-05	25,694		
periods of climatic precession				
k+g5 = p1	4.2197999E-05	23,698	19,037	
k+g2 = p2	4.4672617E-05	22,385		21,039
k+g3 = p3	5.2318274E-05	19,114	23,041	
k+g4 = p4	5.2743282E-05	18,960		
beat cycles of climatic precession				
p3-p4	4.2500818E-07	2,352,896		
p2-p1	2.4746178E-06	404,103		
p2-p3	7.6456570E-06	130,793		
p2-p4	8.0706652E-06	123,906	127,349	
p1-p3	1.0120275E-05	98,812		112,085
p1-p4	1.0545283E-05	94,829	96,820	

TABLE 1: Origin of the Major Astronomical Periods (Lasker, 1990). The fundimental frequencies of the solar system, g2, g3, g4, and g5, combine with the Earth's precessional constant to form the periods of climatic precession. This combination of the periods generates the higher-order cycles of climatic precession; the 100,000, 130,000, 400,000, and 2,000,000 year cycles. The two columns of averaged periods shows the periods commonly observed in lower-resolution analyses.

Depth Rank	Sediment fabric
rank 0	massive bedded calcareous claystone and siltstone with root, tube , crumb, and vesicular fabric. Faint parent fabric exsists. Intensely desiccated, deposited during the time of lowest lake level.
rank 1	Intensely brecciated and cracked calcareous claystone and siltstone. Burrows can be common but obvious parent fabric is present. This fabric shows less intense desiccation and on a time-averaged basis was deposited under relatively deeper water than the facies of depth rank 0.
rank 2	Thin bedded calcareous claystone and siltstone with desiccation cracks. Large patches of uncracked matrix are preserved and reptile footprints and burrows are often present. Relative low density of desiccation cracks.
rank 3	Thin bedded calcareous claystone and rare siltstone with very small scale burrows; desiccation cracks are rareto absent and pinch and swell lamination is often present. Deposited under relatively shallow water, as evidenced by frequent erosion and deposition above wave base.
rank 4	Evenly laminated calcareous claystone with some small-scale burrows and abundant discontinuous microlamination. There are no desiccation cracks.
rank 5	Evenly and finely laminated calcareous claystone or limestone with abundant discontinuous microlaminations. There are no desiccation cracks. Deposited in water frequently anoxic with only infrequent veltilation and hence deeeper than that of depth rank 4.
rank 6	Microlaminated calcareous siltstone with only rare disruptions and no desiccation cracks. Deposited in least oxygenated water when the lake was deepest and when the bottom wa most insulated from wind- and wave- generated turbulence.

from Olsen, 1986

TABLE 2: Depth rank as clssified by Olsen (1986) expressing specific sediment fabrics as related to relative lake level (depth). Ranks are from 0 to 6, with 6 representing the deepest time-averaged lake level.

TABLE 3: Thicknesses of layers 1 and 2 calculated from apparent velocity picks and intercept time for approximately every sixth record of Princeton Line 2. Calculations are made using 1D traveltime formula.

		prl2	thickness	
Layer (rec 1)	Apparent Velocity	Ti	Layer Thickness	Interface Depth
1	1835	0	26.95523237	
2	3941	0.026	8.182572883	35.13780525
5	12483	0.033		
Layer (rec 6)	Apparent Velocity	Ti	Layer Thickness	Interface Depth
1	1795	0	22.36664814	
2	3821	0.022	10.67871201	33.04536015
5	12683	0.03		
Layer (rec 11)	Apparent Velocity	Ti	Layer Thickness	Interface Depth
1	1831	0	25.33093135	
2	4273	0.025	6.021328592	31.35225994
5	12257	0.03		
Layer(rec 20)	Apparent Velocity	Ti	Layer Thickness	Interface Depth
1	1832	0	20.70901036	
2	3929	0.02	9.180833513	29.88984387
3	5927	0.025		
Layer(rec 29)	Apparent Velocity	Ti	Layer Thickness	Interface Depth
1	1837	0	12.29326106	
2	4148	0.012	14.91515091	27.20841197
3	6063	0.018		
Layer(rec 39)	Apparent Velocity	Ti	Layer Thickness	Interface Depth
1	1826	0	10.24889893	
2	4019	0.01	12.06383988	22.3127388
3	5819	0.015		
Layer(rec 46)	Apparent Velocity	Ti	Layer Thickness	Interface Depth
1	1783	0	10.15131356	
2	3728	0.01	17.04981298	27.20112654
3	5958	0.018		
Layer(rec 52)	Apparent Velocity	Ti	Layer Thickness	Interface Depth
1	1839	0	10.41636806	
2	3914	0.01	18.21033463	28.62670269
3	6163	0.018		

Layer(rec 58)	Apparent Velocity	Ti pri2 thickness	Layer Thickness	Interface Depth
1	1792	0	9.898163817	
2	4217	0.01	16.69436172	26.59252553
3	5847	0.016		
Layer(rec 64)	Apparent Velocity	Ti	Layer Thickness	Interface Depth
1	1839	0	15.49945635	
2	4031	0.015	7.972826609	23.47228295
3	6037	0.019		
Layer(rec 70)	Apparent Velocity	Ti	Layer Thickness	Interface Depth
1	1809	0	16.29280412	
2	3938	0.016	4.880510687	21.17331481
3	5916	0.019		
Layer(rec 82)	Apparent Velocity	Ti	Layer Thickness	Interface Depth
1	1836	0	15.57623867	
2	3928	0.015	9.944614643	25.52085332
3	6025	0.02		
Layer(rec 86)	Apparent Velocity	Ti	Layer Thickness	Interface Depth
1	1836	0	16.74418994	
2	3824	0.016	11.88959214	28.63378208
3	5824	0.022		

Layer 1		layer 2		layer 3		layer 4		layer 5		layer 6	
Sta.	Vel.	Sta.	Vel.	Sta.	Vel.	Sta.	Vel.	Sta.	Vel.	Sta.	Vel.
1	?	1	4928	1		1		1	11500	1	
10	?		?	10		10		10	11228	10	
20	1979	20	3343	20	?	20		20	12879	20	
30	2179	30	3680	30	6536	30		30	12897	30	
40	2115		?	40	5474	40	7550	40	12164	40	
50	1710		?	50	5474	50	?	50	10960	50	19039
60	1610		?	60	6737	60	?	60		60	20852
70	1745		?	70	5687	70	7422	70		70	20399
80	1889	80	4342	80	?	80	7840	80		80	?

TABLE 4: Velocities with distance calculated for each of the six layers modeled for Princeton Line 2. Velocity picks were only made with high confidence. Question marks (?) are used where the layer generated a suspect refractor which could not be accurately quantified. Layer 1 velocities vary by 15%. Layer 2 velocities vary by 20%. Layer 3 velocities vary by 12.5 %. Layer 4 velocities vary by 3.5%. Layer 5 velocities vary by 8.5%. Layer 6 velocities vary by 5.5%.

TABLE 5: Calculated velocities and r^2 correlation coefficient by linear regression on digitized first break time picks for each station of Princeton Line 2. Additionally, 1D calculations of the interface depth with an upper layer velocity of 4800 ft/s at each station is included. Regression equations from Snedecor and Cochran (1989).

				v1=4800
sta.	velocity	to	r^2	thick (1D)
1	11063.0111	0.0255658	0.98942315	68.1019462
2	11134.4199	0.02089116	0.98518737	55.5673681
3	11194.0299	0.02335333	0.98361702	62.0412158
4	10961.0802	0.02138986	0.97704563	57.1019604
5	11150.6141	0.02444145	0.9754928	64.9890841
6	12182.2034	0.0301287	0.95745577	78.6733052
7	12518.1422	0.03351507	0.96571019	87.0931997
8	12948.0203	0.03800986	0.94715712	98.2222363
9	13431.9642	0.04030493	0.96253843	103.570809
10	13745.0199	0.0424587	0.9573347	108.747418
11	13961.9587	0.04392232	0.97710523	112.256009
12	14631.0433	0.04839812	0.97955601	122.960927
13	14778.3251	0.04850333	0.97833934	123.081123
14	15218.3502	0.04842435	0.97013936	122.469792
15	13942.2105	0.04539246	0.98840165	116.035431
16	14877.1022	0.05177841	0.97355598	131.28946
17	13452.9148	0.04655333	0.9902816	119.599975
18	13424.1245	0.04798261	0.98921655	123.310547
19	12751.8019	0.04492203	0.98225675	116.372009
20	12849.162	0.04921594	0.99477263	127.336958
21	13043.4783	0.05261667	0.99317044	135.810387
22	11981.2467	0.04986638	0.99627734	130.619805
23	11581.0675	0.04820812	0.99678008	127.133458
24	11055.9205	0.04660826	0.99527294	124.173152
25	11320.7547	0.04785	0.99645264	126.802246
26	12141.4746	0.05155957	0.99115578	134.717703
27	12096.7742	0.05297	0.9916523	138.497979
28	12450.3789	0.05804188	0.98431035	150.971343
29	12361.1609	0.06029986	0.99622056	157.043222
30	12332.4397	0.05987536	0.99361428	156.002285
31	11902.7083	0.05856145	0.9980221	153.590166
32	12378.902	0.06138159	0.98813526	159.819837
33	11931.5234	0.06020449	0.99117628	157.825488
34	12552.3013	0.06504333	0.98220035	168.944293
35	12880.3435	0.06747377	0.98184085	174.507216
36	13011.5029	0.06919217	0.97695799	178.662774
37	13320.4633	0.07165725	0.96962966	184.363283
38	13888.8889	0.07399	0.96631067	189.236381
39	14027.2413	0.07536565	0.94409117	192.49865
40	14523.2583	0.07849884	0.9416611	199.61467
41	14265.0403	0.07895348	0.9532549	201.221978

42	15391.4789	0.08365377	0.94159808	211.307413
43	16342.9654	0.08727884	0.92930854	219.133828
44	16530.9056	0.08968594	0.93810716	224.93749
45	16882.7991	0.09028319	0.93228485	226.006605
46	16487.4552	0.08886522	0.95673342	222.933238
47	18177.0285	0.09196478	0.94968174	228.83841
48	18424.5661	0.09286087	0.94668534	230.837367
49	18518.5185	0.09384667	0.9509195	233.201988
50	18821.6039	0.09412638	0.9504883	233.628421
51	20204.978	0.09539928	0.95780363	235.706153
52	21415.27	0.09699623	0.9661652	238.868449
53	22215.0676	0.09759812	0.95531061	239.902461
54	22380.7979	0.09554145	0.98537018	234.762238
55	26325.8298	0.09959522	0.98663818	243.103591
56	23381.9044	0.09797348	0.98057917	240.253304
57	22855.2501	0.09594536	0.98972231	235.521554
58	24784.4828	0.09780478	0.9827502	239.261459
59	21826.0244	0.09234289	0.98708346	227.184935
60	23009.961	0.09398306	0.99238182	230.633298
61	22826.087	0.09246667	0.99039784	226.995628
62	23014.8048	0.09273158	0.98848482	227.559999
63	24207.4928	0.09212024	0.97439307	225.567378
64	22310.0537	0.08982284	0.98847388	220.744412

titusville							
time	depth	sed.rt.	y^2	x^2	xy		
413	474		224676	170569	195762	ΣXi=	14868
826	800	0.002406	640000	682276	660800	ΣYi=	13022
1239	1168	0.002718	1364224	1535121	1447152	ΣXi^2=	34796076
1652	1522	0.002613	2316484	2729104	2514344	ΣYi^2=	25462996
2065	1810	0.002125	3276100	4264225	3737650	ΣXiYi=	29720306
2478	2168	0.002642	4700224	6140484	5372304	X(mean)=	1858.5
2891	2402	0.001727	5769604	8357881	6944182	Y(mean)=	1627.75
3304	2678	0.002037	7171684	10916416	8848112		
slope=	0.770379	ft/ky	0.009245	in/y	0.234812	mm/y	
intercept=	196						
r =	0.998267						
r^2 =	0.996537						

nursery							
time	depth	sed.rt.	y^2	x^2	xy		
413	584		341056	170569	241192	ΣXi=	14868
826	894	0.002288	799236	682276	738444	ΣYi=	12754
1239	1170	0.002037	1368900	1535121	1449630	ΣXi^2=	34796076
1652	1486	0.002332	2208196	2729104	2454872	ΣYi^2=	23661908
2065	1766	0.002066	3118756	4264225	3646790	ΣXiYi=	28583730
2478	2008	0.001786	4032064	6140484	4975824	X(mean)=	1858.5
2891	2262	0.001875	5116644	8357881	6539442	Y(mean)=	1594.25
3304	2584	0.002376	6677056	10916416	8537536		
slope=	0.681252	ft/ky	0.008175	in/y	0.207646	mm/y	
intercept=	328.1429						
r =	0.999392						
r^2 =	0.998785						

princeton							
time	depth	sed.rt.	y^2	x^2	xy		
413	604		364816	170569	249452	ΣXi=	6195
826	924	0.002362	853776	682276	763224	ΣYi=	6304
1239	1206	0.002081	1454436	1535121	1494234	ΣXi^2=	9381295
1652	1596	0.002878	2547216	2729104	2636592	ΣYi^2=	9116920
2065	1974	0.00279	3896676	4264225	4076310	ΣXiYi=	9219812
						X(mean)=	1239
						Y(mean)=	1260.8
slope=	0.82615	ft/ky	0.009914	in/y	0.251811	mm/y	
intercept=	237.2						
r =	0.998004						
r^2 =	0.996011						

TABLE 6: Listing of the time-depth picks for the 400 ky cycles seen in each of the three reflectivity series. Additionally, linerar regression lines with correlation coefficients are shown.

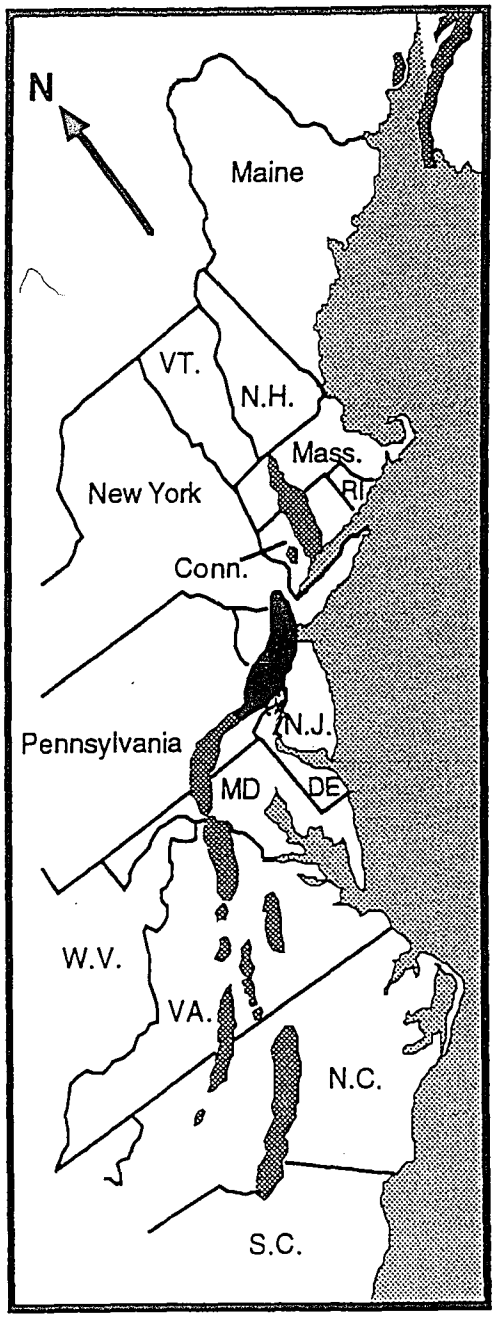

FIGURE 1: A map of the eastern coast of North America. The shaded regions are early Mesozoic rift basins identified by surface exposure. The black region is the Newark Rift Basin. Note that the general trend of the basins parallels the final rifted axis.

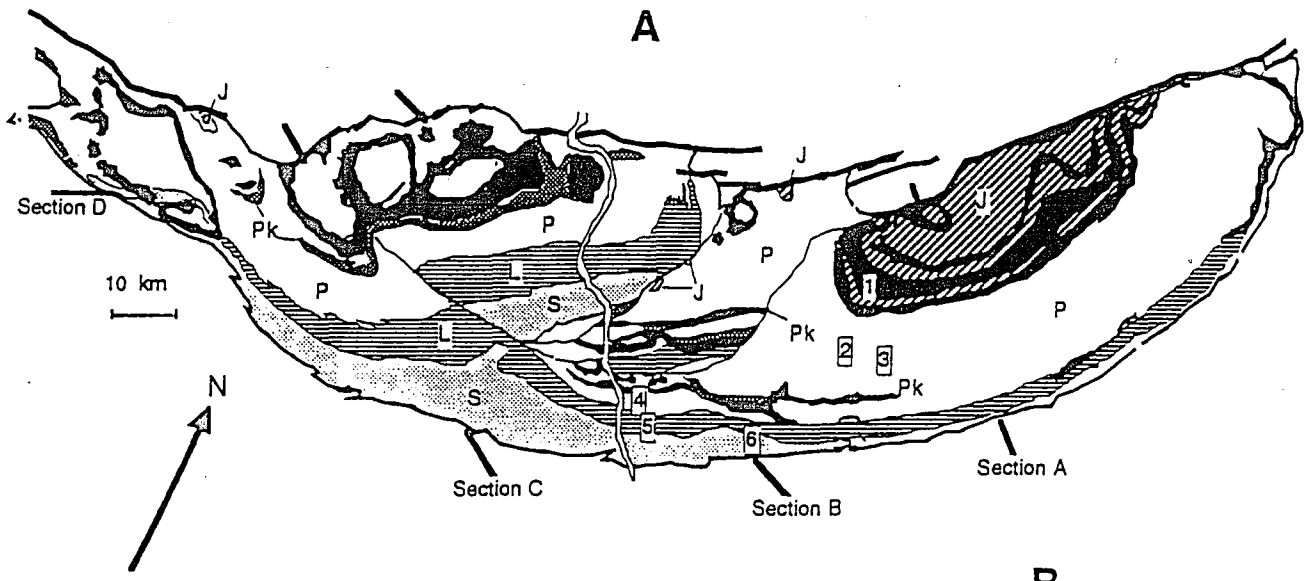

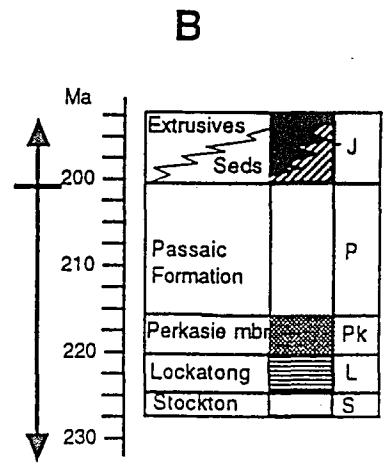

FIGURE 2: The Newark basin

A. a simplified geologic map (after Schlische, 1991) showing the areas discussed in the text. The Lamont cores are numbered as follows:

1. Martinsville
2. Somerset
3. Rutgers
4. Titusville
5. Nursery Road
6. Princeton

Cross sections A-D are shown in **Figure 4.**

B. the major components of the Newark Supergroup in the Newark basin, correlated with age (from Olsen, 1988). Symbols shown in the right hand column correlate with symbols on map in A.

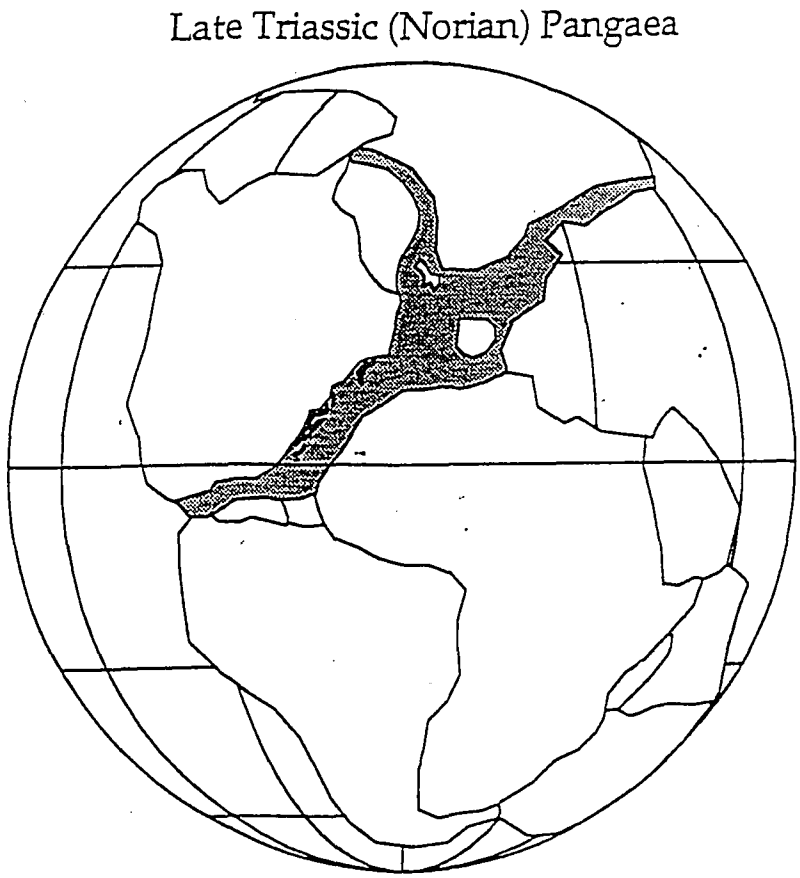

FIGURE 3: Simplified map showing the near-equitorial location of the North American East Coast rift basins during the Late Triassic (from Reynolds, 1994). The pole-to-pole coverage of Pangea is a suspected cause of strong equitorial monsoonal climates.

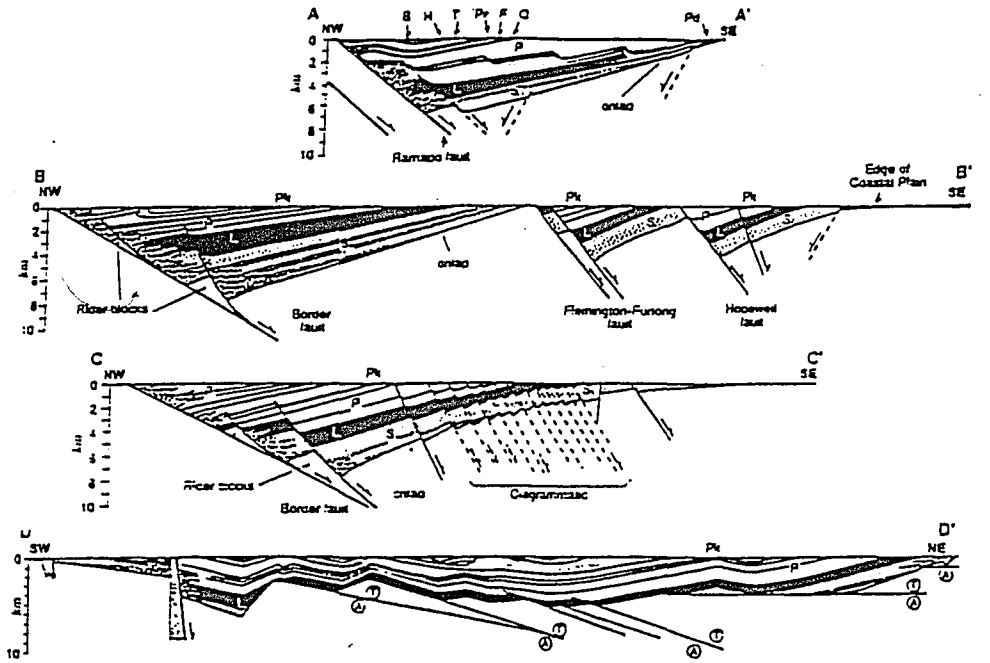

FIGURE 4: Representative cross sections of the Newark Basin (see **Figure 2** for locations). Transverse lines A-A', B-B', and C-C' illustrate the asymmetric nature of the basin. Longitudinal section D-D' shows the overall synclinal shape of the basin. No vertical exageration in any section. From Schlische, 1990.

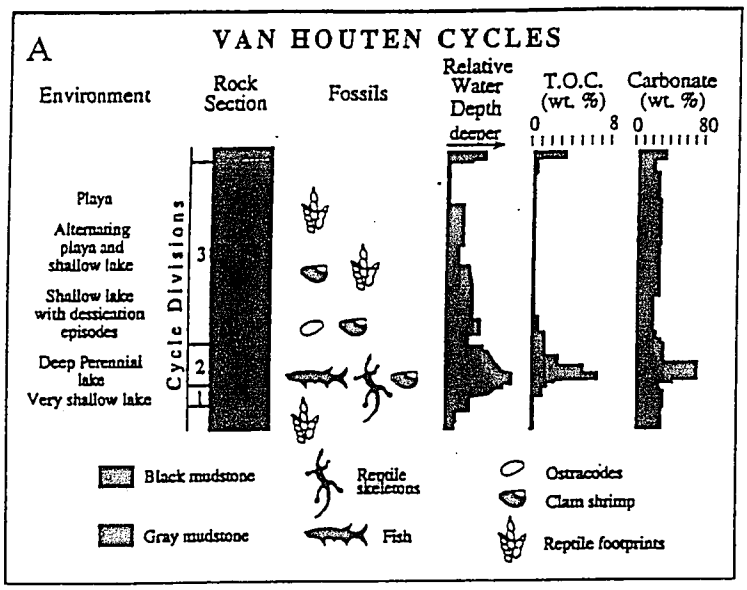

FIGURE 5: Characteristics of a single Van Houten cycle (from playa to deep perennial lake) typical of the Newark Rift Basin (Olsen, 1986). The cycles are caused by the 21,000 year cycles related to the astronomoical influences upon the precession constant of the Earth.

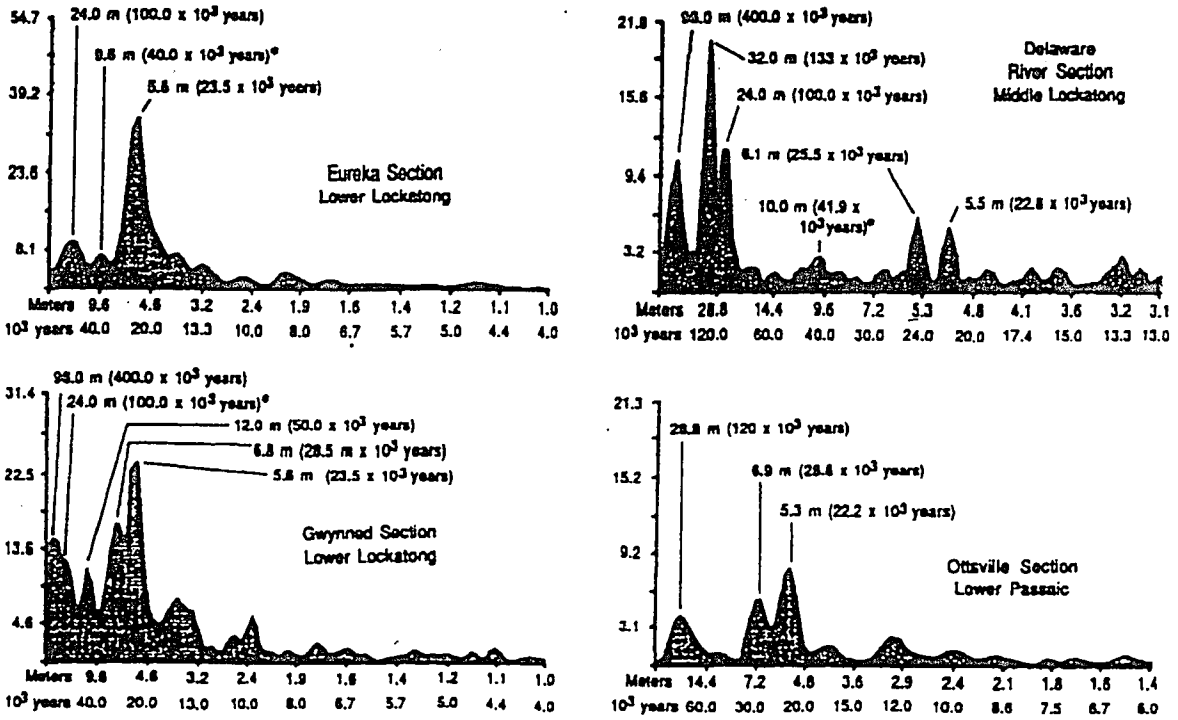

from Olsen, 1986

FIGURE 6: Power spectra of the sections of the Lockatong and Passaic examined by Olsen (1986). In this instance, the "peaks" represent locations where a high number of certain cycles were repeated. The vertical axis is the correlated amplitude of the Fourier analysis. Note the two sets of numbers given for the horizontal axis. The first set denote sediment thickness. Thus the number corresponding with a peak is the thickness which is repeated throughout the section. The second set of numbers is that derived when Olsen (1986) used a sedimentation rate of 0.7382 ft/ky (22.2 cm/ky) to convert from sediment thickness to time. This assumption assumes a constant sedimentation rate and is based on varve counting within the microlaminated sequences.

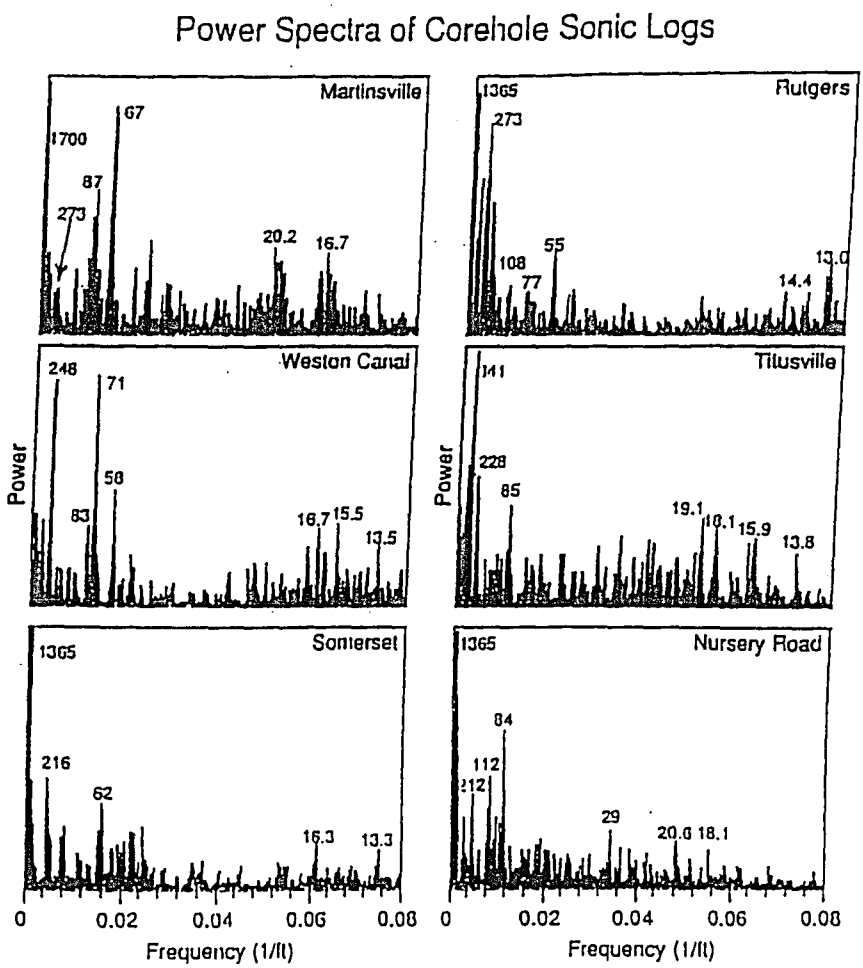

FIGURE 7: Power spectra of corehole sonic logs by Olsen et al. (in press). The depth peaks shown by the spectral analysis should correspond to: 1450 ft for the 2 My cycles, 300 ft for the 413 ky cycles, 95 ft for the 130 ky cycles, and 15 ft for the 21 ky cycles. Note the good correlation with the majority of the logs, and the 'smearing' which takes place to the peaks of the smaller cycles due to fluctuations in sedimentation rates.

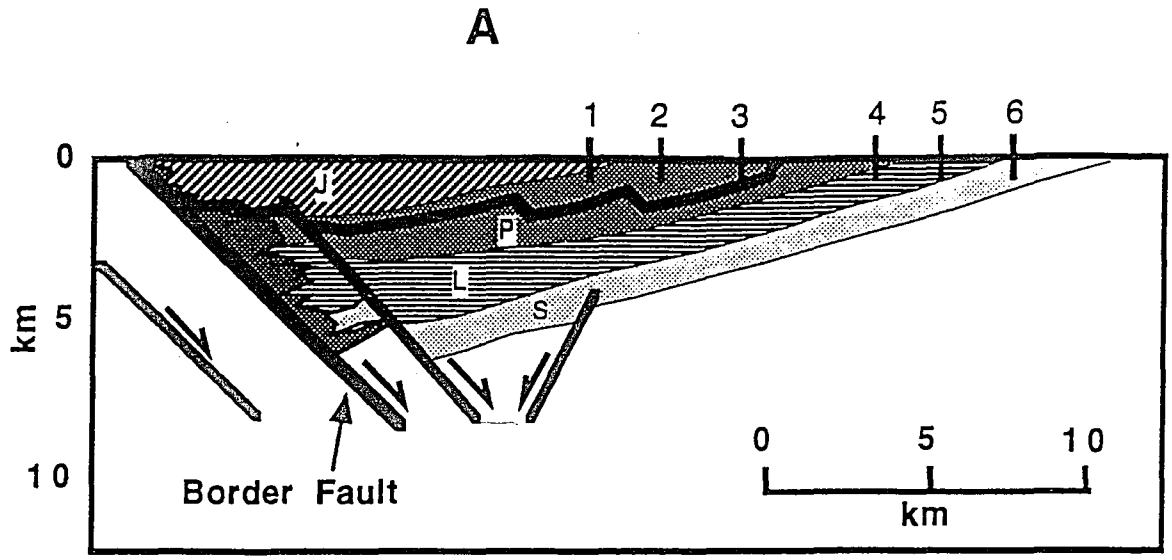

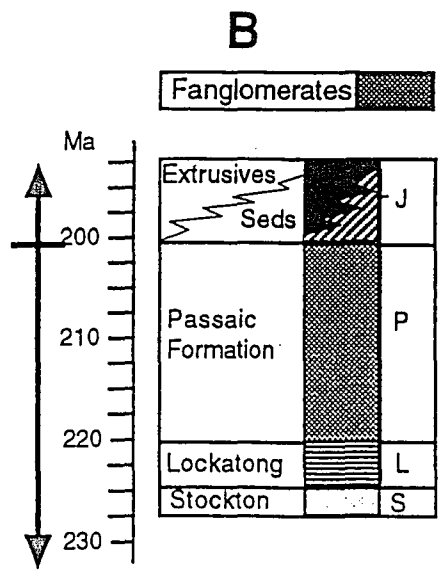

Figure 8 - Schematic location of Lamont coreholes.

A. a generalized cross section showing the areas discussed in the text (from Meltzer et al., 1991). Note classic half-graben shape, dipping strata, and the placement of cores to sample entire basin stratigraphy.

Lamont cores are as follows:

1. Martinsville
2. Sommerset
3. Rutgers
4. Titusville
5. Nursery Rd.
6. Princeton

B. the major components of the Newark Supergroup in the Newark basin, correlated with age (from Olsen, 1988).

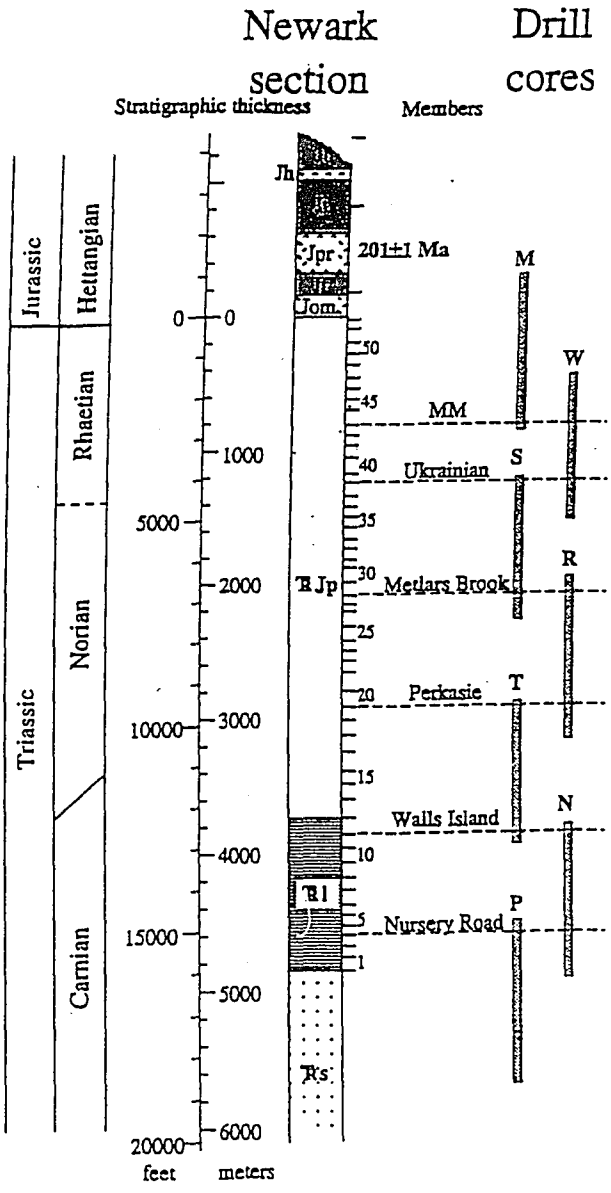

FIGURE 9: Stratigraphy of the Newark Basin cores (from Olsen, submitted). The cores of interest to this study are: T - Titusville, N - Nursery Road, and P - Princeton.

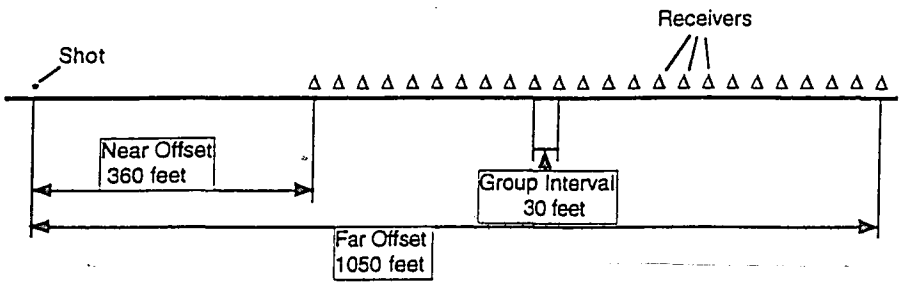

FIGURE 10: Shot and receiver geometry for the Washington's Crossing and Princeton seismic profiles. Eash shot is collected as one field record, the next shot, moved 30 ft further along the transect, represents the next sequential field record, etc.

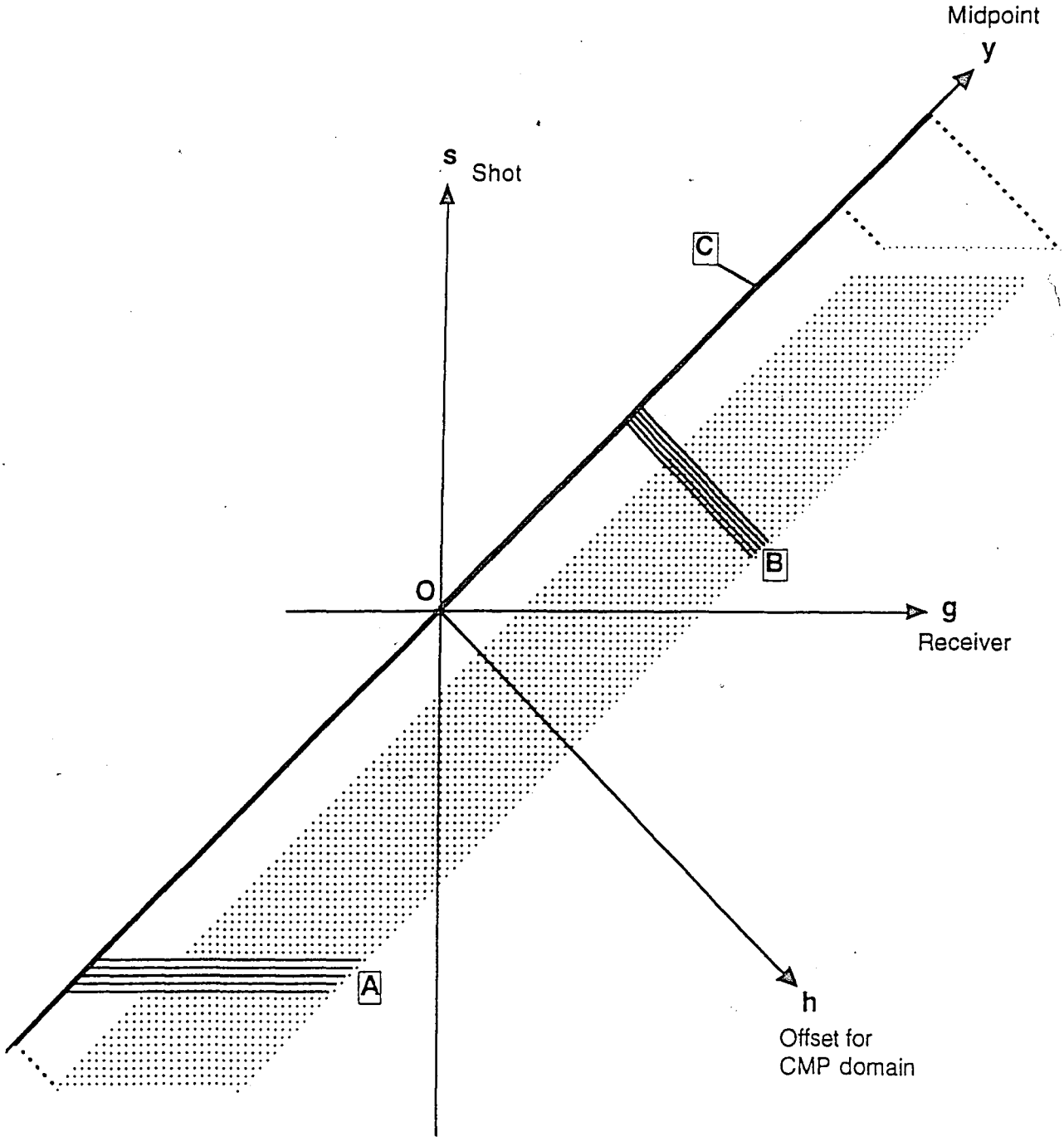

FIGURE 11: A stacking chart for Washington's Crossing Line 2 (110 shotpoints). Each dot represents a receiver location. **A** is the shot domain and is in the S-G (shot-receiver) coordinate plane. Traces that fall along line A = shot gather. **B** represents common midpoint domain, the midpoint being the projection onto line. Traces that fall along line B = 1 CMP gather. **C**. Note for future reference the shot gathers composed of 24 receivers (traces) are sorted into common midpoint gathers of 12 traces.

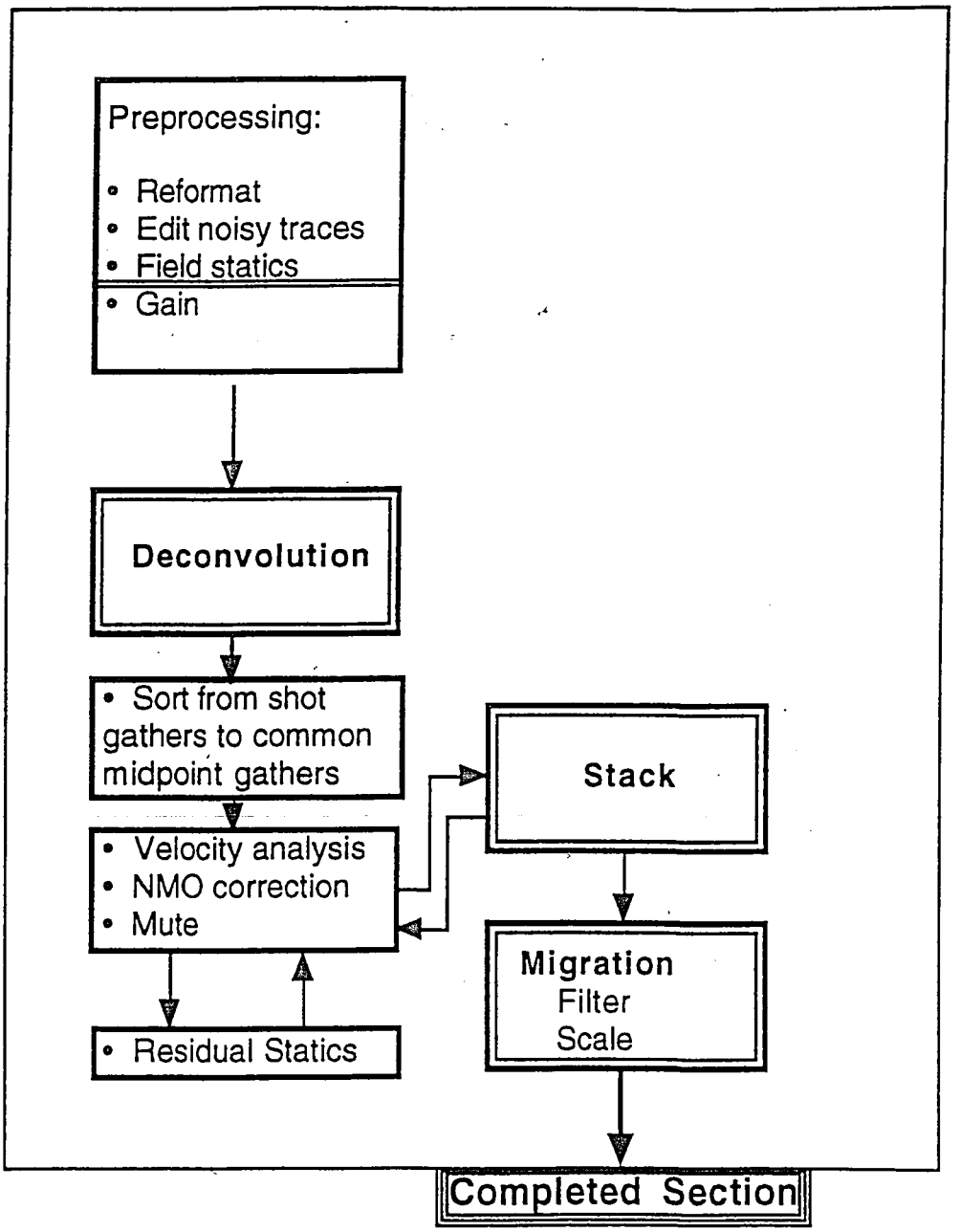

FIGURE 12: Generalized seismic data processing routine. Note that returning arrows represent possible iterations.

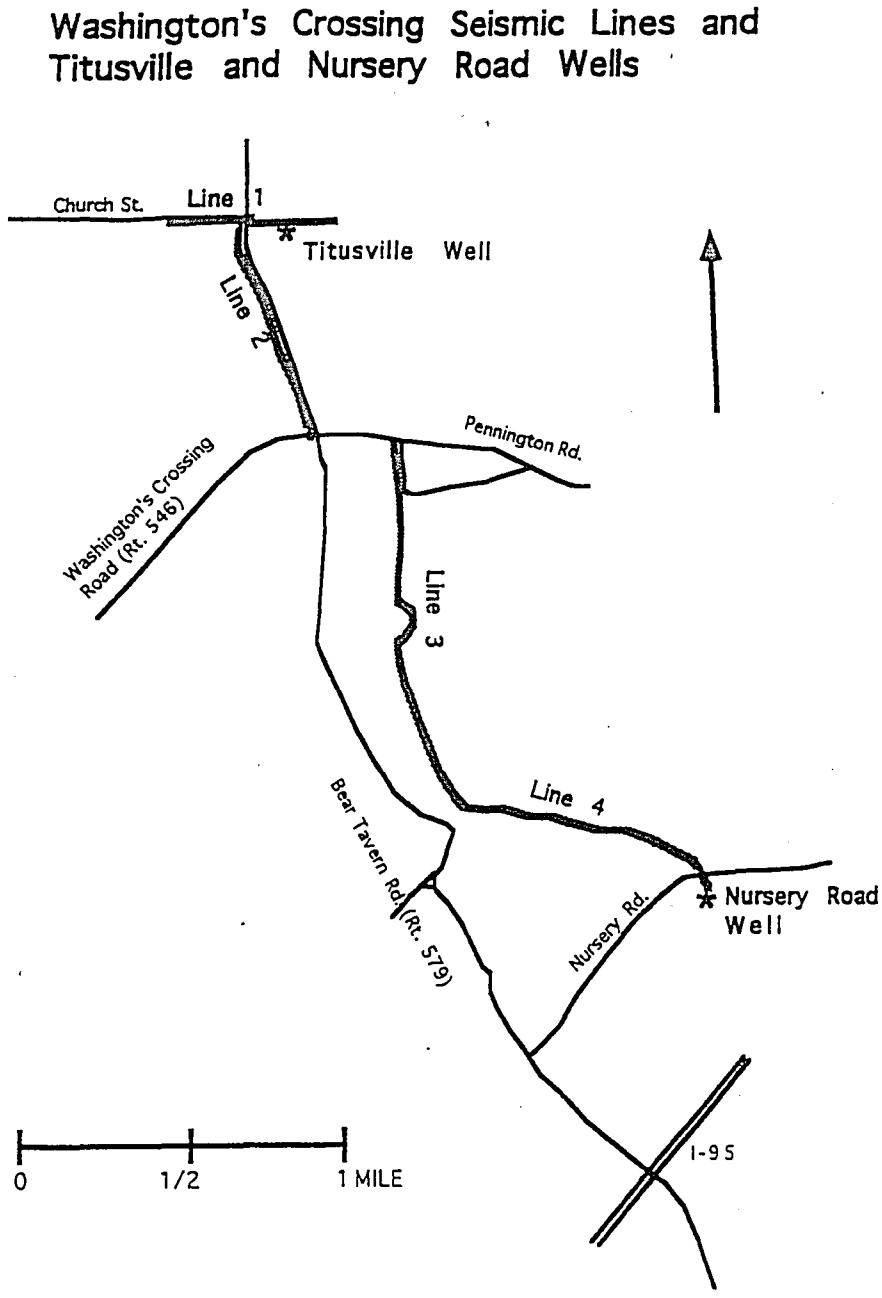

FIGURE 13: Location map of the Washington Crossing seismic lines and the Titusville and Nursery Road core hole locations. Washington's Crossing Line 3 & 4 were not examined in this study (University of Deleware).

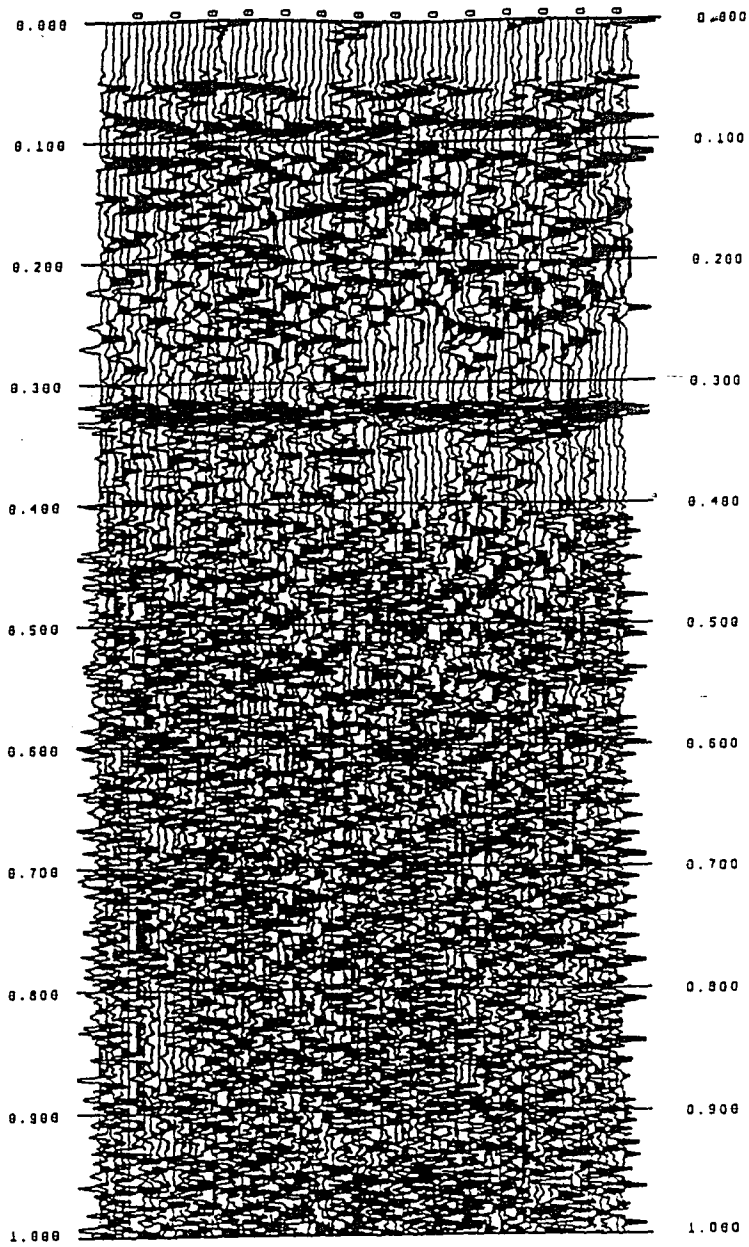

FIGURE 14: A scaled (AGC, 0.13 second window) and filtered (5 to 360 Hz) near trace display of Washington's Crossing Line 1. The high amplitude signal at 0.32 seconds is the air wave. The upper 0.26 seconds of the data is characterized by refracted arrivals. Note the lack of coherent reflections.

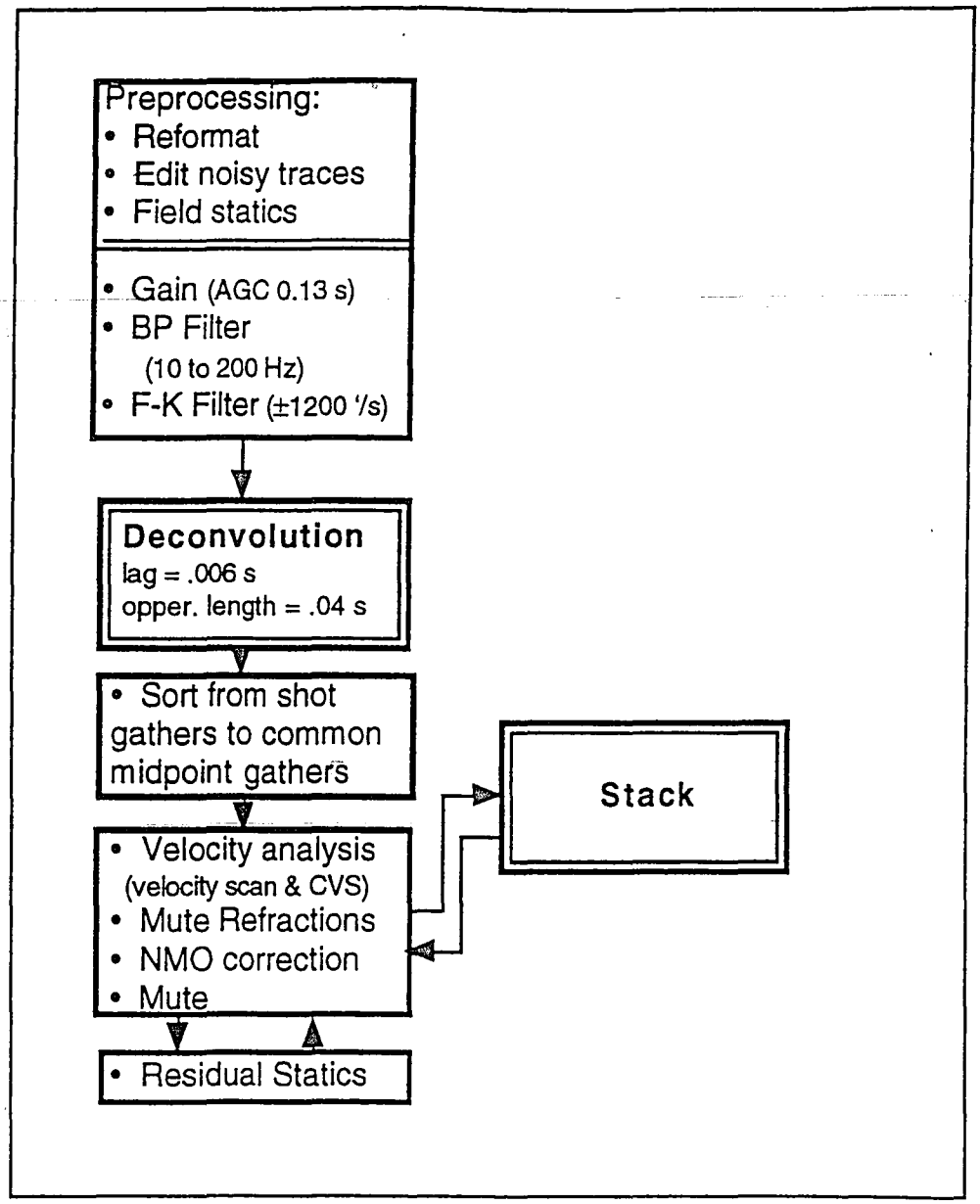

FIGURE 15: Processing scheme for Washington Crossing Lines 1 & 2.

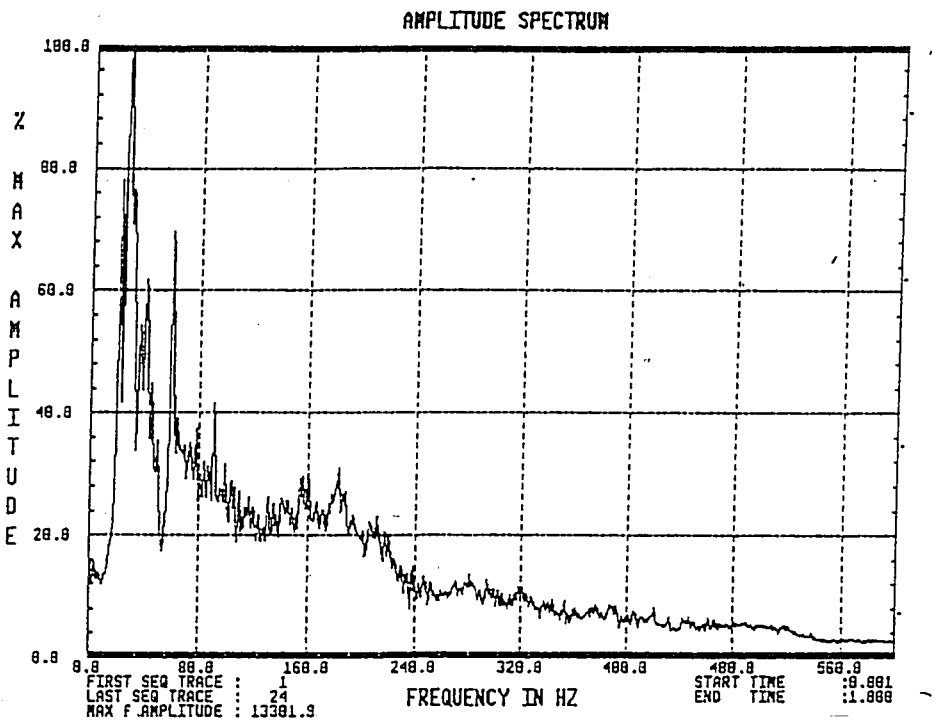

FIGURE 16: An amplitude spectra of field record 10 from Washington Crossing Line 1. Frequencies up to 240 Hz contain signal above ambient noise level.

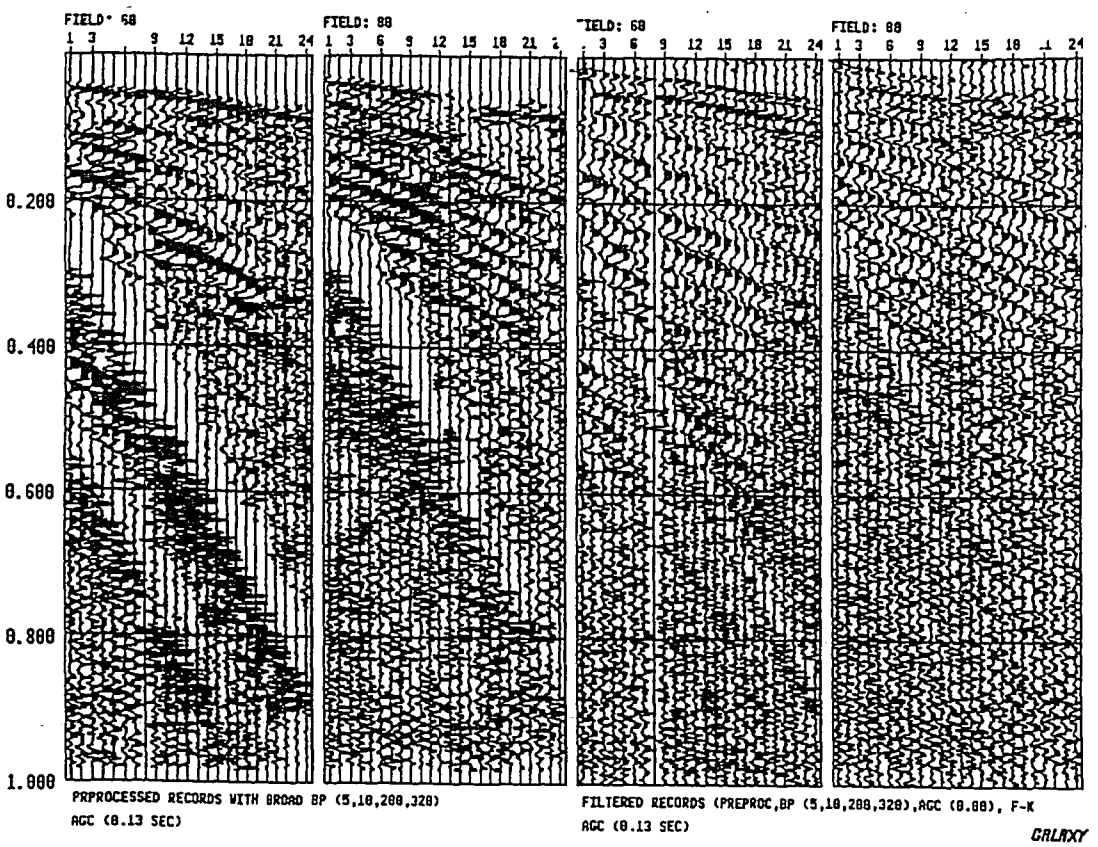

FIGURE 17: Plots from WCL1 of records 60 and 80 before and after f-k filtering. Note the reduced prominance of the air wave.

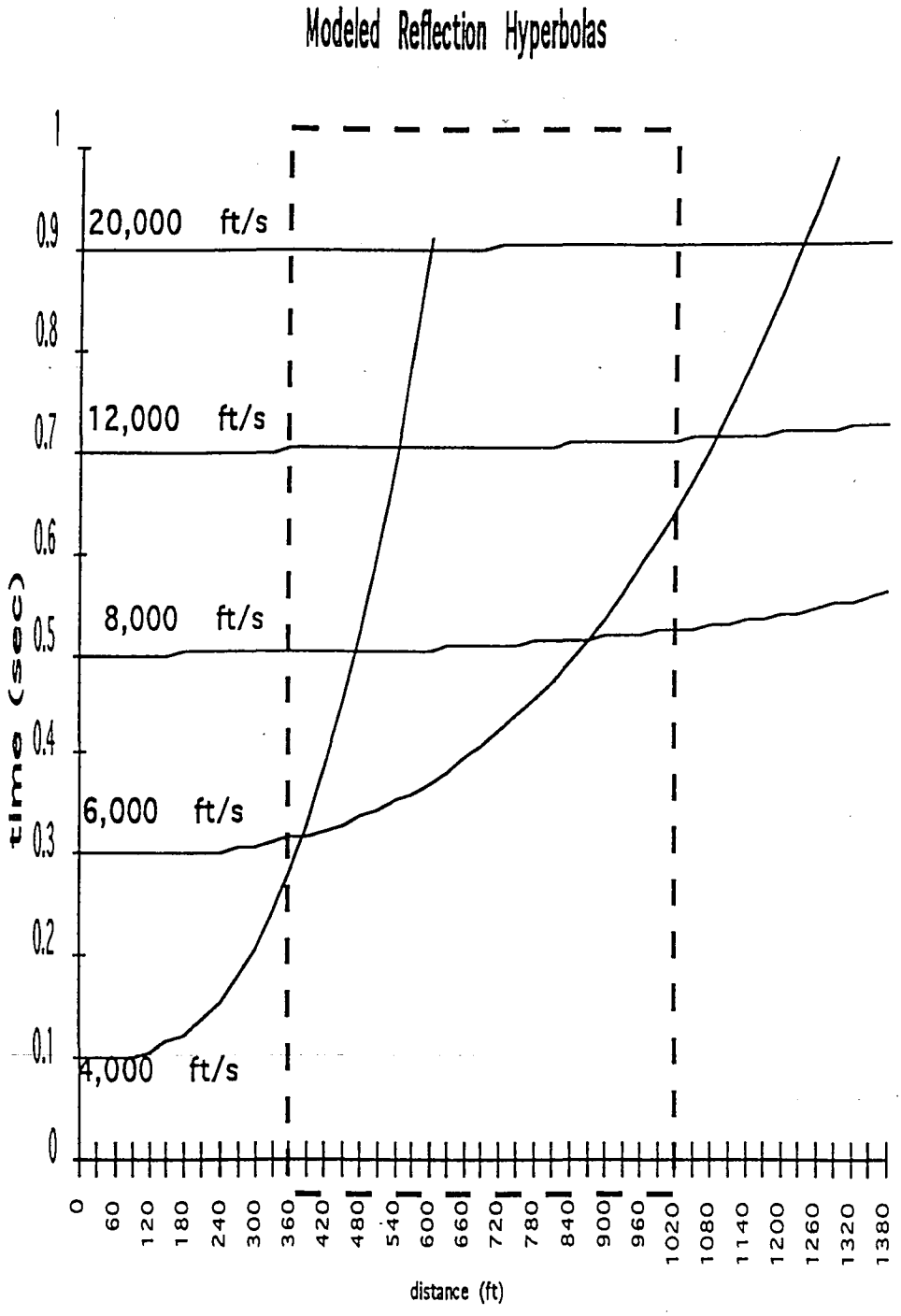

FIGURE 18: Hyperbola generated for various velocities demonstrating expected moveout times. The dashed box represents the offsets recorded by the shot geometry of the Washington Crossing and Princeton seismic lines.

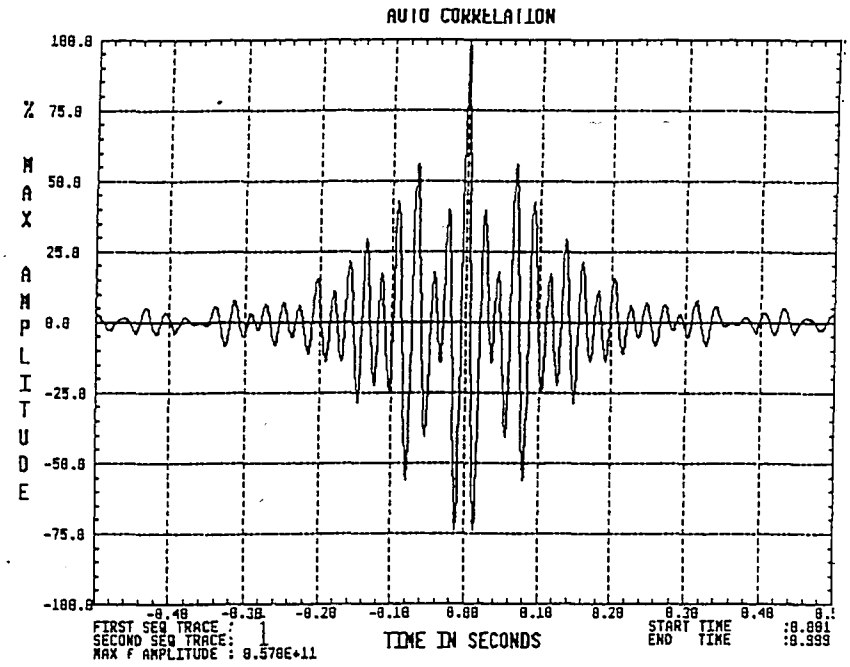

FIGURE 19: An autocorrelation plot from record 20 of WCL1. From time zero, the second zero crossing is used as the first estimation of the deconvolution opperator length.

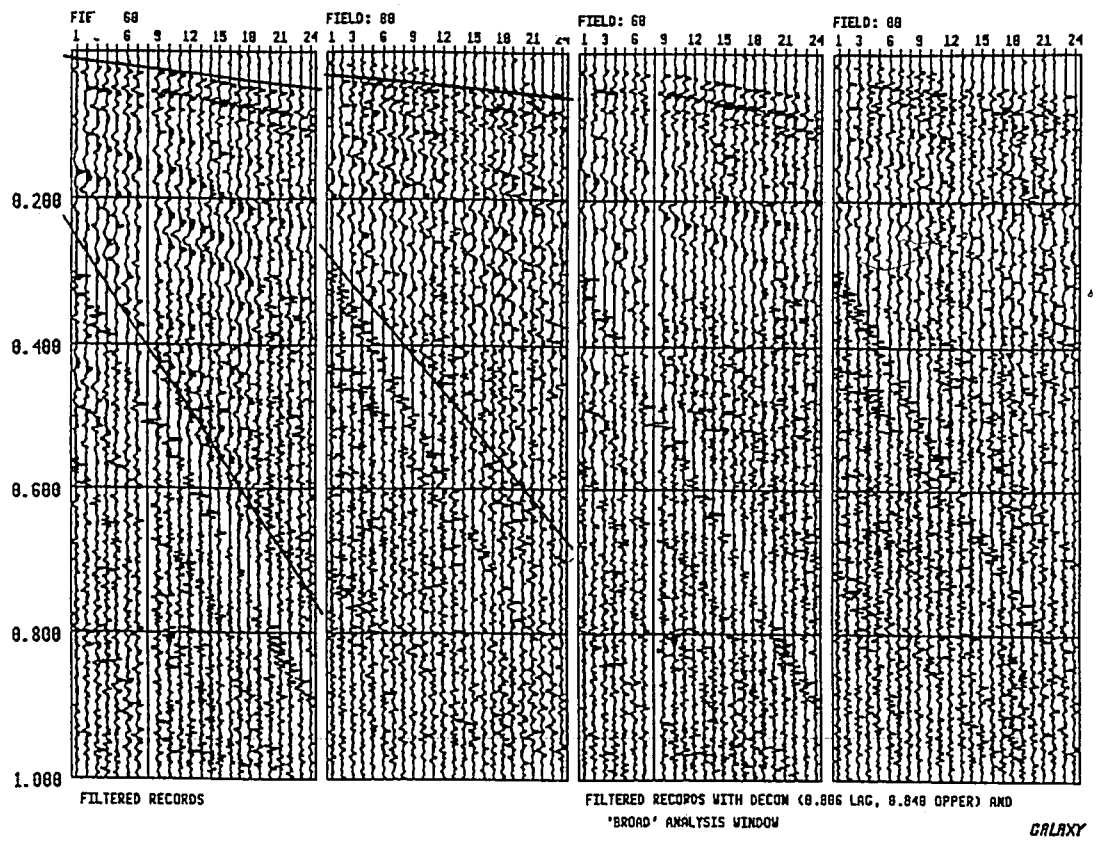

FIGURE 20: Plots from WCI 1 before and after deconvolution witha lag of 0.006 seconds and an opperator length of 0.04 seconds. The analysis window for the deconvolution spans 0.1 to 0.4 seconds. Note the reduction of refraction multiples and lack of reflection hyperbolas. All records plotted with AGC (0.13 sec window).

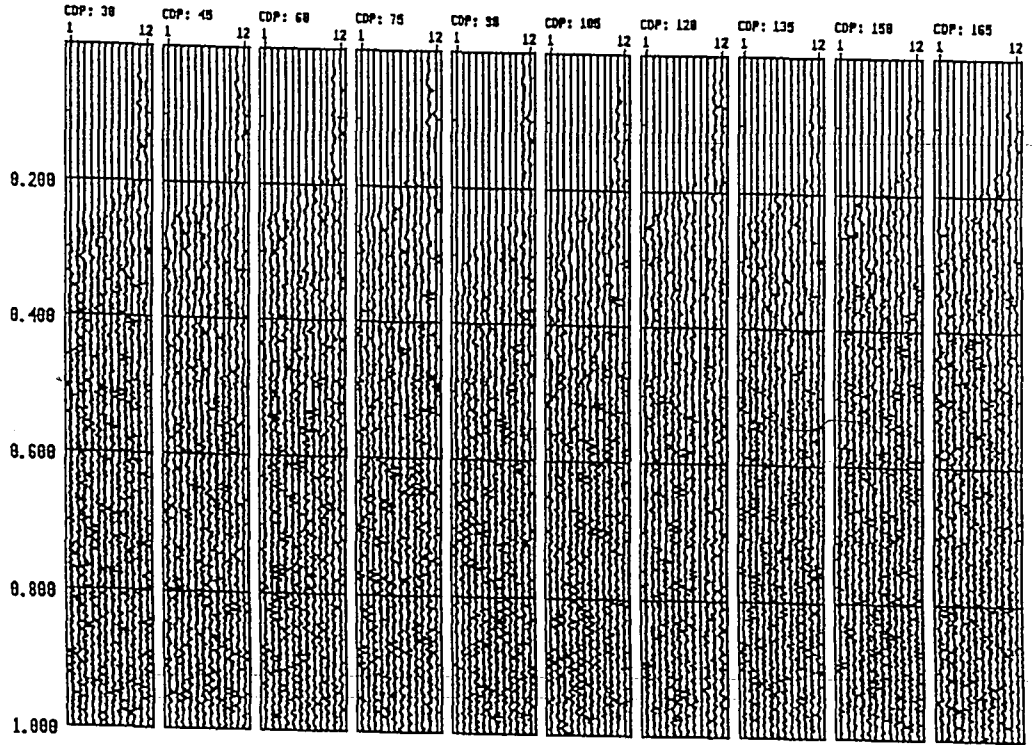

FIGURE 21: WCL1 after common midpoint sorting, deconvolution, and a mute to remove refracted arrivals. The mute is necessary in order to prevent stacking in refracted signal in velocity analyses. All gathers are plotted with AGC (0.13 sec window).

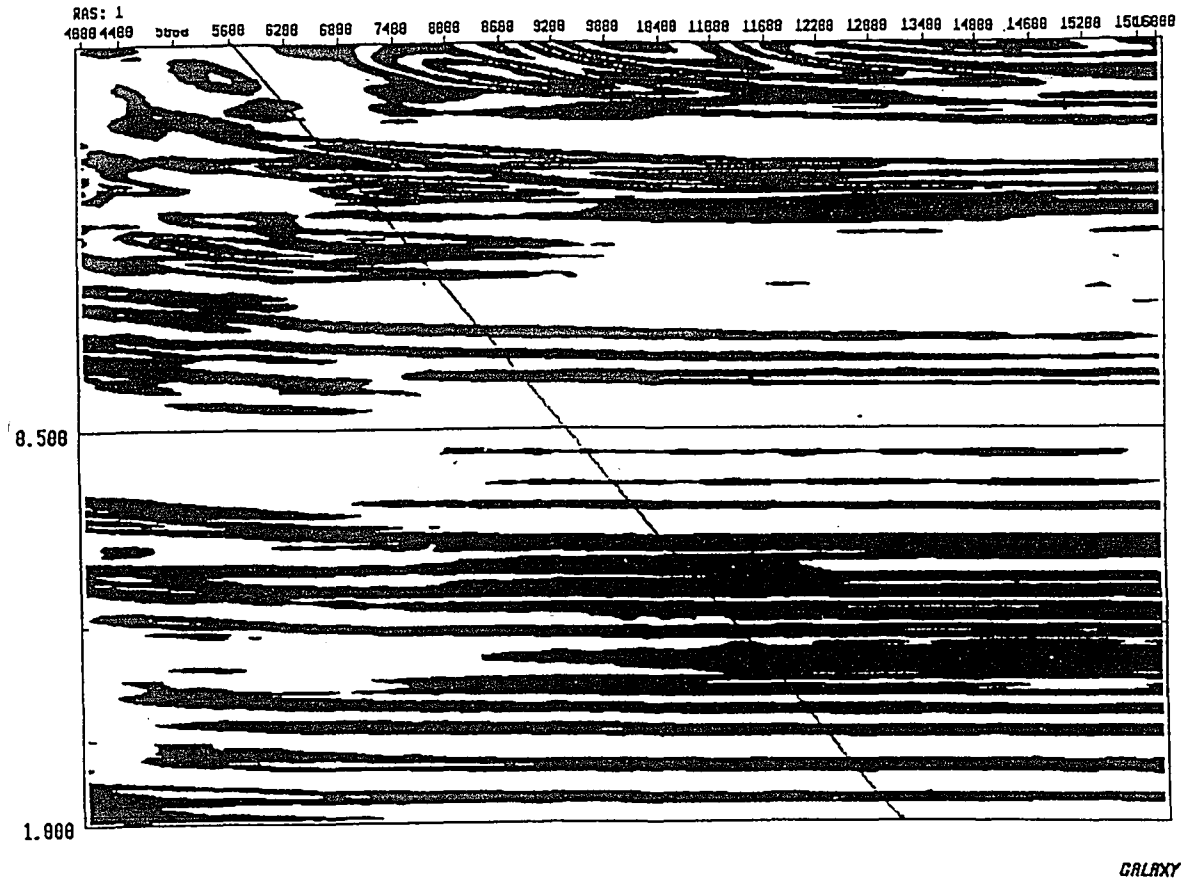

FIGURE 22: Velocity scan for WCL1 for common midpoint gather 27. The smearing of the high-semblance dark contours is an indication of a lack of coherent energy. The ruled line represents the best velocity function obtainable from this velocity scan.

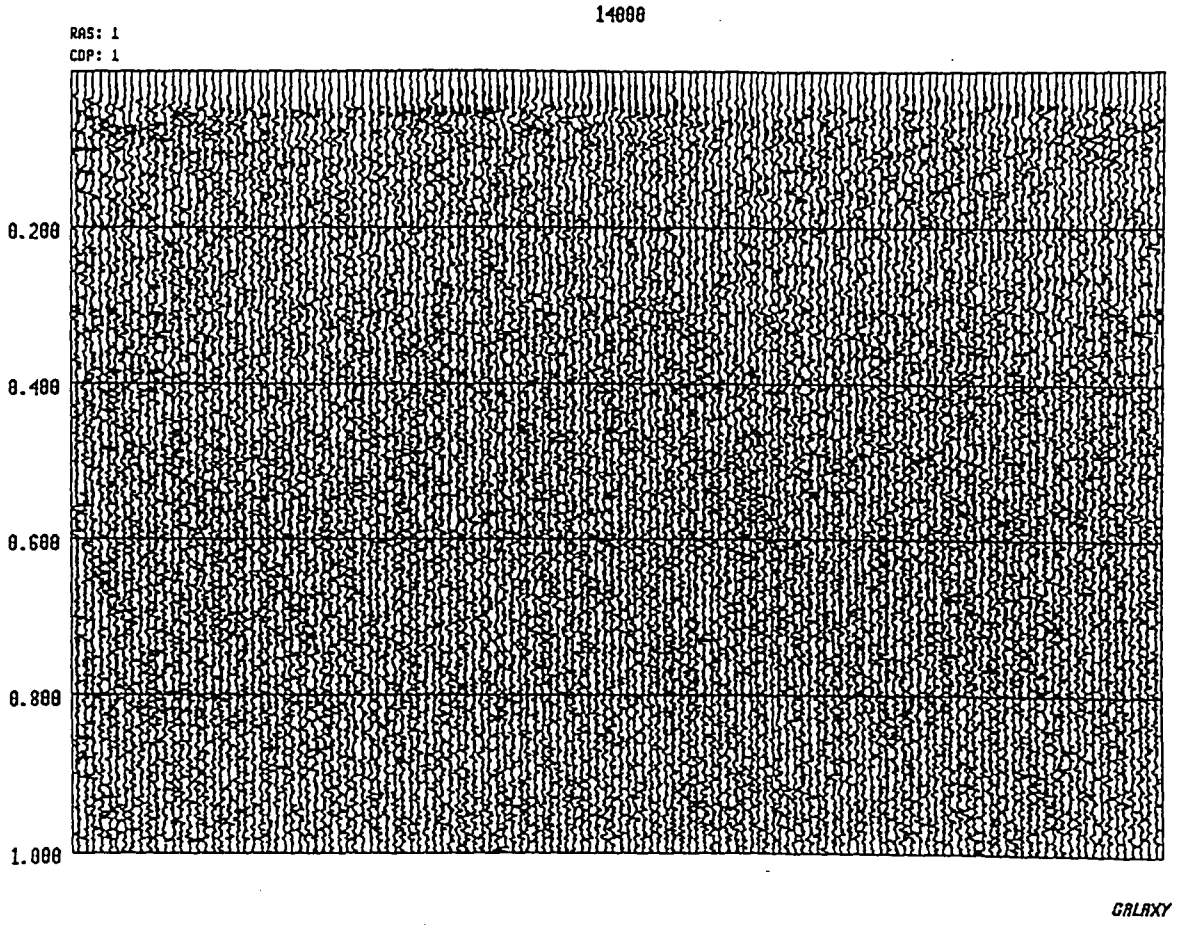

FIGURE 23: Constant velocity stack for WCL1 at 14,000 ft/s. Near surface refractions from near traces left live are the only horizons seen in this section. No reflections are identified. The other constant velocity stacks for this line look similar. Plotted with AGC (0.13 sec window).

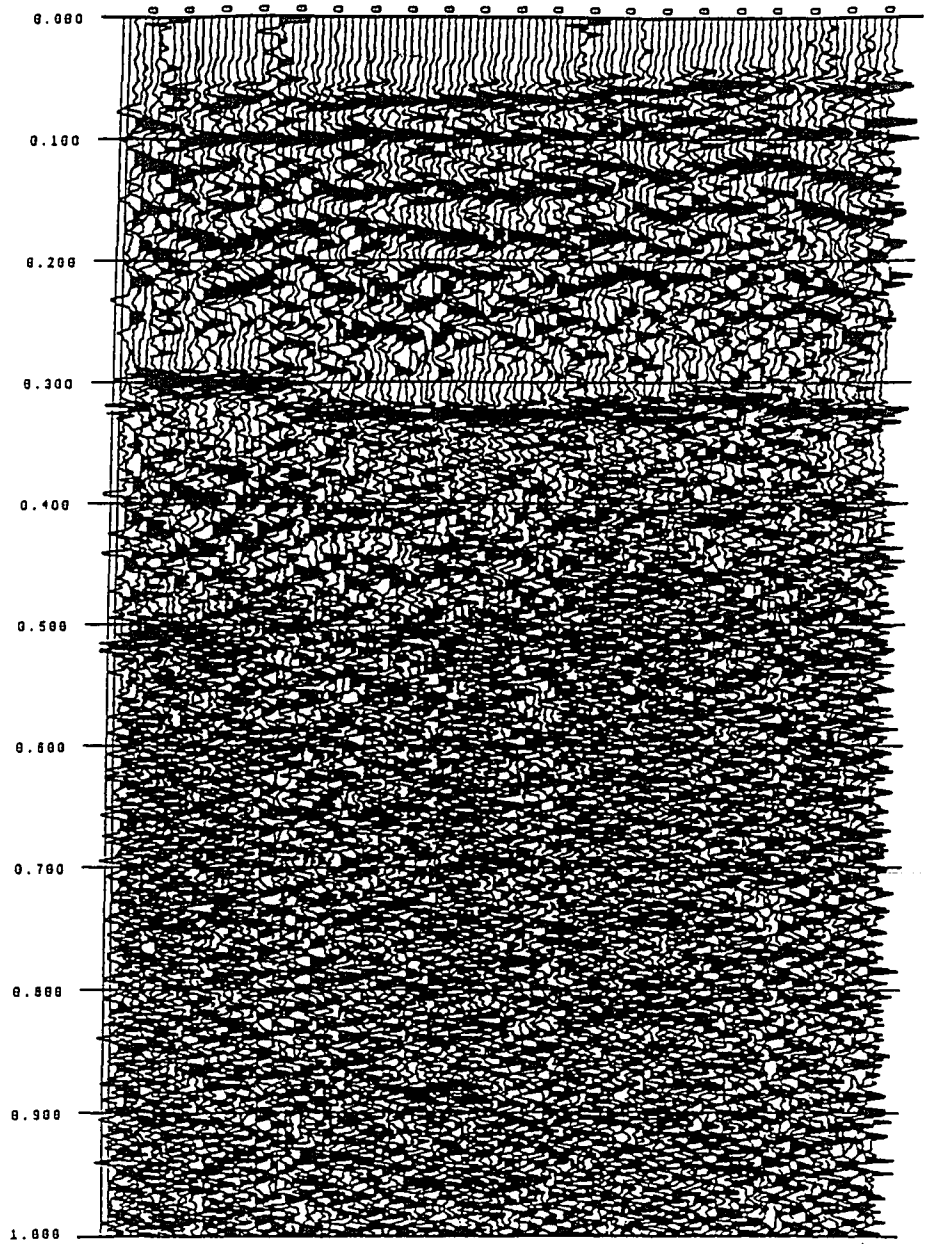

FIGURE 24: Near trace display of Washington Crossing Line 2. Note the similarities between this section and the near trace display of WCL1 (**Figure 14**). Plotted with BP filter (5,10,240,360) and AGC (0.13 sec window).

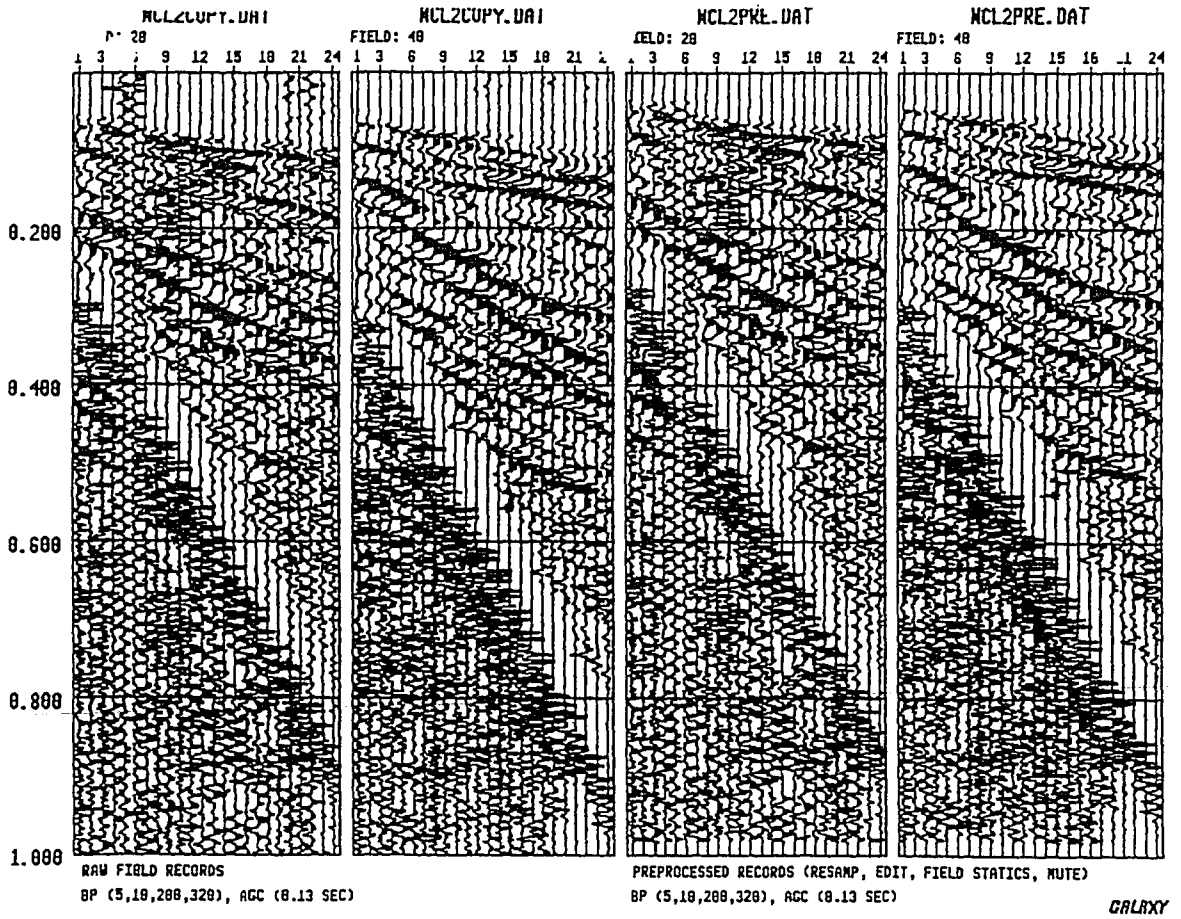

FIGURE 26: Comparison of WCL2 records 20 and 40 before and after editing, field statics, and electronic noise muting. Displayed with band-pass filter (5,10,200,320) and AGC (0.13 second window).

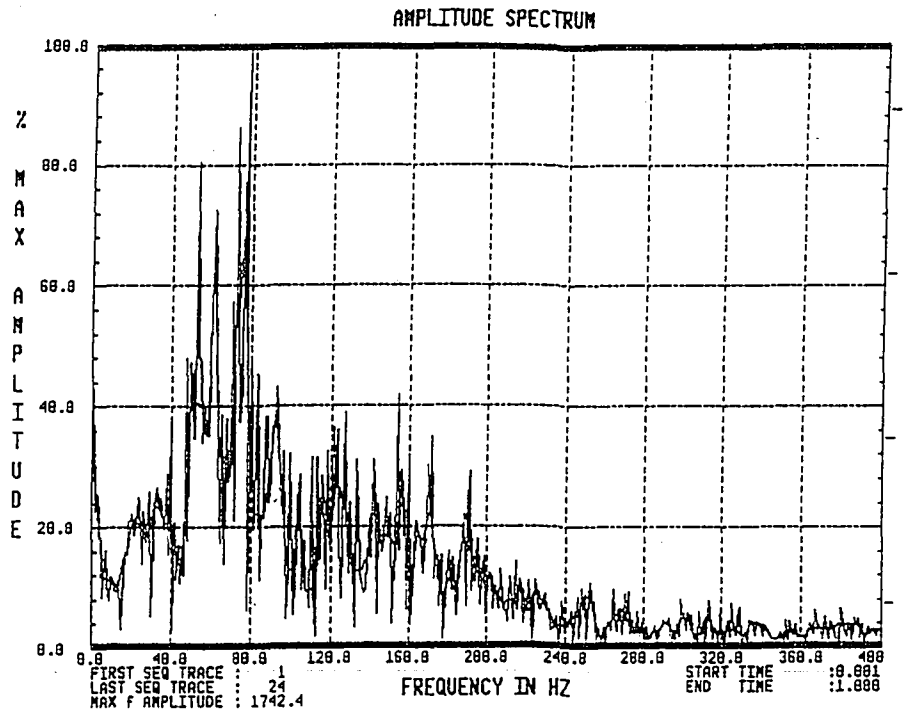

FIGURE 27: An amplitude spectra of field record 20 from Washington's Crossing Line 2. Frequencies up to 240 Hz contain signal above ambient noise level.

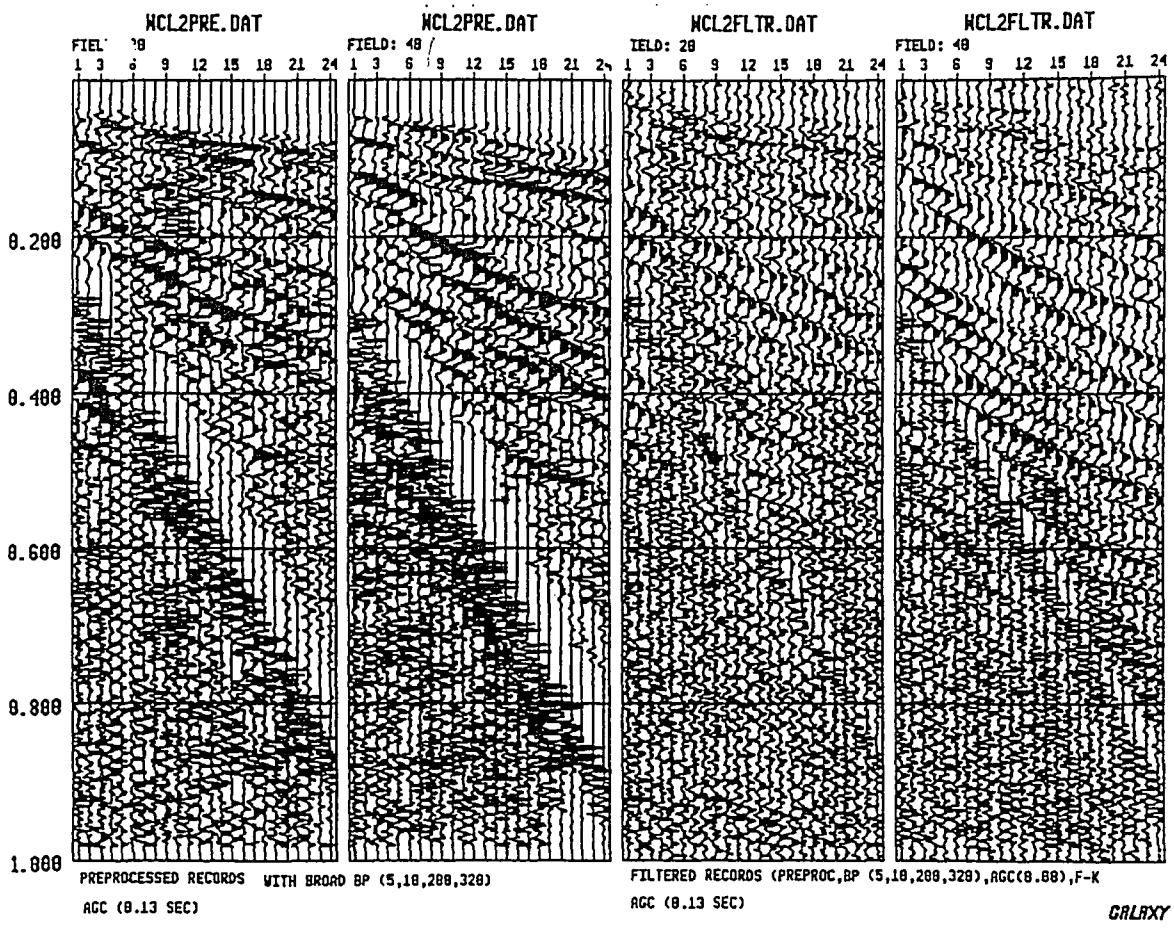

FIGURE 28: Plot from WCL2 of records 20 and 40 before and after f-k filtering. Note the reduced prominance of the air wave. Plotted with AGC (0.13 sec window).

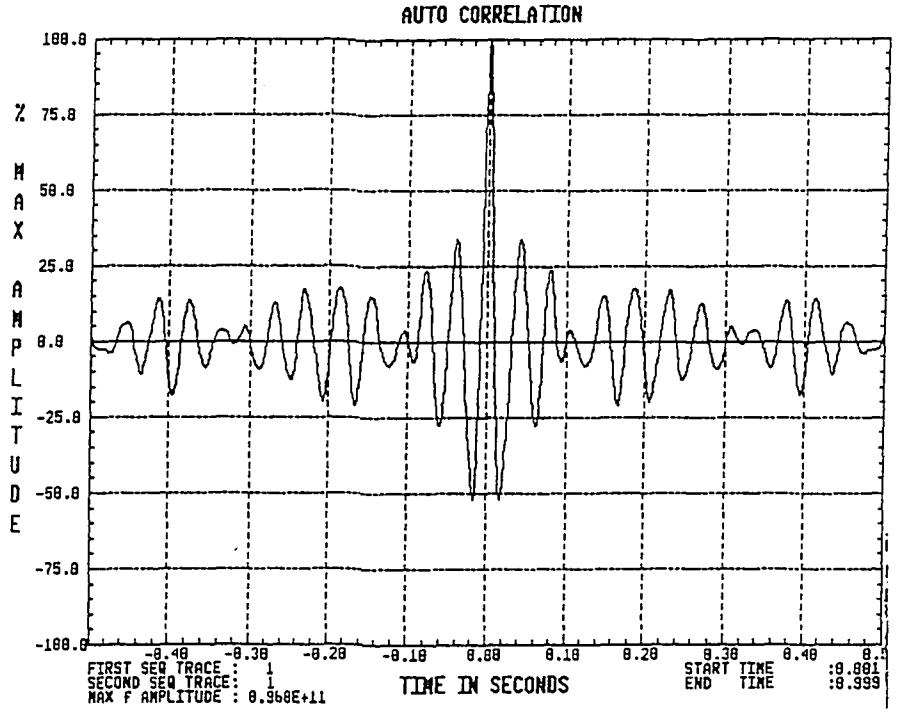

FIGURE 29: An autocorrelation plot from record 40 of WCL2. From time zero, the second zero crossing is used as the first estimation of the deconvolution opperator length.

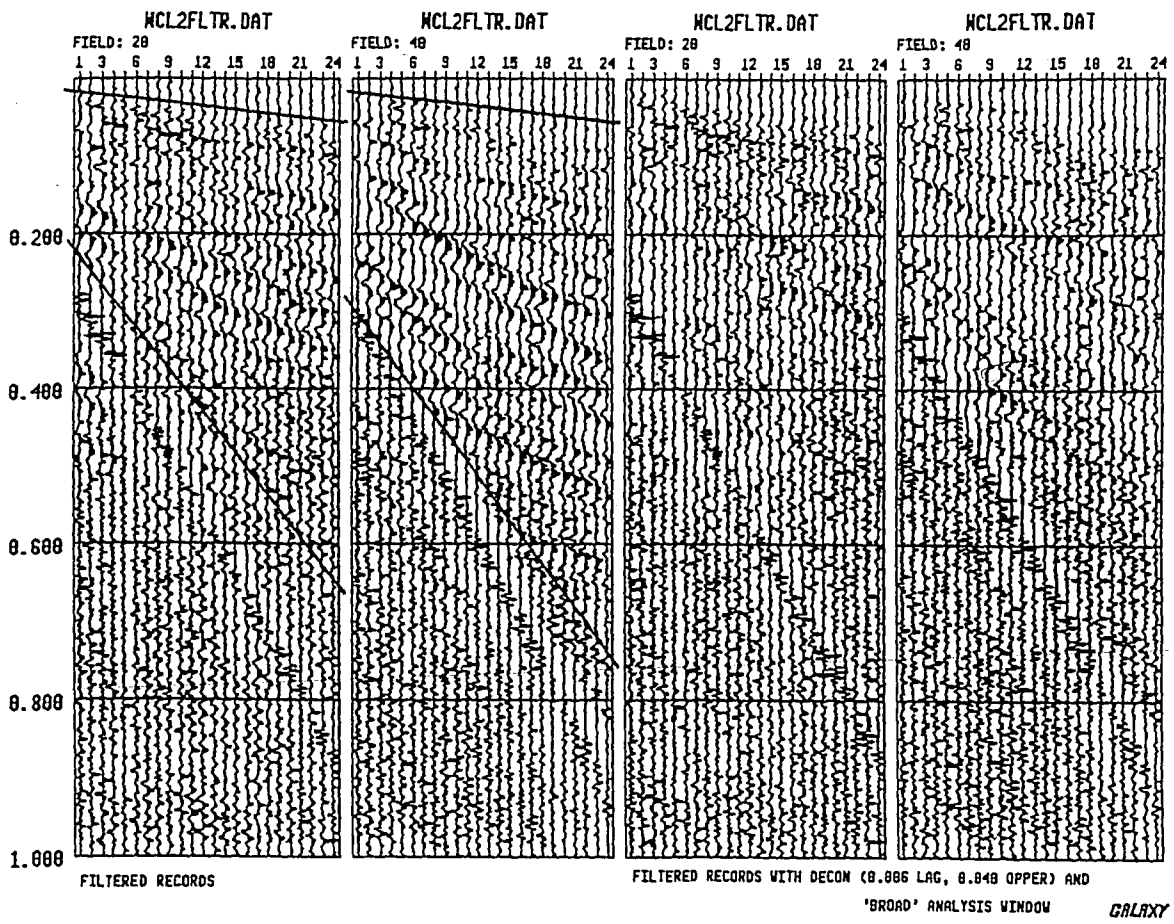

FIGURE 30: Plots from WCL2 before and after deconvolution with a lag of 0.006 seconds and an opperator length of 0.04 seconds. The analysis window for the deconvolution was chosen at every tenth record along the line, and is the area between the heavy lines. Note the reduction of refraction multiples and lack of reflection hyperbolas. Plotted with AGC (0.13 sec window).

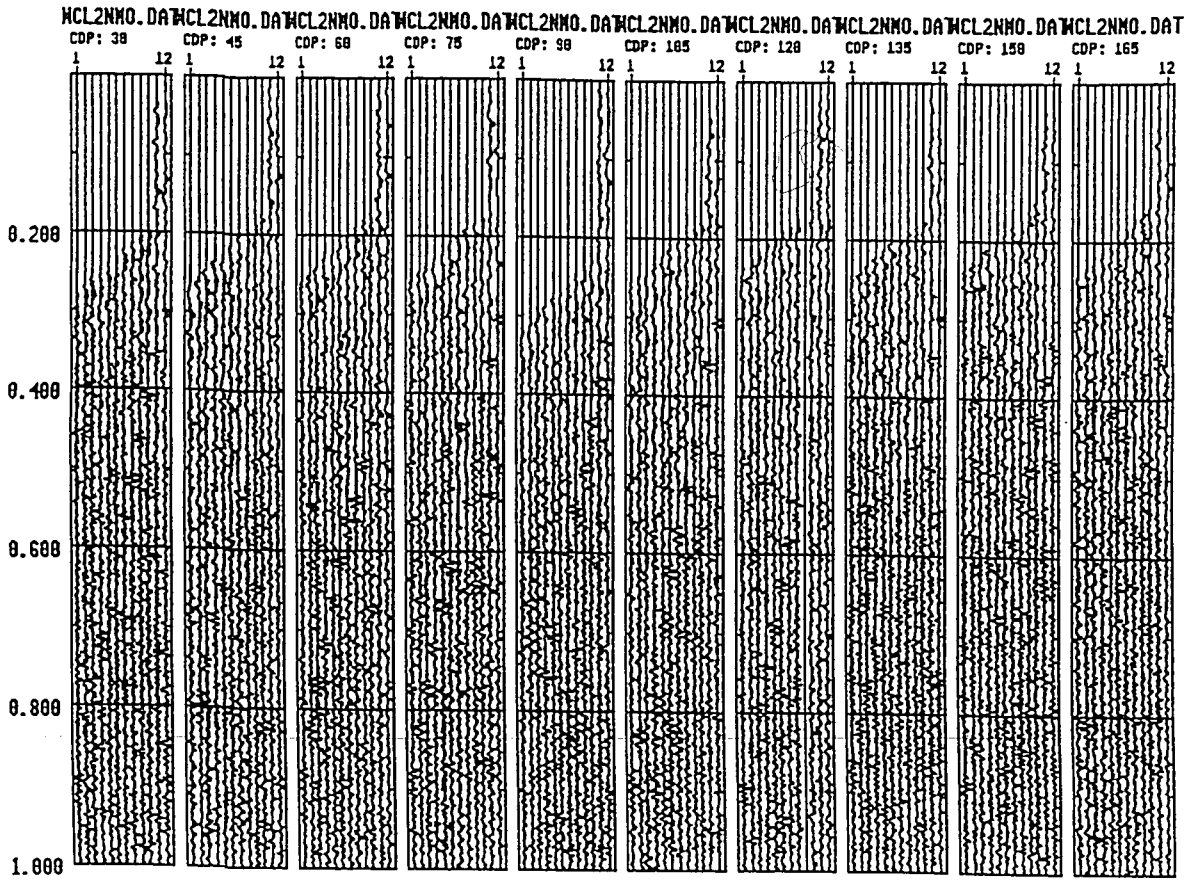

FIGURE 31: WCL2 after common midpoint sorting, deconvolution, and a mute to remove refracted arrivals. The mute is necessary in order to prevent stacking in refracted signal in velocity analyses. Plotted with AGC (0.13 sec window).

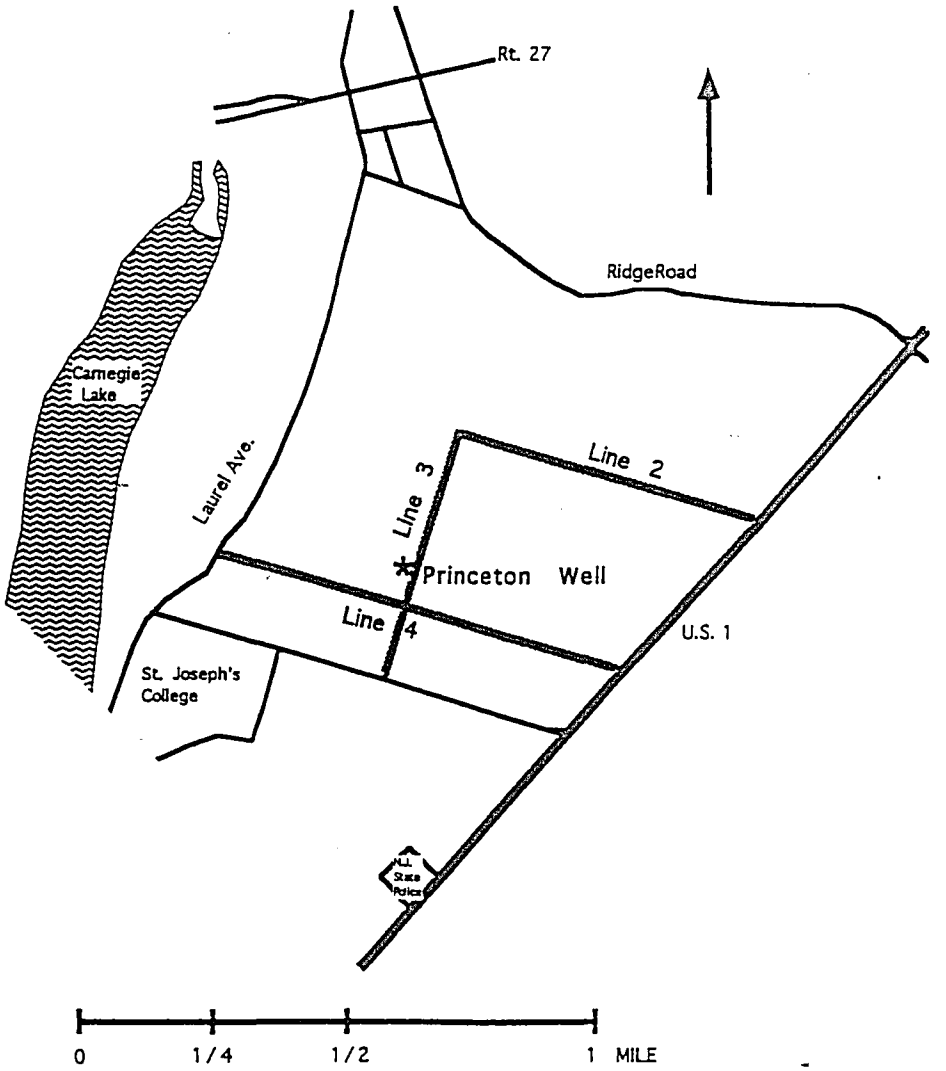

FIGURE 32: Site location map for the Princeton seismic lines and the Princeton core hole.

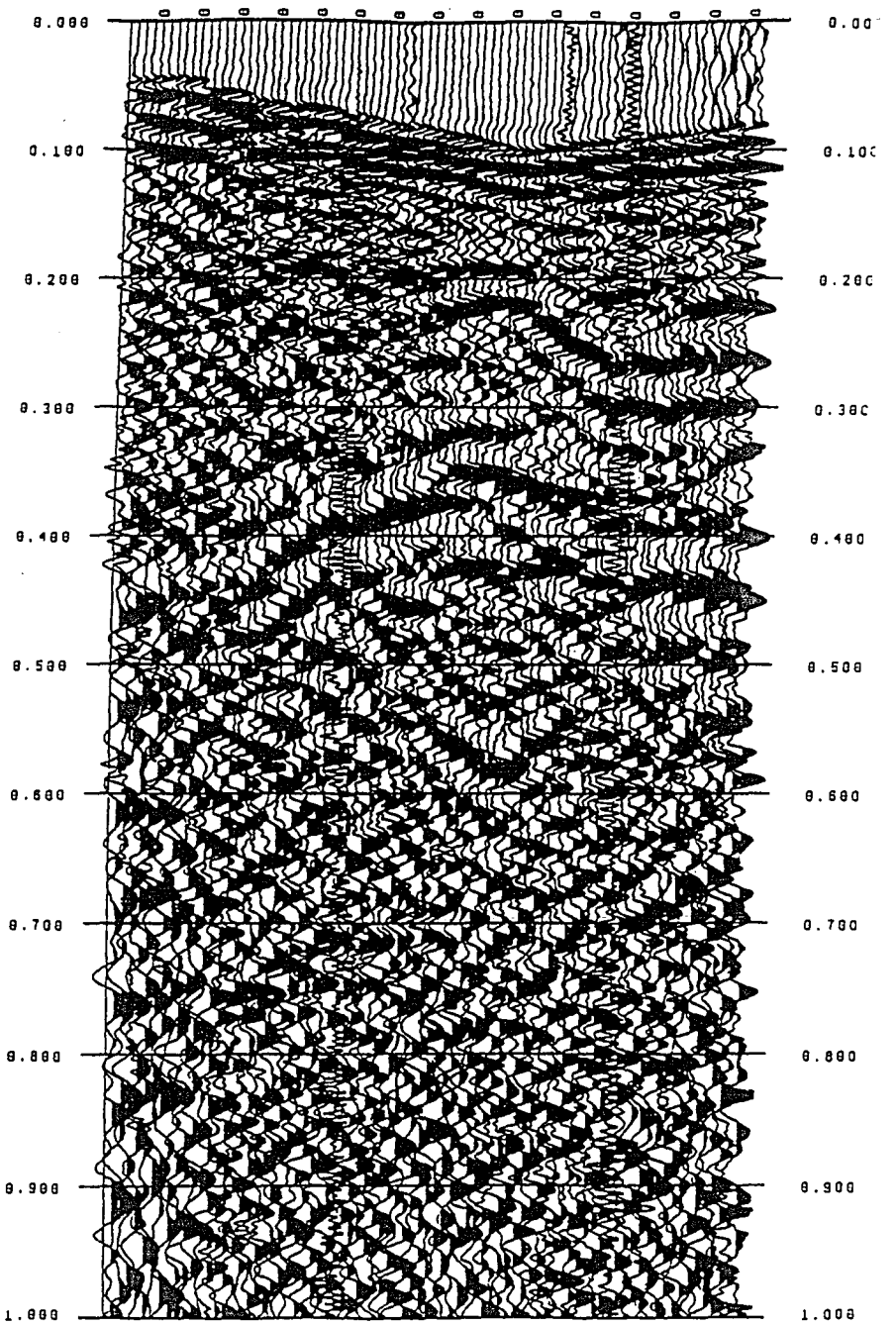

FIGURE 33: Near trace display, after field statics, of Princeton Line 2. Note higher S/N ratio than Washington's crossing Lines and prominant residual statics effect. Plotted with BP filter (5,10,160,240) and AGC (0.13 sec window).

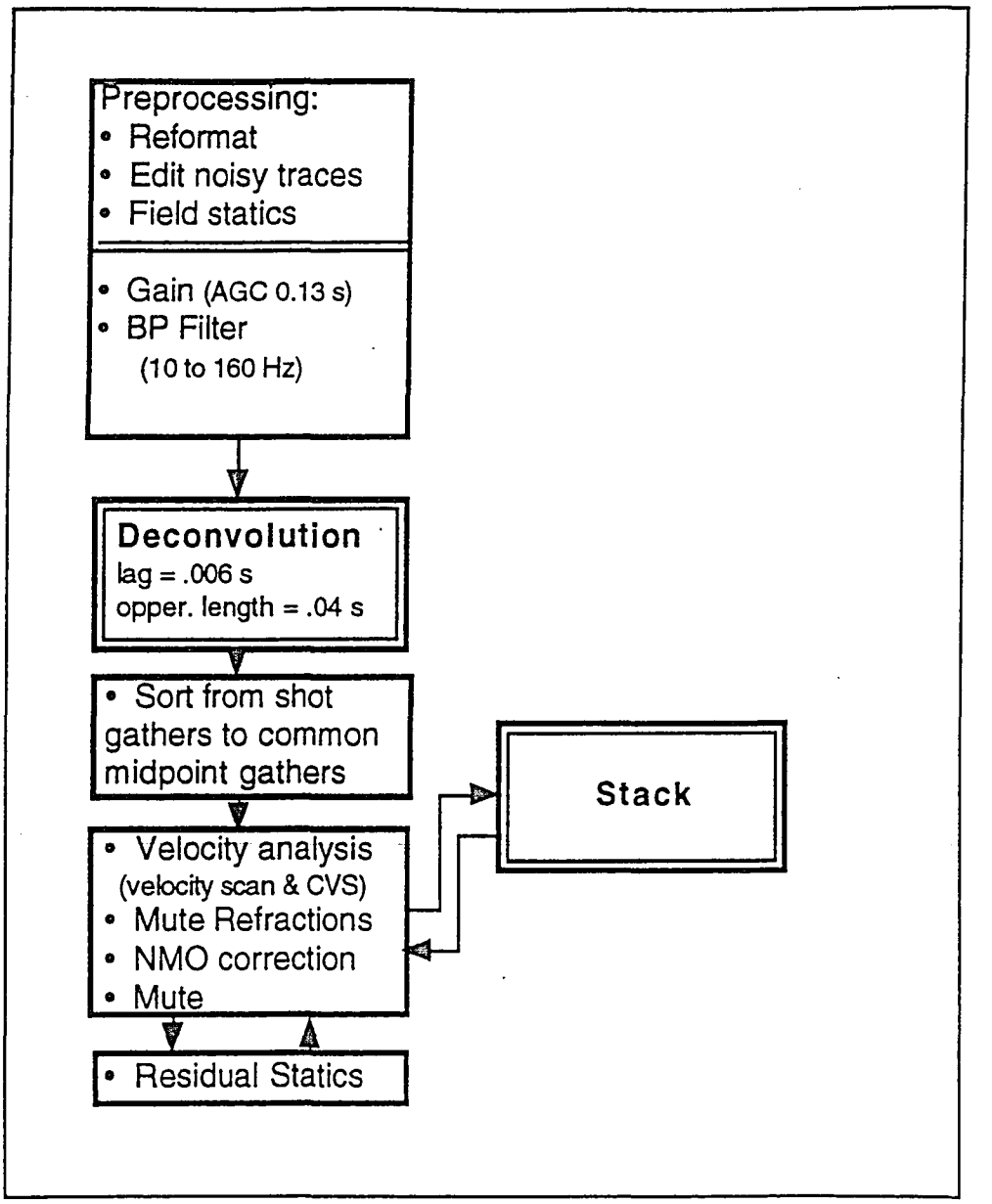

FIGURE 15: Processing scheme for Princeton Lines 2, 3 & 4.

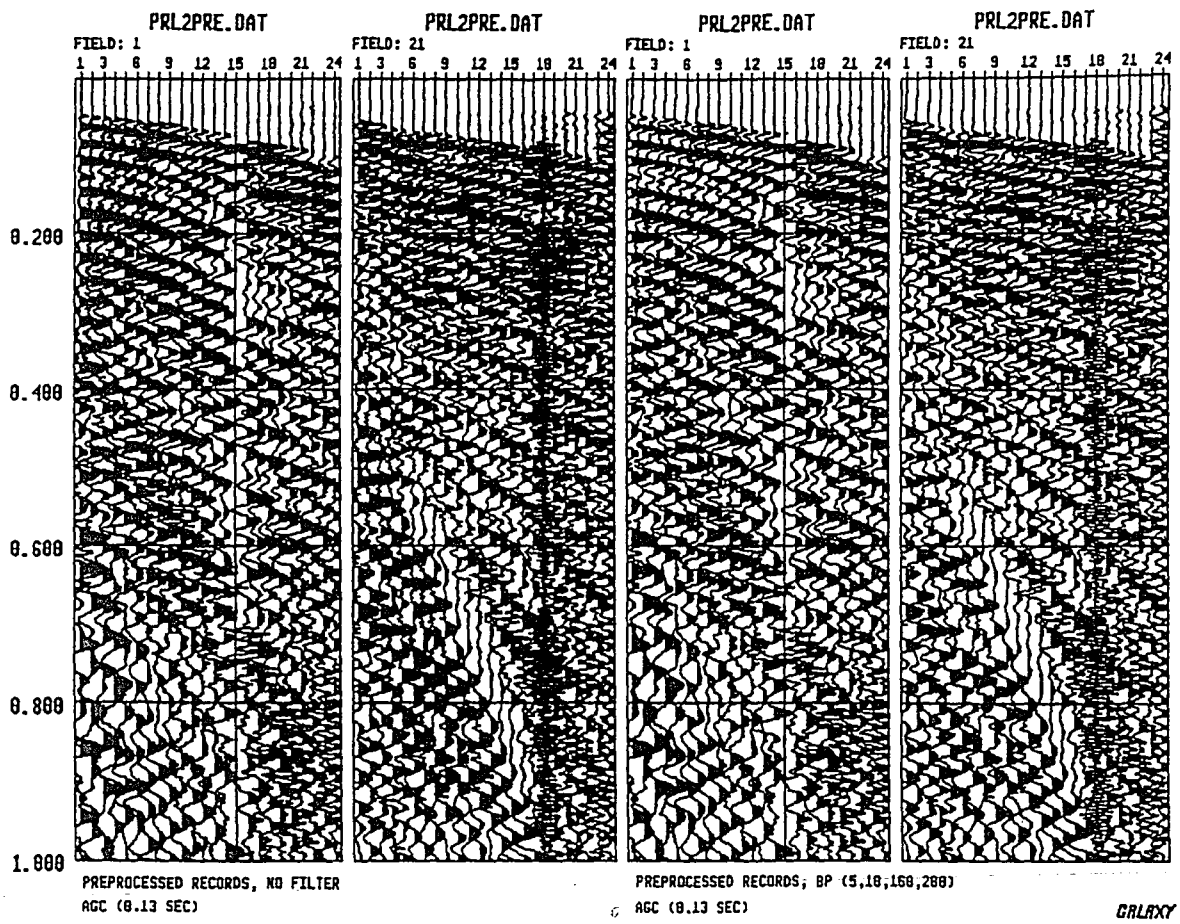

FIGURE 35: Comparison of PRL2 records 1 and 21 before and after editing, field statics, and electronic noise muting. Displayed with band-pass filter (5,10,160 200) and AGC (0.13 second window).

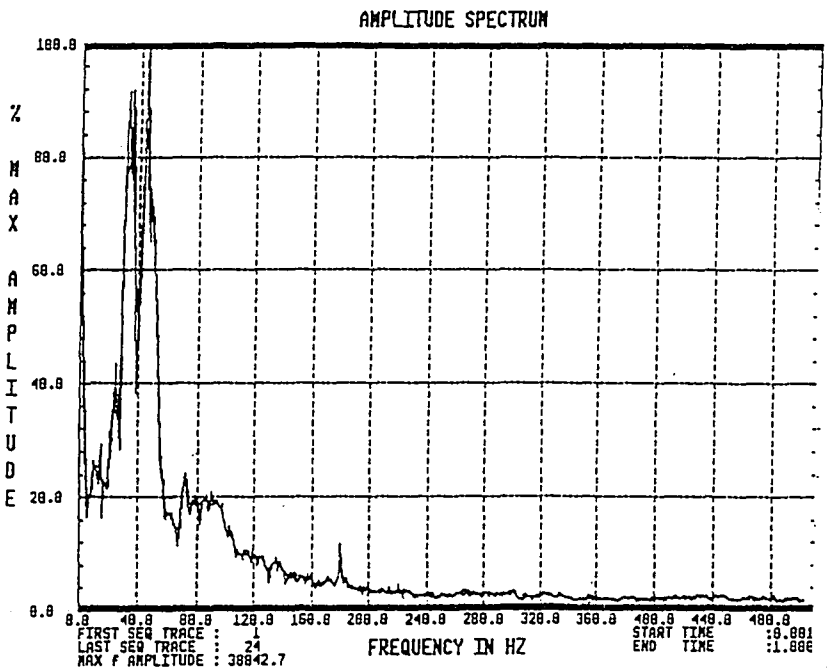

FIGURE 36: An amplitude spectra of field record 1 from Princeton Line 2. Frequencies up to 160 Hz contain signal above ambient noise level.

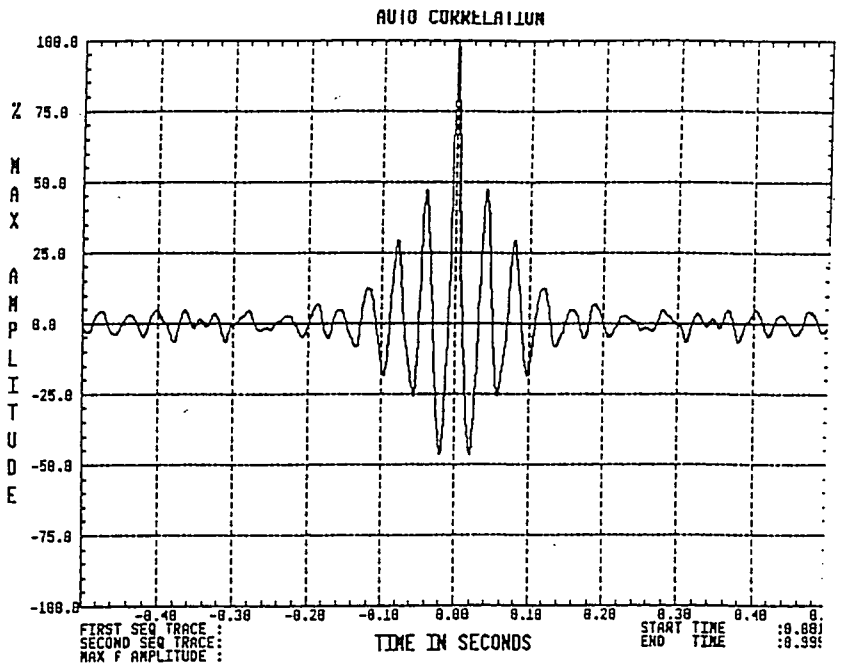

FIGURE 37: An autocorrelation plot from record 1 of PRL2. From time zero, the second zero crossing is used as the first estimation of the deconvolution opperator length.

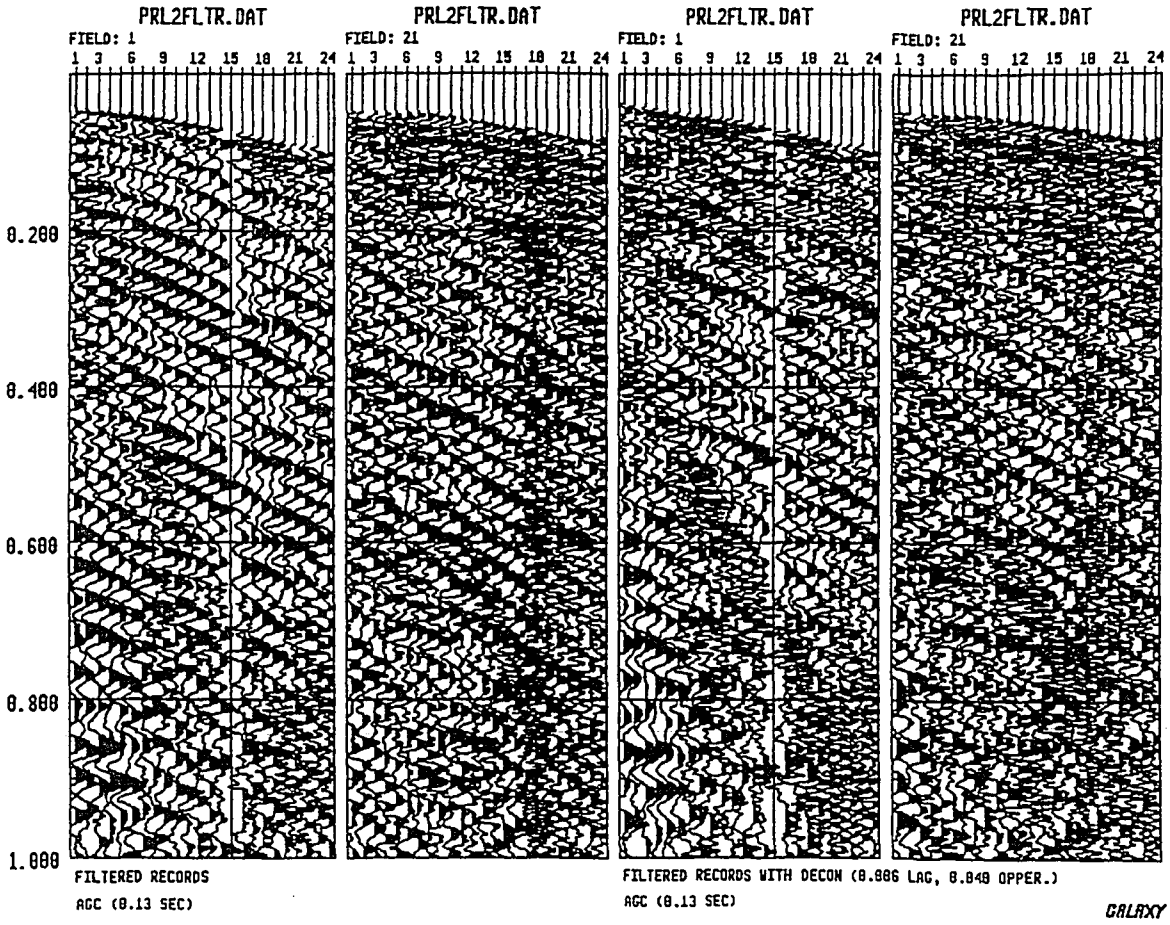

FIGURE 38: Plots from PRL2 before and after deconvolution with a lag of 0.006 seconds and an opperator length of 0.04 seconds. The analysis window for the deconvolution was chosen at every tenth record along the line, and is the area between the heavy lines. Note the reduction of refraction multiples and lack of reflection hyperbolas. Plotted with AGC (0.13 sec window).

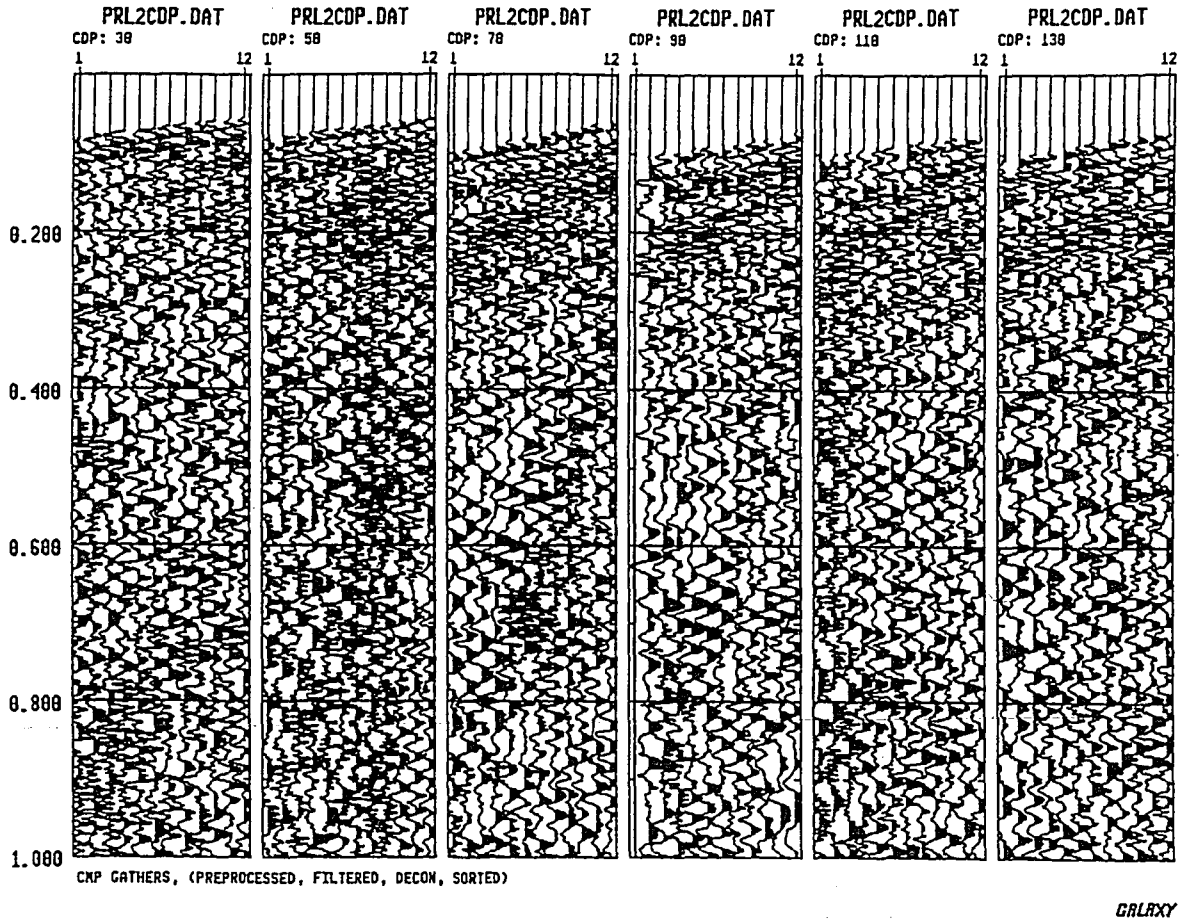

FIGURE 39: Records of PRL2 sorted to common midpoint gathers after deconvolution. Note the refractions which still dominate the upper 0.1 seconds of the gather. Plotted with AGC (0.13 sec window).

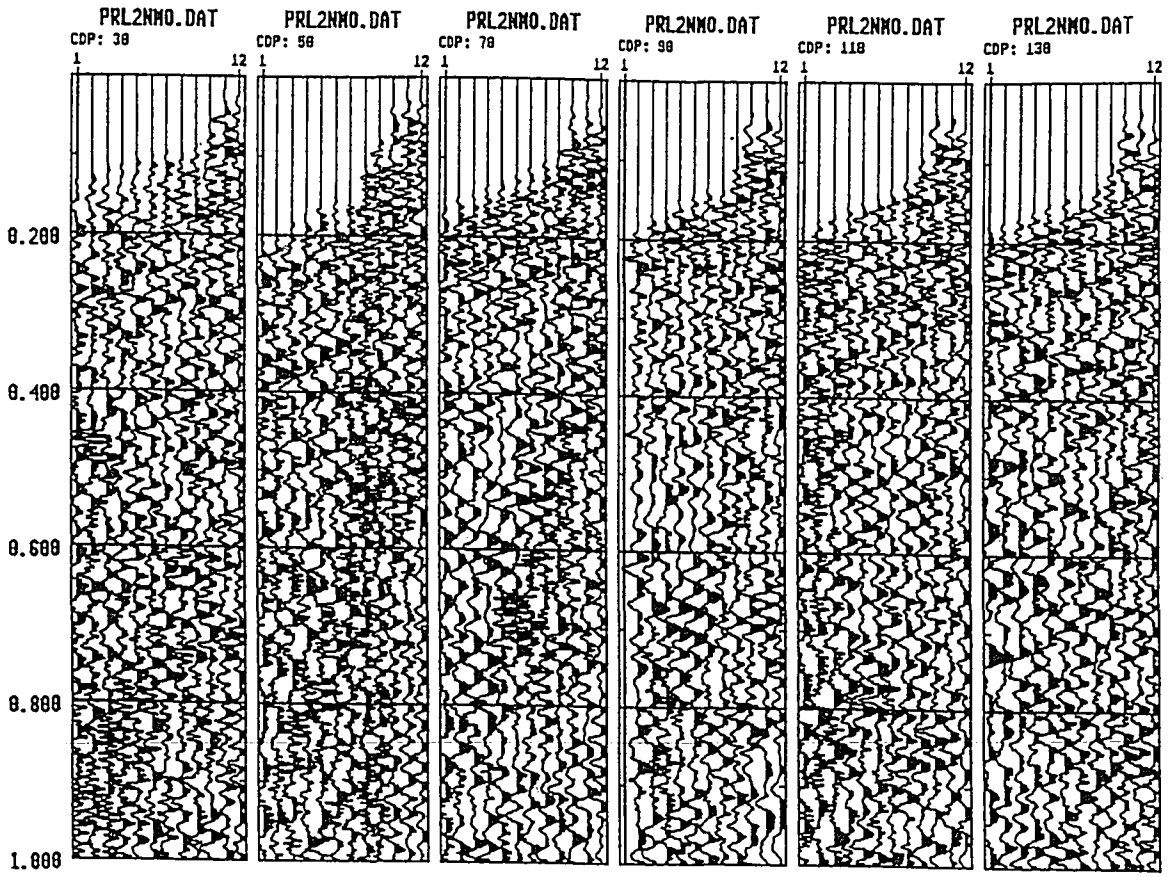

FIGURE 40: PRL2 after common midpoint sorting, deconvolution, and a mute to remove refracted arrivals. The mute is necessary in order to prevent stacking in refracted signal in velocity analyses. Plotted with AGC (0.13 sec window).

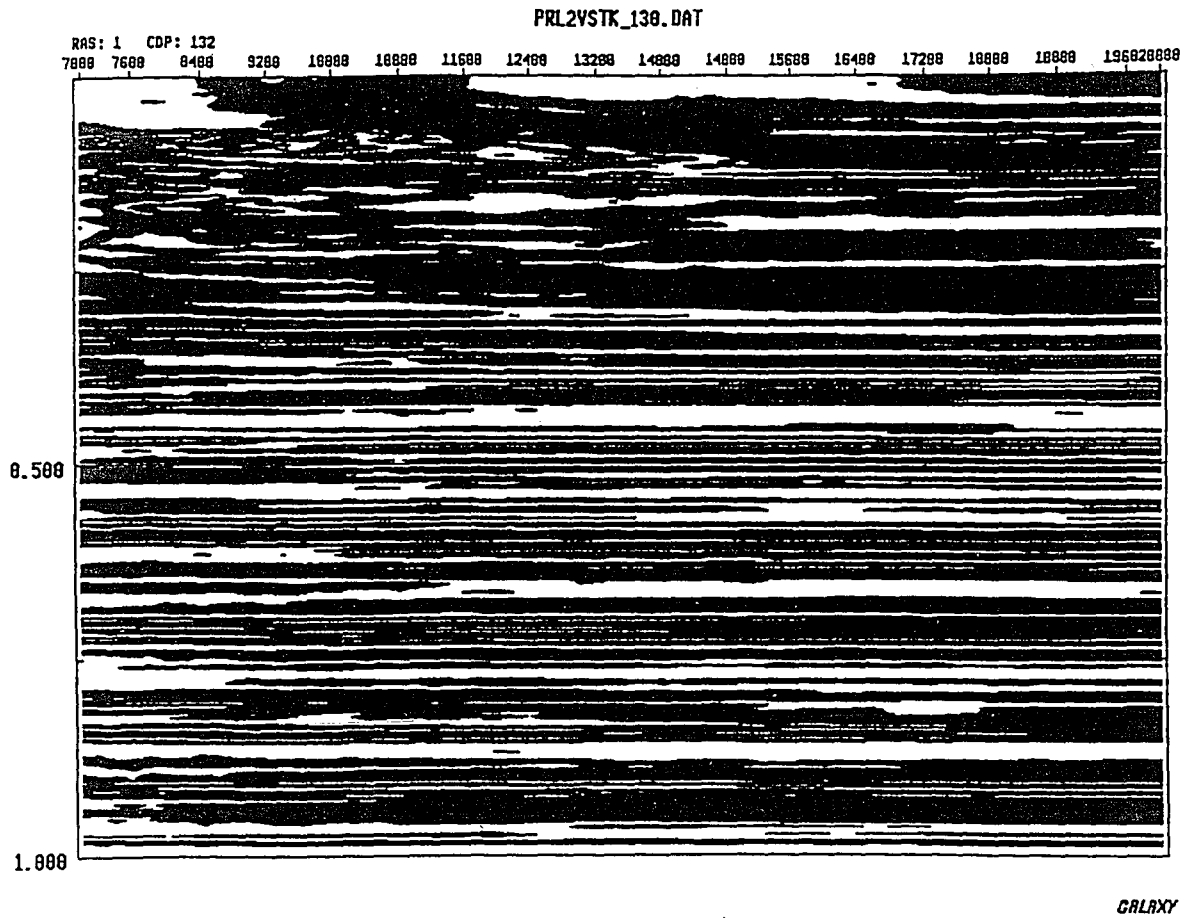

FIGURE 41: Velocity scan for PRL2 for common midpoint gather 132. The smearing of the high-semblance dark contours show the lack of good stacking velocities for reflection hyperbolas.

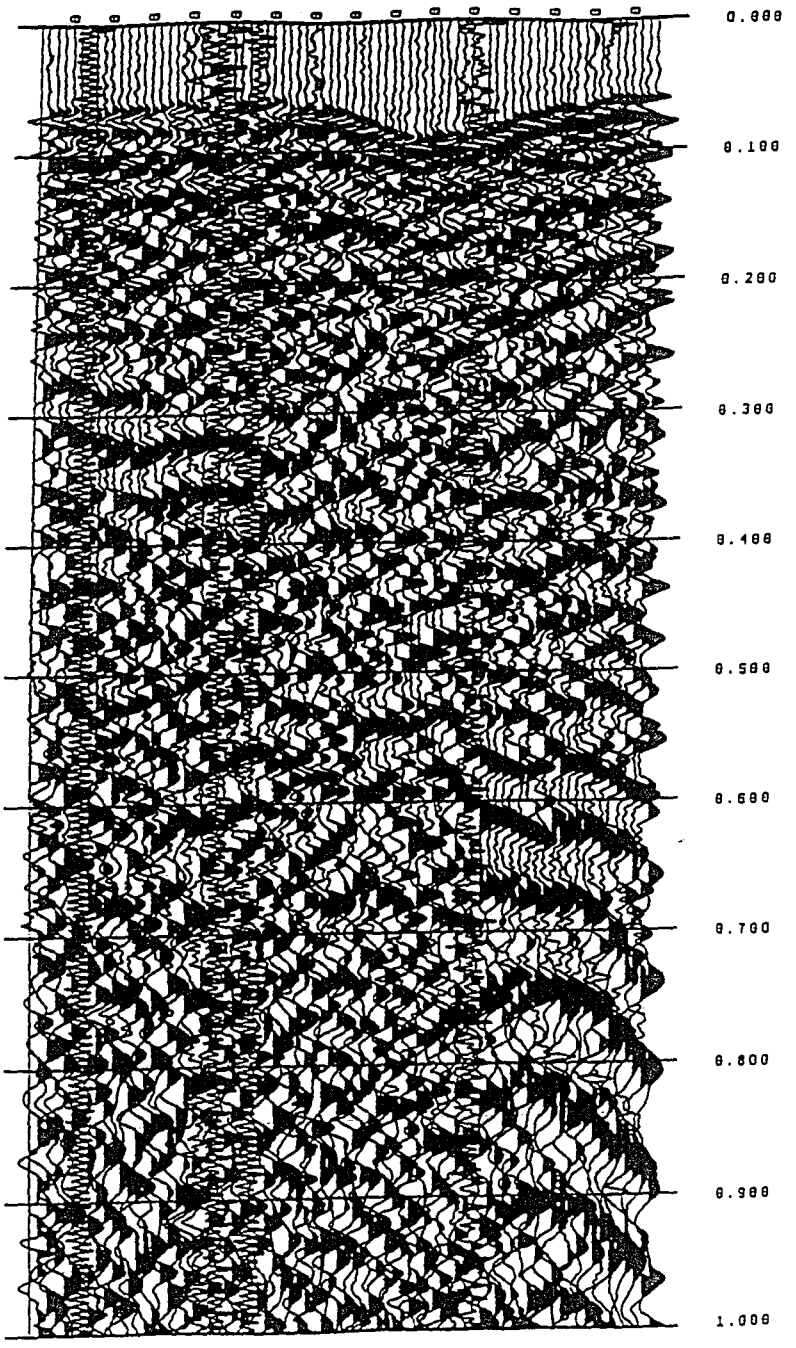

FIGURE 42: Near trace display of Princton Line 3. Note the similarities between this plot and PRL2 (**Figure 33**). Plotted with BP filter (5,10,160,240) and AGC (0.13 sec window).

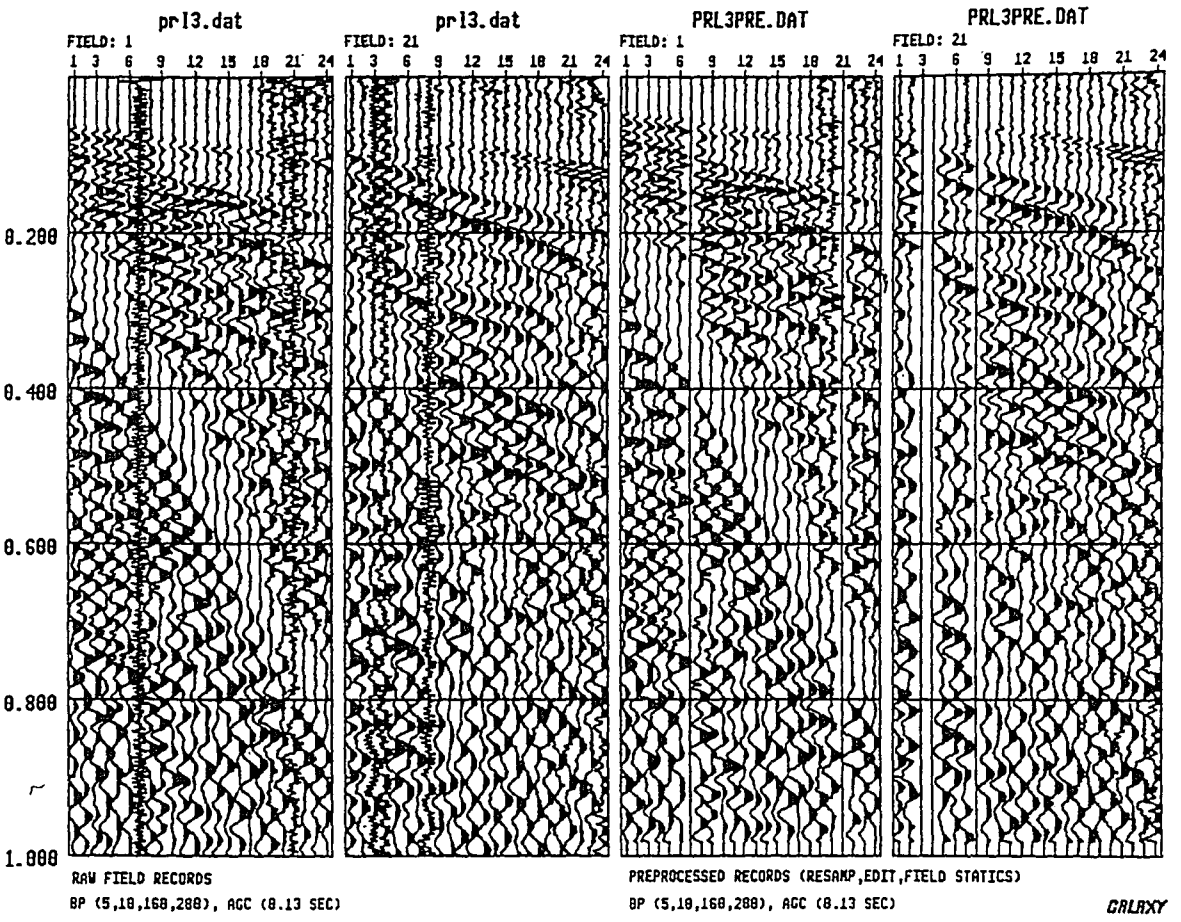

FIGURE 43: Comparison of PRL3 records 1 and 21 before and after editing, field statics, and electronic noise muting. Displayed with band-pass filter (5,10,160,200) and AGC (0.13 second window).

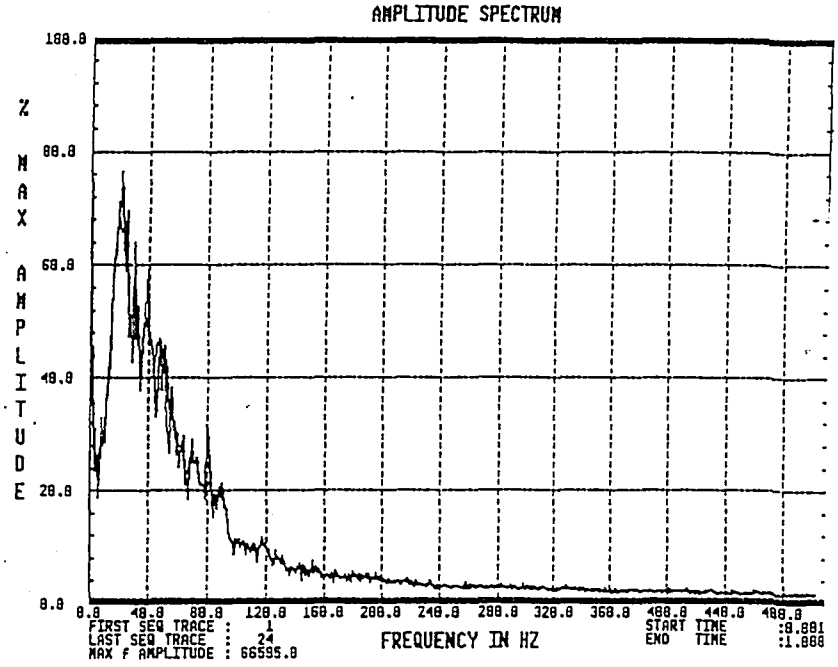

FIGURE 44: An amplitude spectra of field record 21 from Princeton Line 3. Frequencies up to 140 Hz contain signal above ambient noise level.

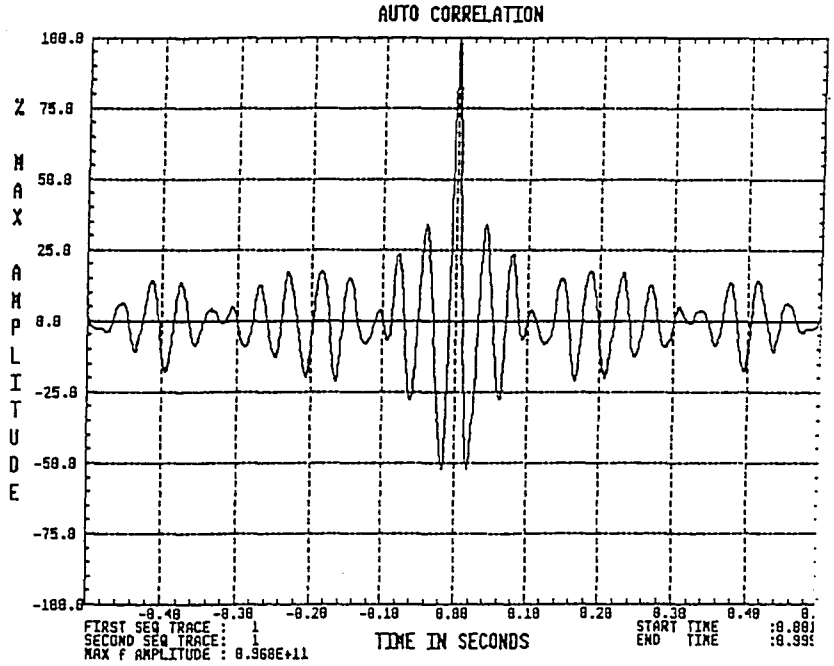

FIGURE 45: An autocorrelation plot from record 21 of PRL3. From time zero; the second zero crossing is used as the first estimation of the deconvolution opperator length.

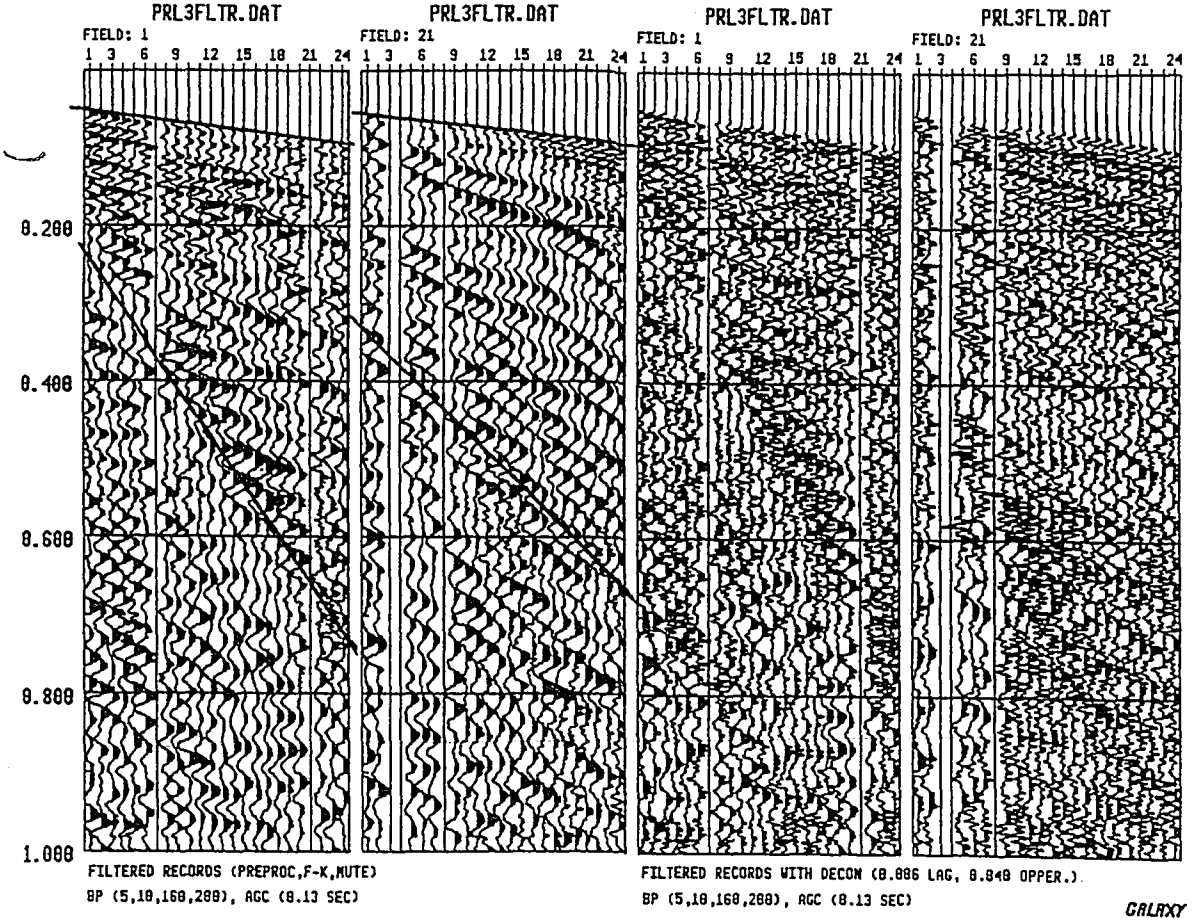

FIGURE 46: Plots from PRL3 before and after deconvolution with a lag of 0.006 seconds and an opperator length of 0.04 seconds. The analysis window for the deconvolution was chosen at every tenth record along the line, and is the area between the heavy lines. Note the reduction of refraction multiples and lack of reflection hyperbolas. Plotted with AGC (0.13 sec window).

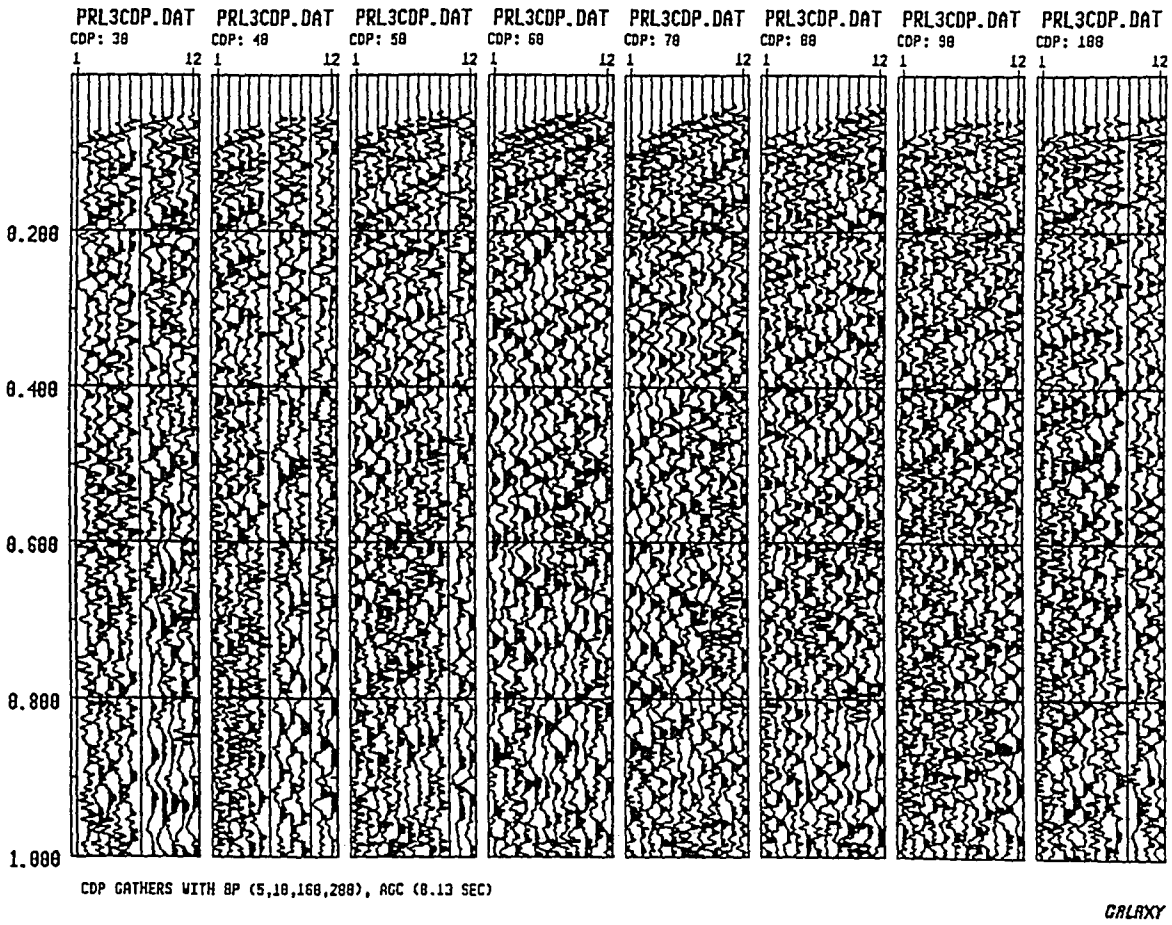

FIGURE 47: Records of PRL3 sorted to common midpoint gathers after deconvolution. Note the refractions which still dominate the upper 0.1 seconds of the gather. Plotted with AGC (0.13 sec window).

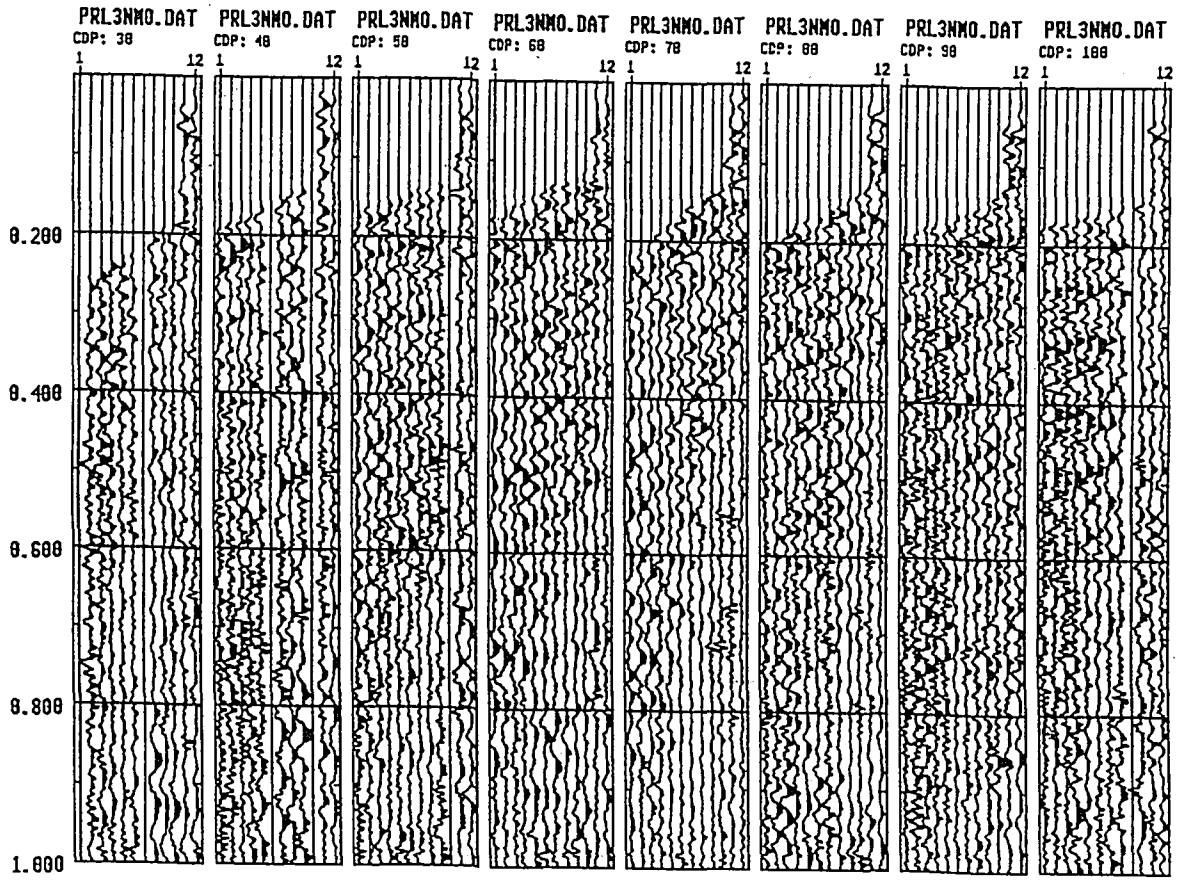

FIGURE 48: PRL3 after common midpoint sorting, deconvolution, and a mute to remove refracted arrivals. The mute is necessary in order to prevent stacking in refracted signal in velocity analyses. Plotted with AGC (0.13 sec window).

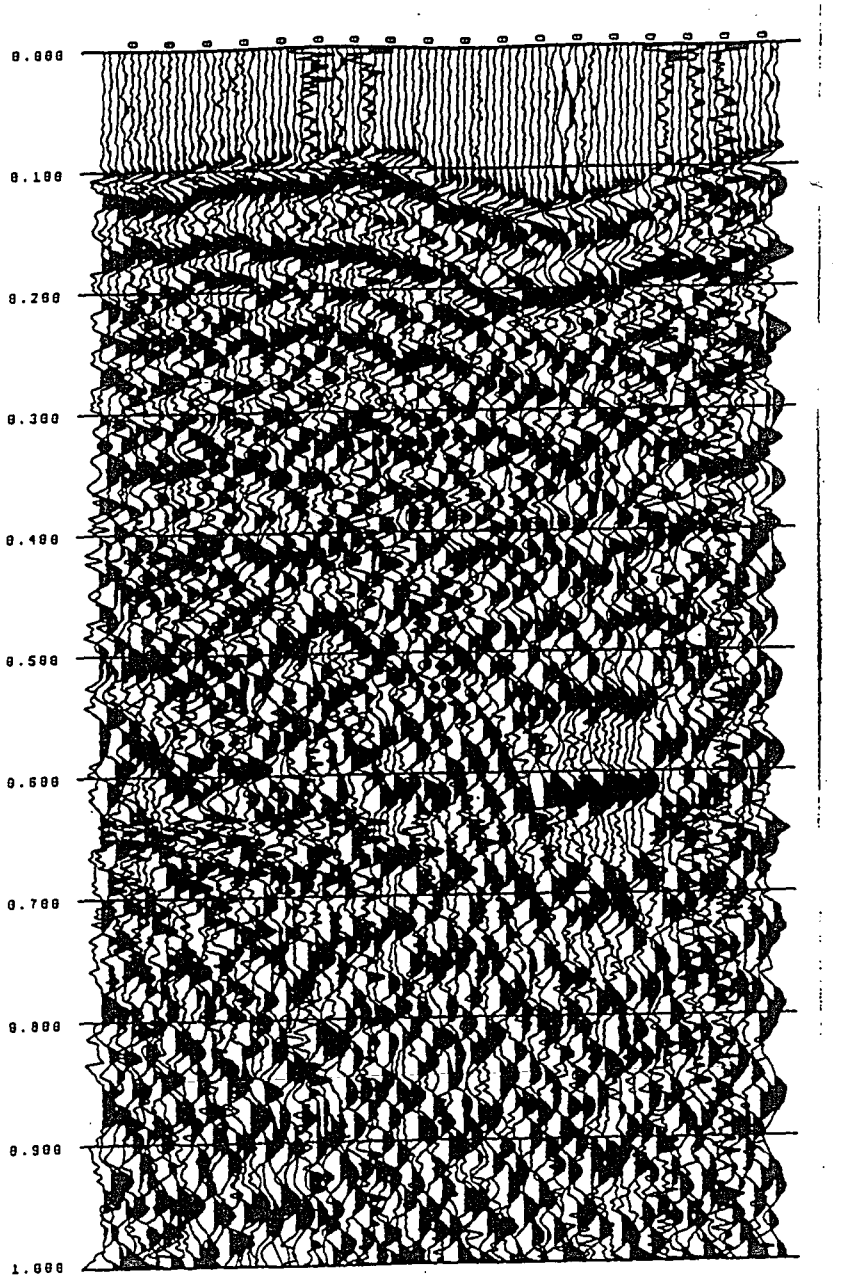

FIGURE 49: Near trace display of Princton Line 4. Note the similarities between this plot and PRL2 (**Figure 33**). Plotted with BP filter (5,10,160,240) and AGC (0.13 sec window).

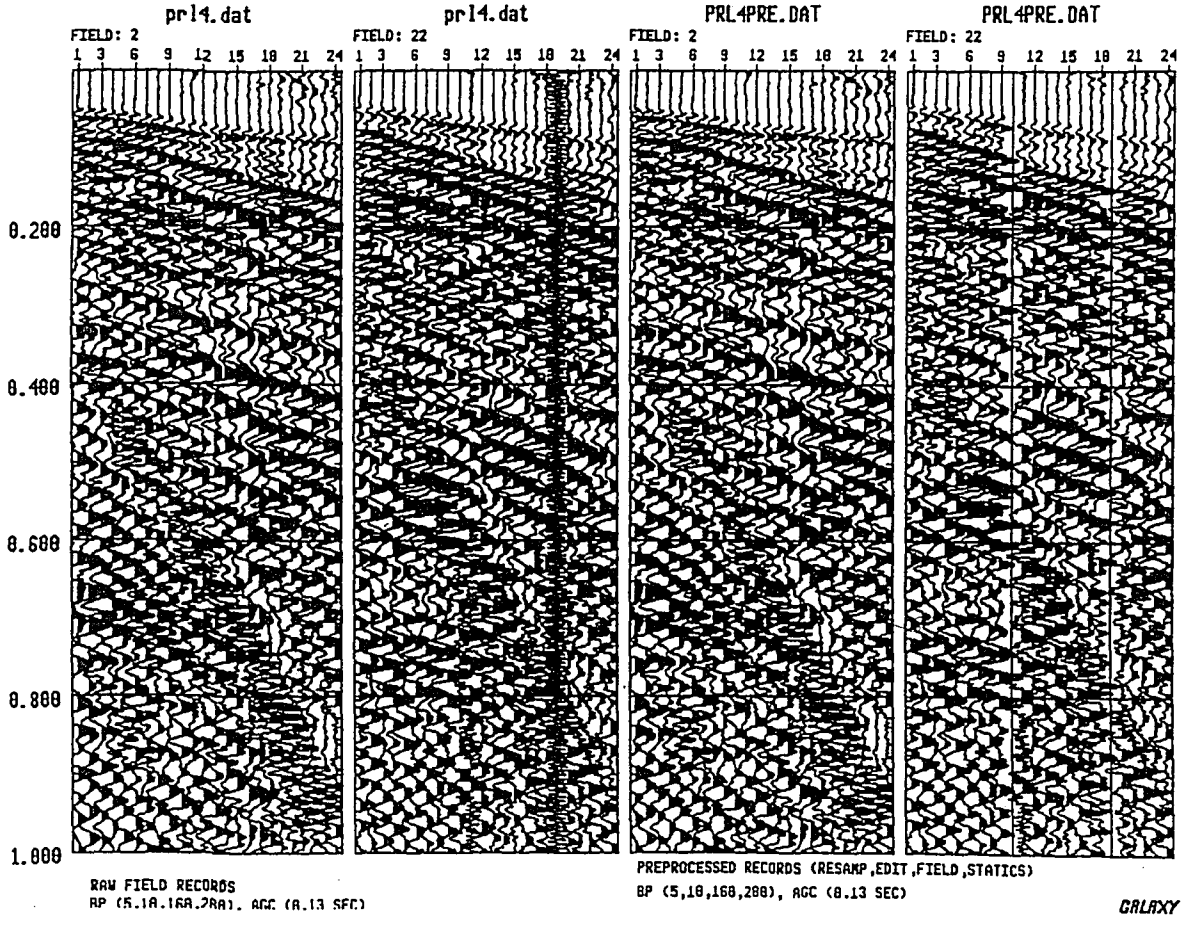

FIGURE 50: Comparison of PRL4 records 2 and 22 before and after editing, field statics, and electronic noise muting. Displayed with band-pass filter (5,10,160,200) and AGC (0.13 second window).

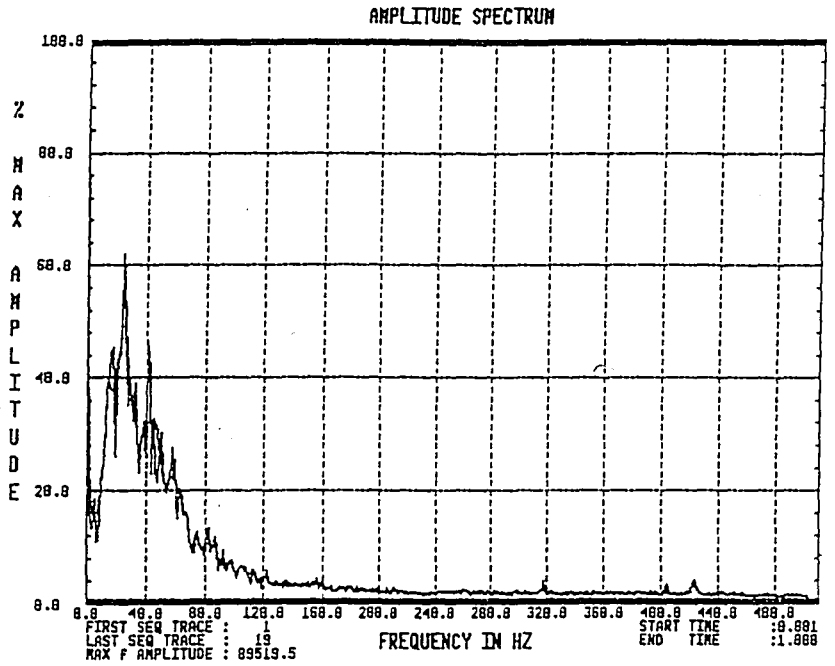

FIGURE 51: An amplitude spectra of field record 22 from Princeton Line 4. Frequencies up to 120 Hz contain signal above ambient noise level.

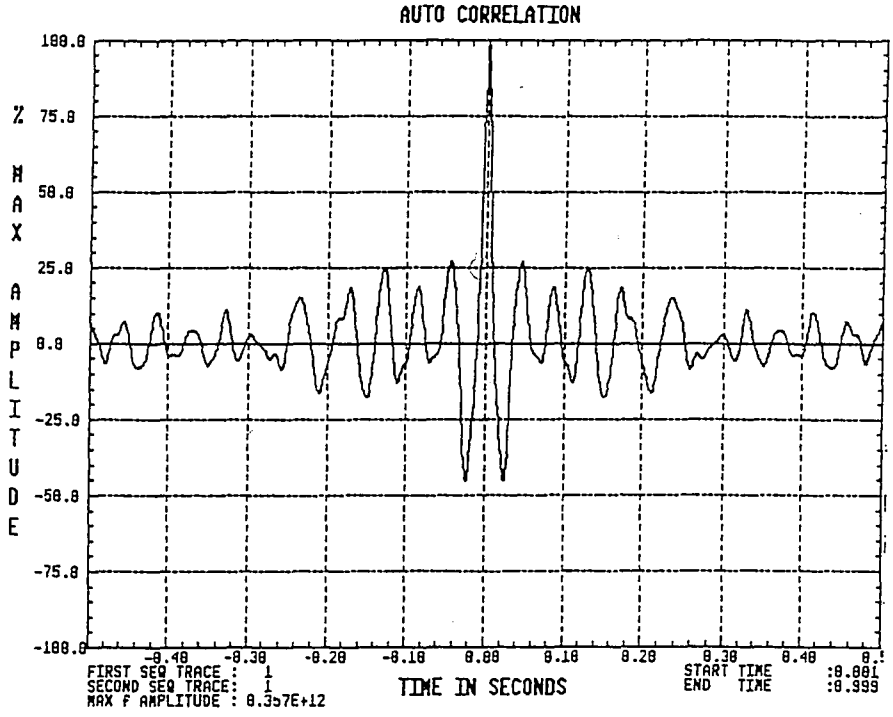

FIGURE 52: An autocorrelation plot from record 52 of PRL4. From time zero, the second zero crossing is used as the first estimation of the deconvolution opperator length.

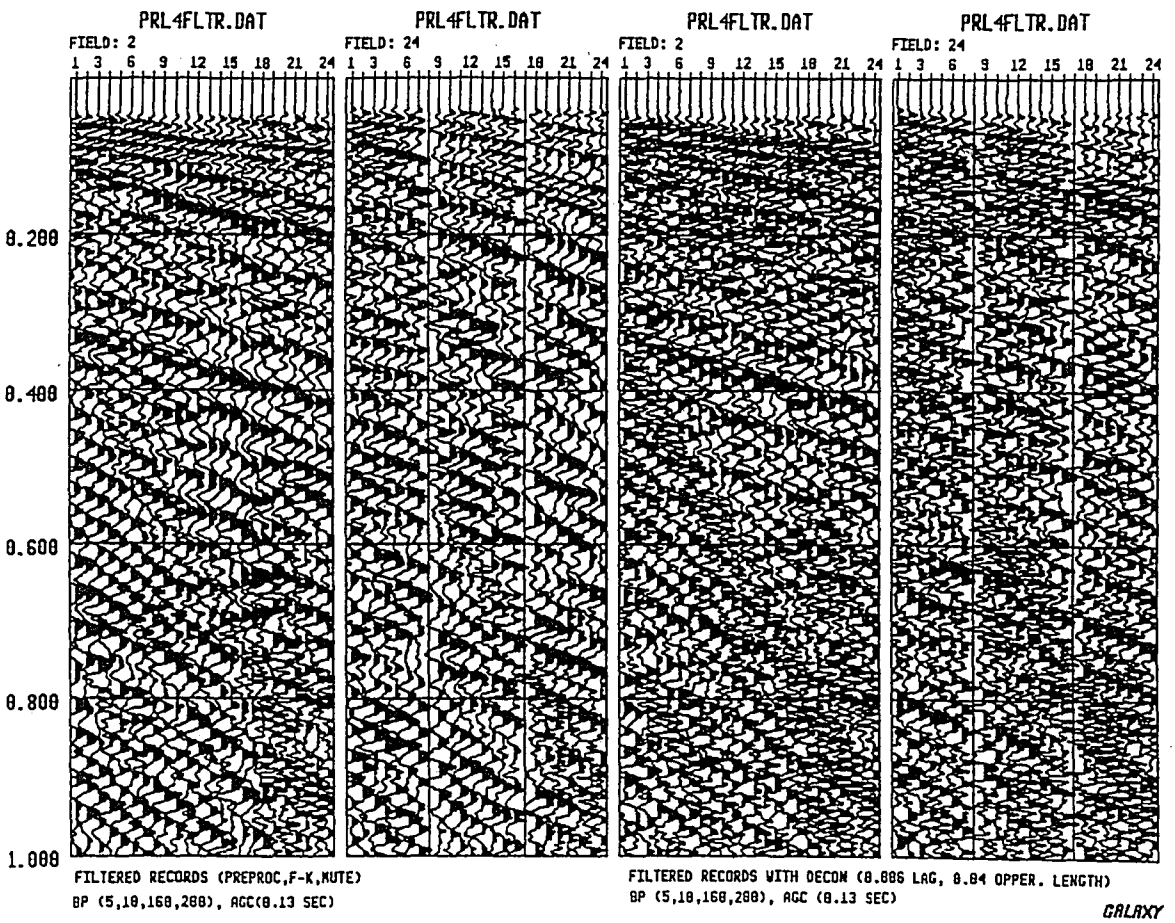

FIGURE 53: Plots from PRL4 before and after deconvolution with a lag of 0.006 seconds and an opperator length of 0.04 seconds. The analysis window for the deconvolution was chosen at every tenth record along the line, and is the area between the heavy lines. Note the reduction of refraction multiples and lack of reflection hyperbolas. Plotted with AGC (p.13 sec window).

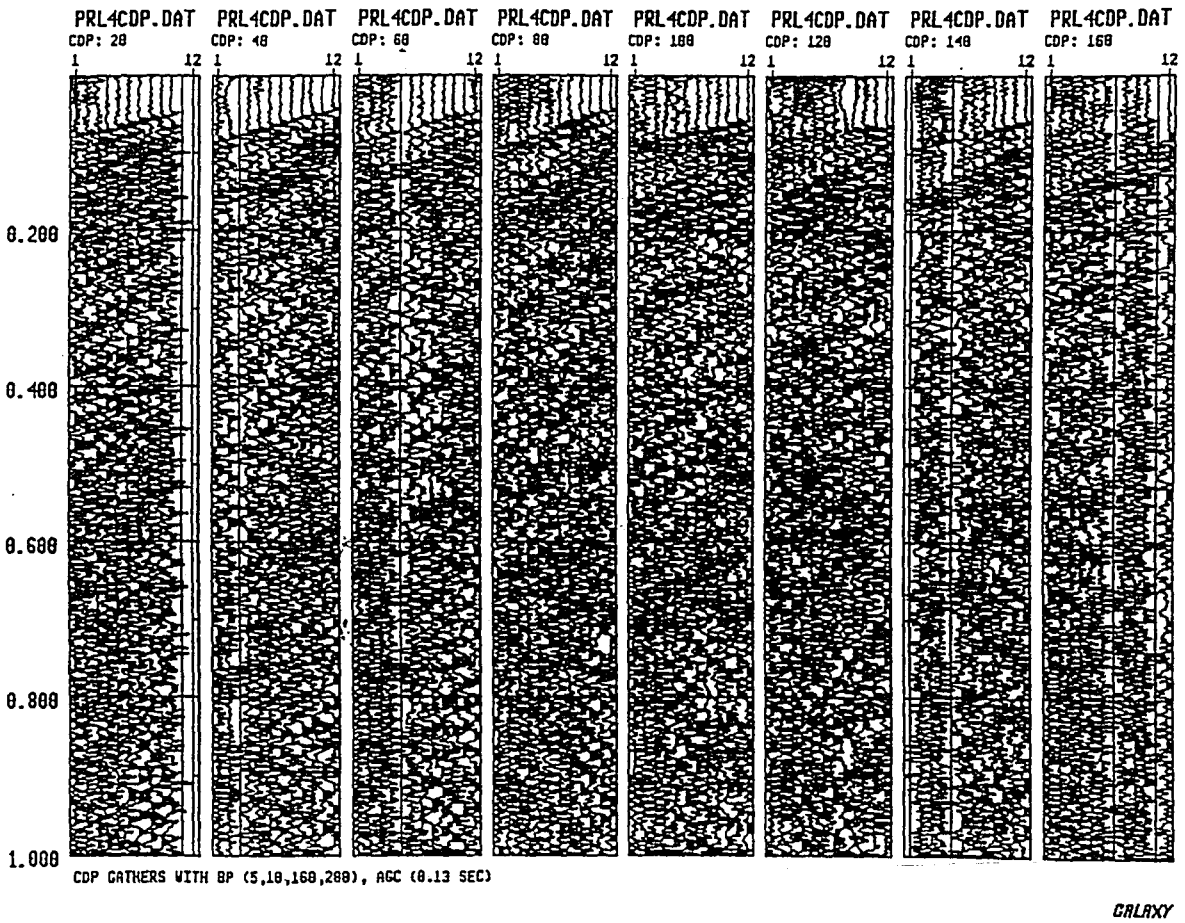

FIGURE 54: Records of PRL4 sorted to common midpoint gathers after deconvolution. Note the refractions which still dominate the upper 0.1 seconds of the gather. Plotted with AGC (0.13 sec window).

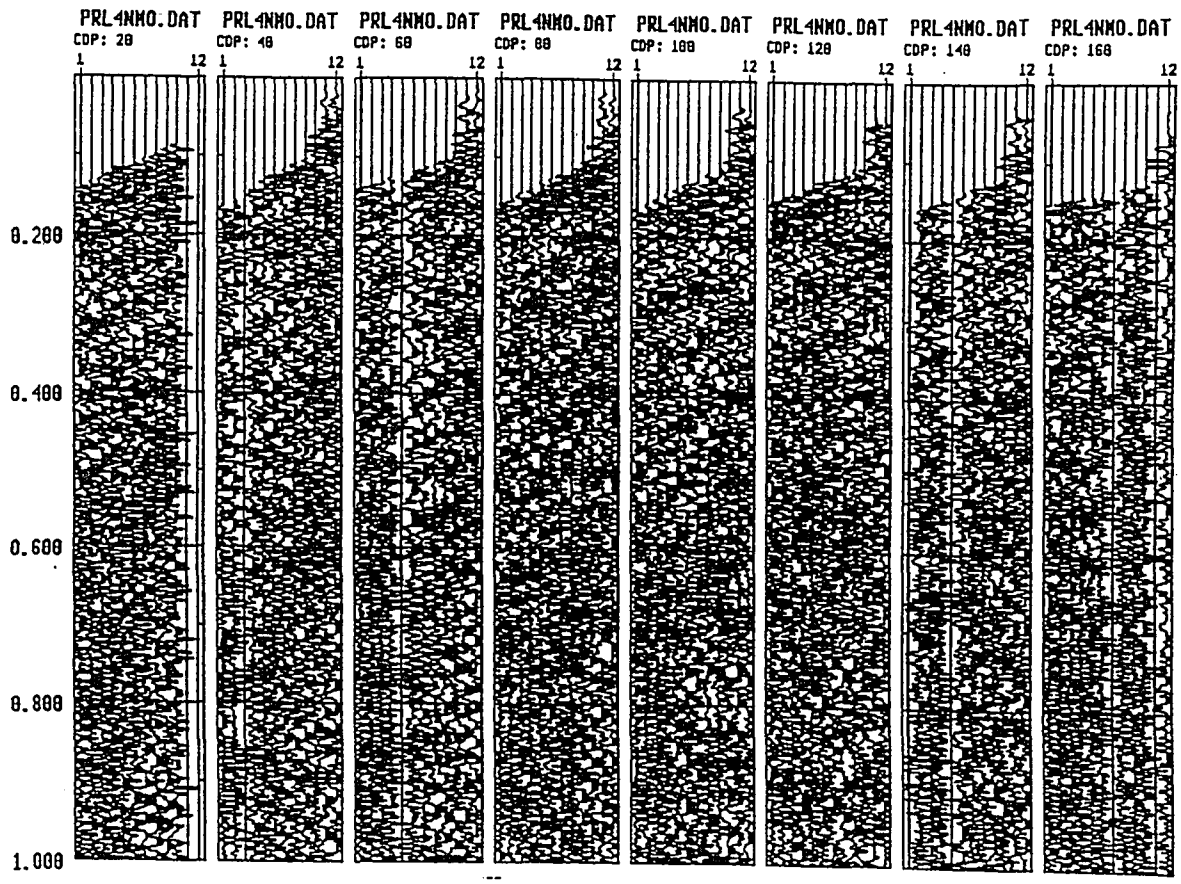

FIGURE 55: PRL4 after common midpoint sorting, deconvolution, and a mute to remove refracted arrivals. The mute is necessary in order to prevent stacking in refracted signal in velocity analyses. Plotted with AGC (0.13 sec window).

FIGURE 56: The top schematic shows a sample ray path traveling through different thicknesses of a low velocity layer. (a) shows a common midpoint gather with a normal moveout velocity correctly applied. However, the static time shifts caused by the varying low velocity layer cause a degraded stacked trace (b). By correcting for a varying near surface layer, a correct common midpoint gather with the same normal moveout velocity applied produces a distinct reflector (c).

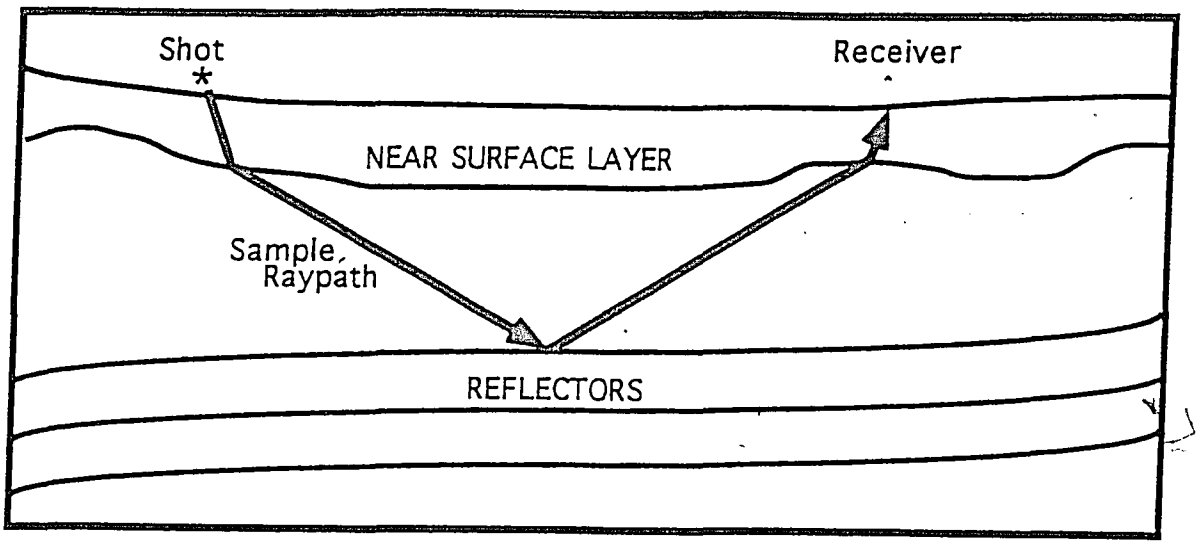
Shot
Receiver
NEAR SURFACE LAYER
Sample
Raypath
REFLECTORS

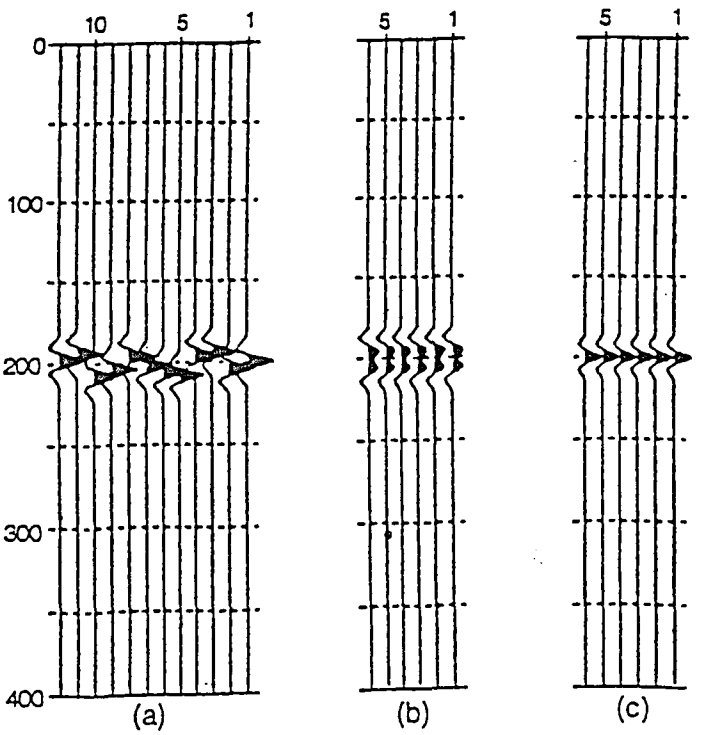
10
5
1
0
100
200
300
400
(a)
5
1
(b)
5
1
(c)

Schematic Cross-Section
Princeton Line 2 Near Surface

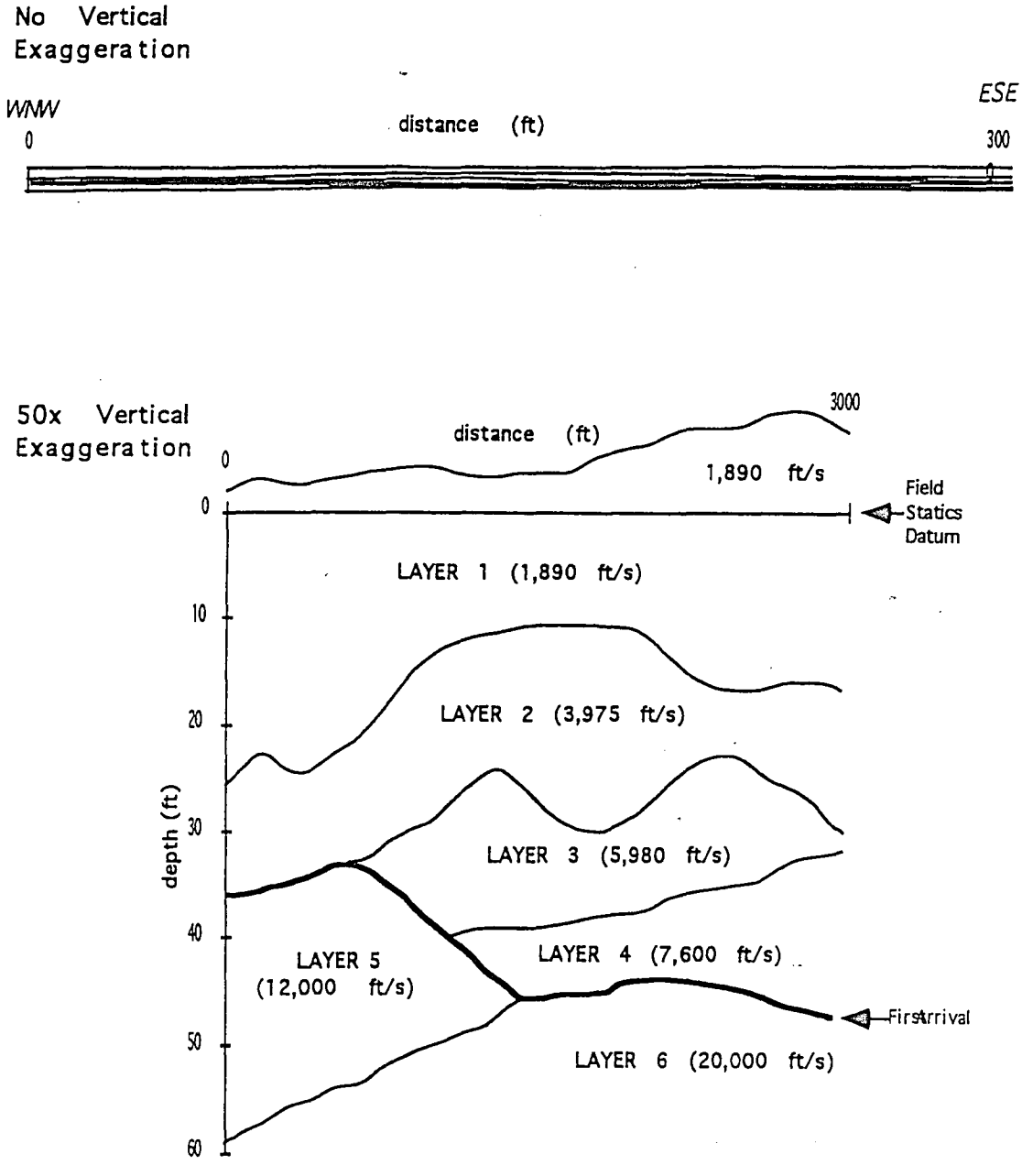

FIGURE 57: Interpretation of the complex near-surface of Princeton Line 2. The velocities for the layers are calculated as described in the text.

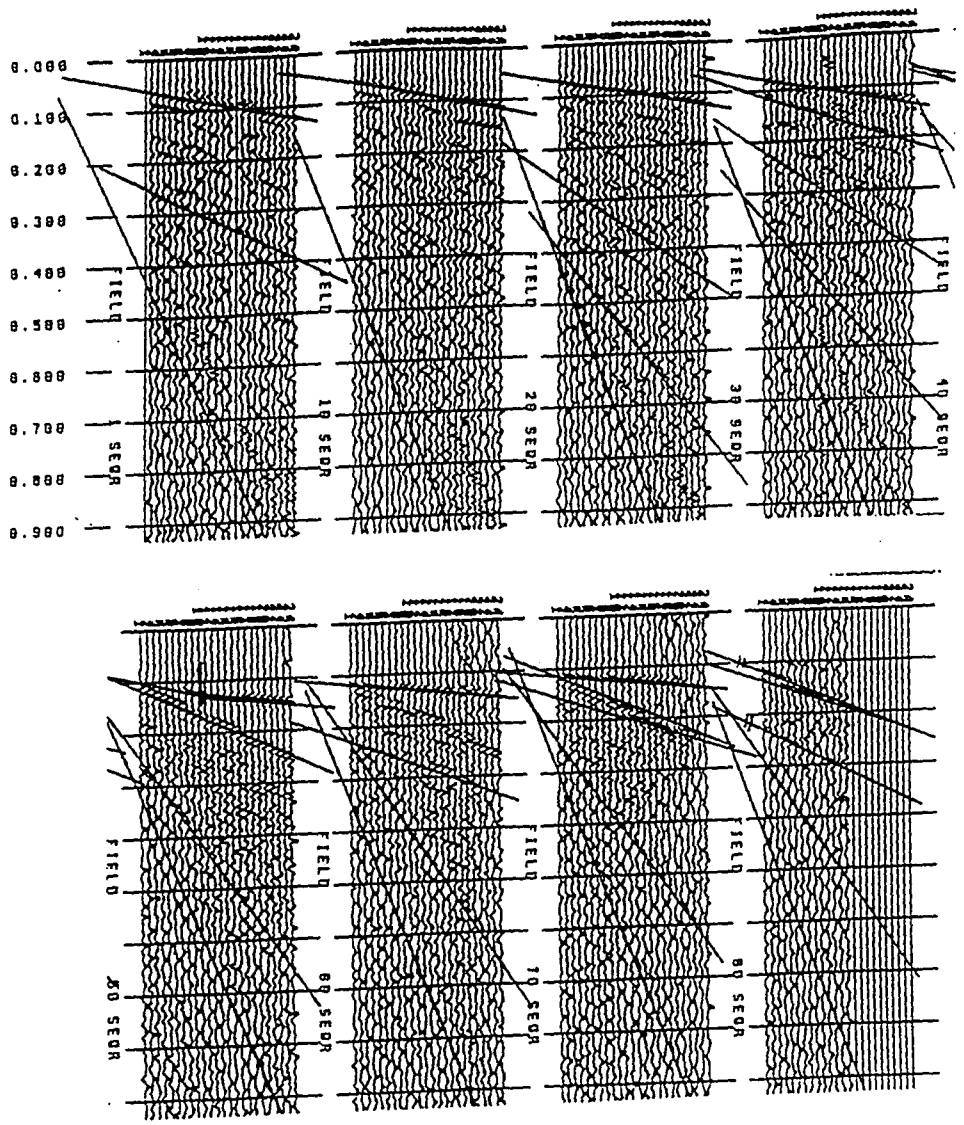

FIGURE 58: A graphical illustration of the location of the refraction picks used to calculate the various near surface velocities. **Table 4** tabulates the results of inverting the refraction slopes to get velocities. The field record number is shown along the side of the respective gather.

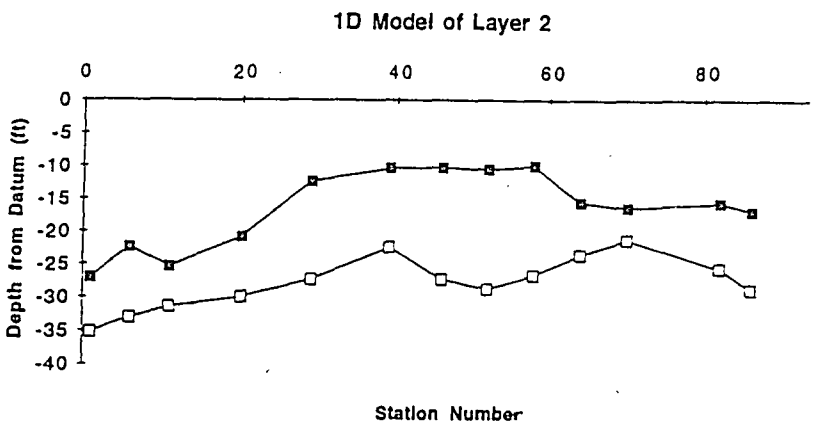

FIGURE 59: Plot of the 1D interface depth of Layer 1 and Layer 2 (see **Table 5**), showing the modeled depths and geometries of the interfaces. Depth to Layer 2 is calculated using Layer 5/6 velocities, thus the depth is the shallowest expected position of the interface.

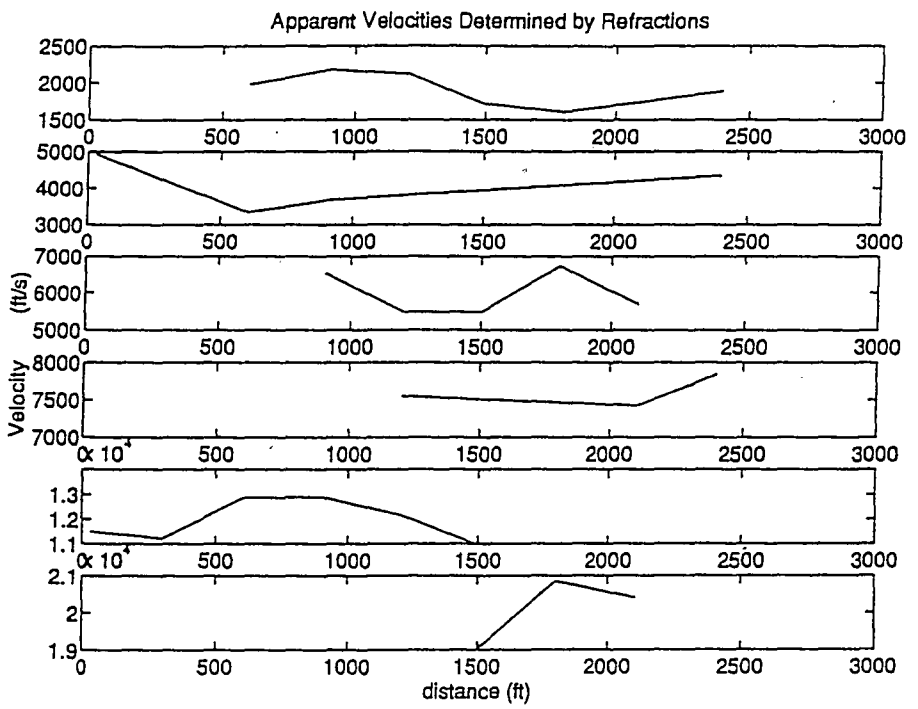

FIGURE 60: A plot of the apparent velocity picks for the six near surface layers seen in PRL2. The curves are plotted with layer 1 at the top and layer 6 at the bottom. With the assumption of constant velocity layers, an increase in apparent velocity suggests updip ray paths, or an upward sloping interface. Similarly, a decrease in apparent velocity suggests a downward spoling interface.

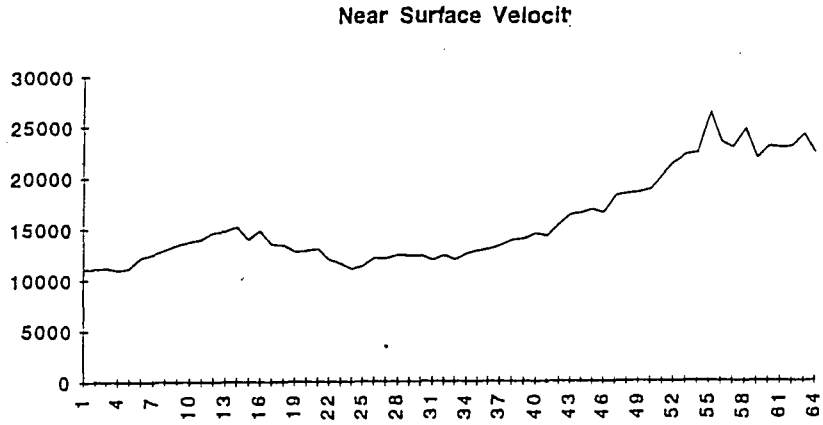

FIGURE 61: A plot of the near surface velocity calculated from linear-regressions at each station (see **Table 5**). Note the two trends in the velocity: the perturbation between stations 7 and 19 from an average velocity of 12,000 ft/s, and the smoothed increase to 20,000 ft/s at increasing station numbers. The vertical axis is in units of ft/sec, and the horizontal axis is station numbers.

FIGURE 62: A plot of the correlation cofficient from the regressions on the refraction picks of PRL2. The two locations of decreasing correlation (increased deviations of the picks from the regression line) correspond with the short offset perturbation between stations 4 and 16, and the sharp break in velocity from 12,000 ft/s the 20,000 ft/s at station 46, which is recorded in records 34 through 58.

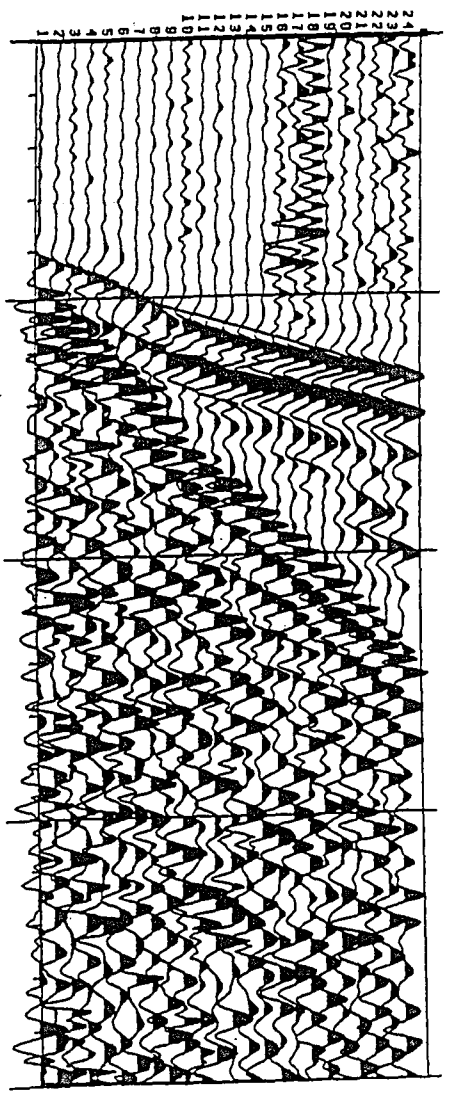

FIGURE 63: Comparison of the raytracing model of **Figure 69** for shot record 52, with travel times from raytracing model superimposed.

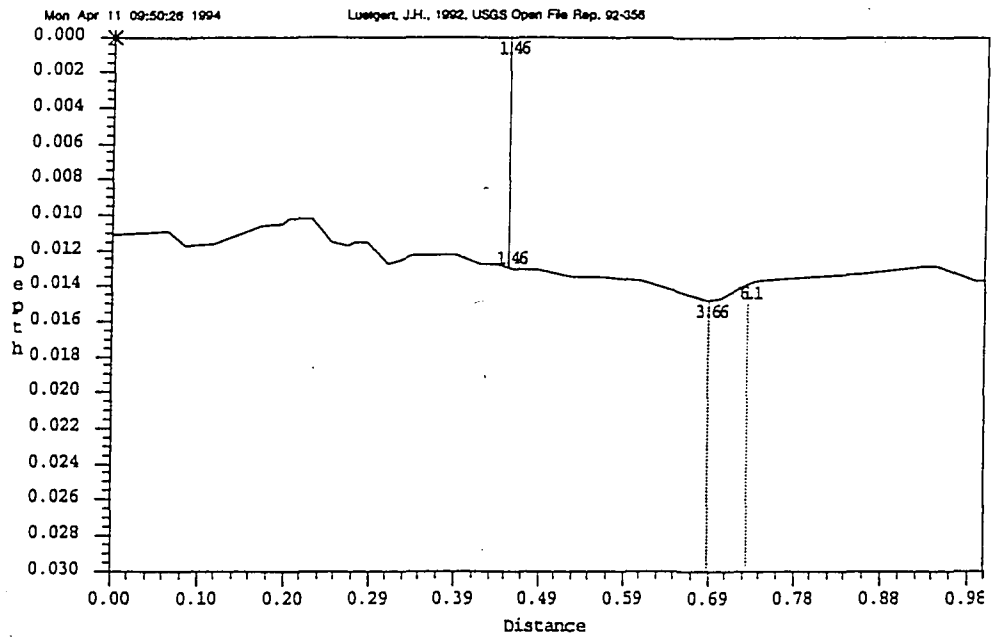

FIGURE 64: Final model of the Layer 5 and Layer 6 first break interface using the 2D raytracing program MacRay (Leutgert, 1992). Note the short offset undulations throughout the model, and the velocity break at offsets of 0.69 to 0.74 km from 12,000 ft/s (3.66 km/s) to 20,000 ft/s (6.1 km/s). Distance and depth are in kilometers.

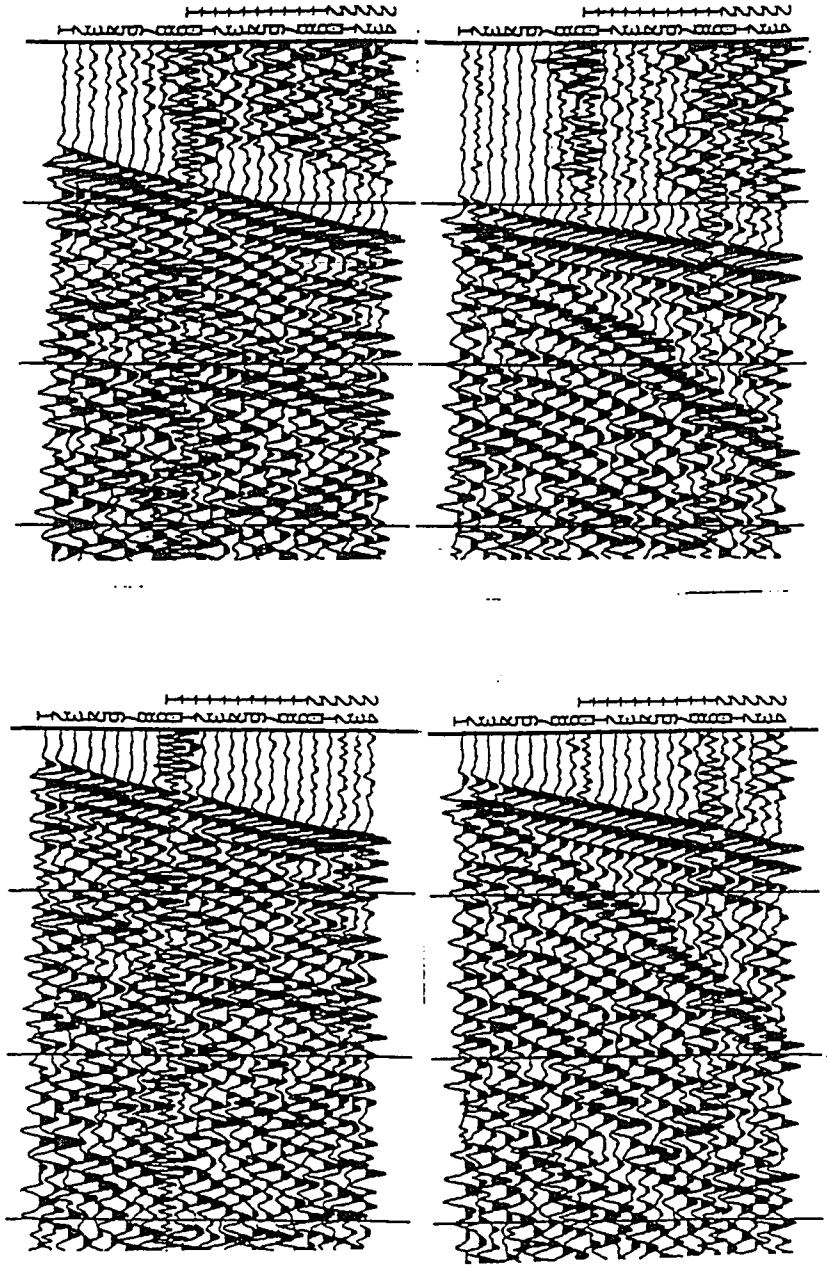

FIGURE 65: Princeton Line 2 records 20 and 60 before (top) and after (bottom) refraction statics corrections to adjust static time shifts. Plotted with AGC (0.13 sec window).

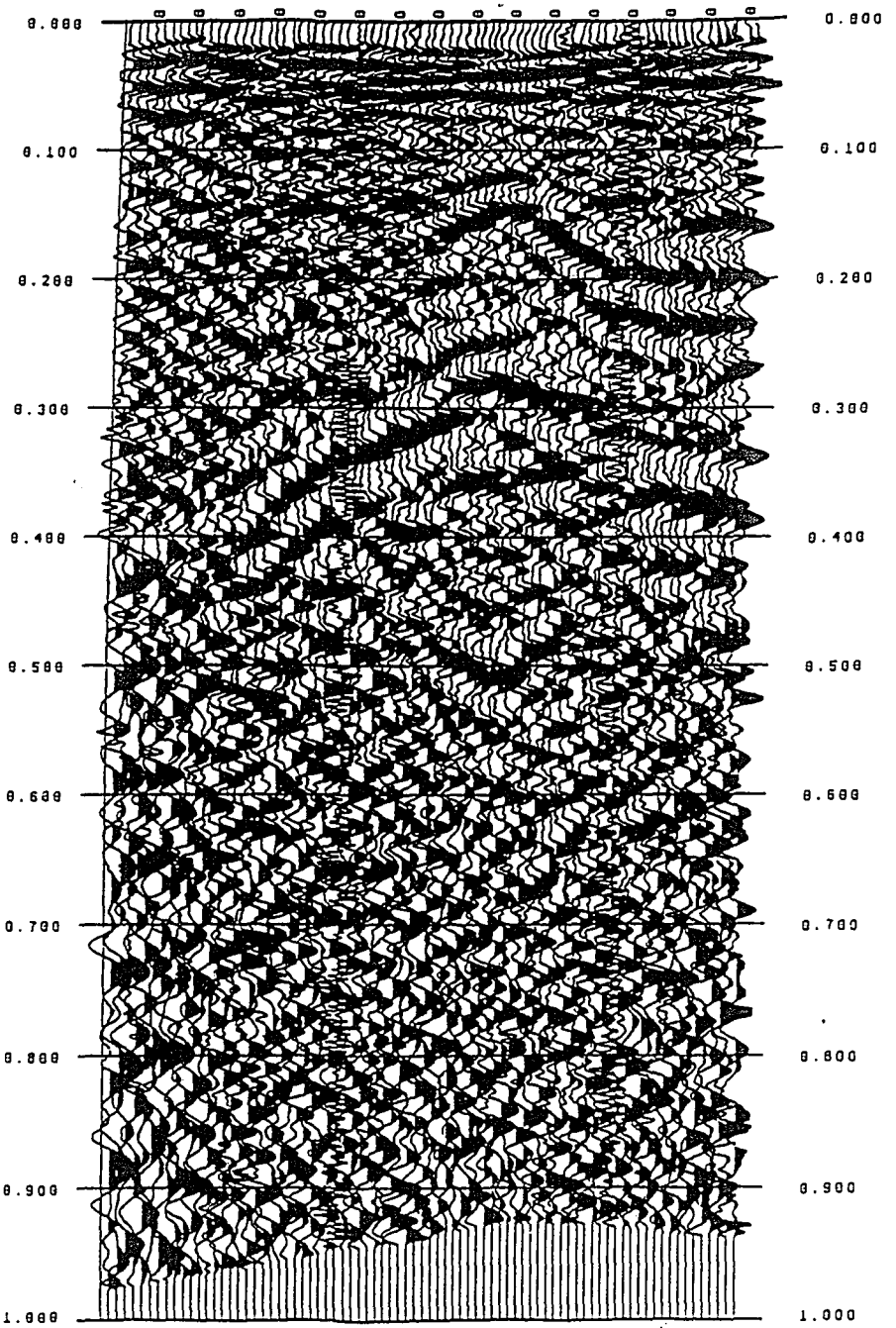

FIGURE 66: Near trace display of Princeton Line 2 after refraction statics corrections modified with least-squares velocities of digitized picks for subweathering velocities and modeled estimated for weathering velocities. Compare static shift with that of the uncorrected near trace display (**Figure 33**). Plotted with AGC (0.13 sec window).

FIGURE 6.7: A plot of several constant velocity stacks used to examing the presence of coherent reflectors after refraction statics corrections. The traces shown are the stacked gathers of PRL2 common midpoint gathers 72 through 80. The velocities shown are: 4400, 4800, 5200, 5600, 5600, 6000, 6400, 6800, 7200 ft/s. Then 10400, 12400, 14400, 16400, 18400, 20400 and 22400 ft/s. Velocities chosen for display represent the range of velocities expected in the PRL2 survey. Although not displayed, continuous constant velocity stacks from 4400 to 22400 ft/s at an increment of 200 ft/s were examined, and "reflectors" seen in the near surface correlated to stacked refractions in the unmuted near traces.

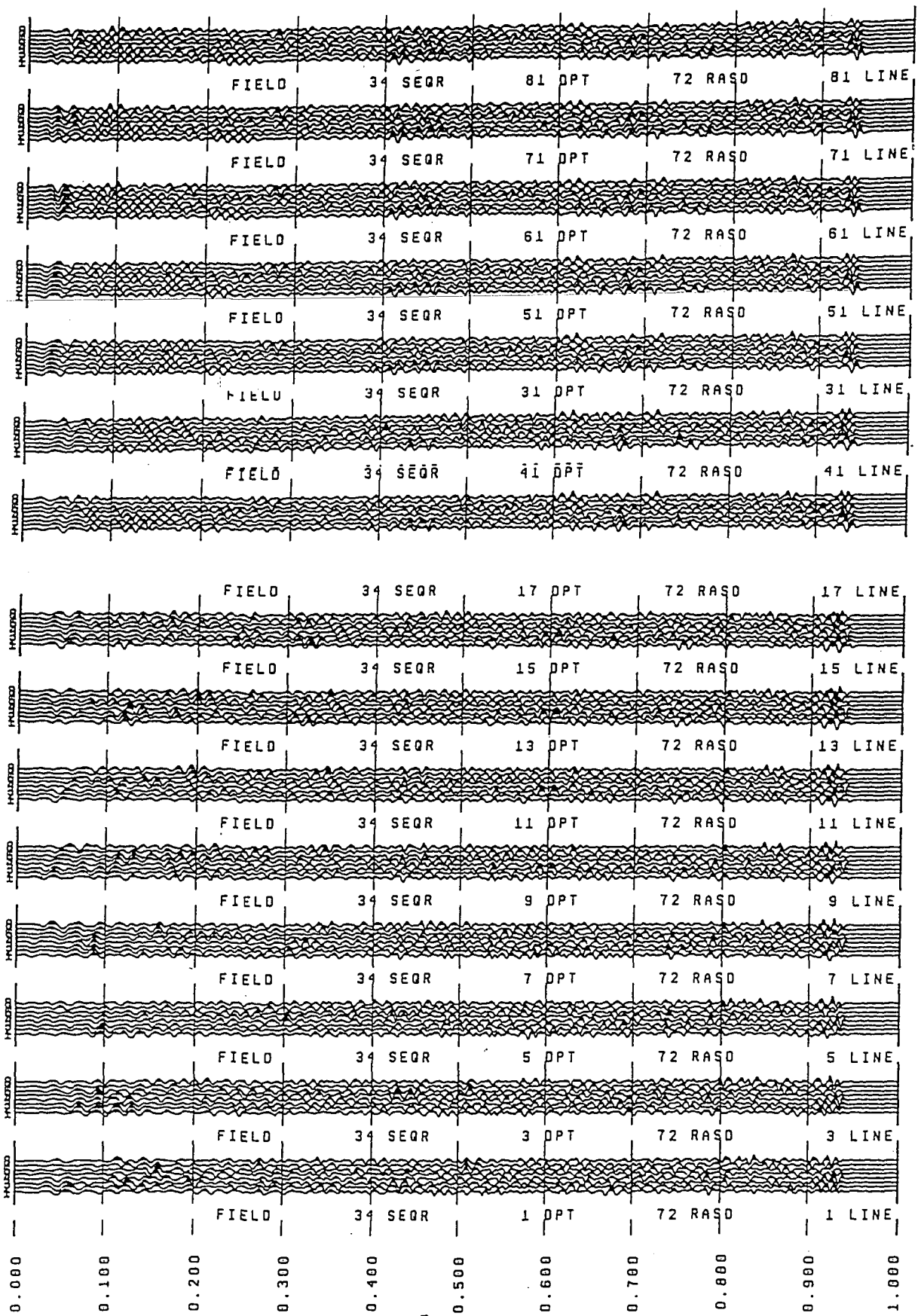
FIELD 34 SEQR 81 OPT 72 RASD 81 LINE
FIELD 34 SEQR 71 OPT 72 RASD 71 LINE
FIELD 34 SEQR 61 OPT 72 RASD 61 LINE
FIELD 34 SEQR 51 OPT 72 RASD 51 LINE
FIELD 34 SEQR 31 OPT 72 RASD 31 LINE
FIELD 34 SEQR 41 OPT 72 RASD 41 LINE
FIELD 34 SEQR 17 OPT 72 RASD 17 LINE
FIELD 34 SEQR 15 OPT 72 RASD 15 LINE
FIELD 34 SEQR 13 OPT 72 RASD 13 LINE
FIELD 34 SEQR 11 OPT 72 RASD 11 LINE
FIELD 34 SEQR 9 OPT 72 RASD 9 LINE
FIELD 34 SEQR 7 OPT 72 RASD 7 LINE
FIELD 34 SEQR 5 OPT 72 RASD 5 LINE
FIELD 34 SEQR 3 OPT 72 RASD 3 LINE
FIELD 34 SEQR 1 OPT 72 RASD 1 LINE
0.000
0.100
0.200
0.300
0.400
0.500
0.600
0.700
0.800
0.900
1.000

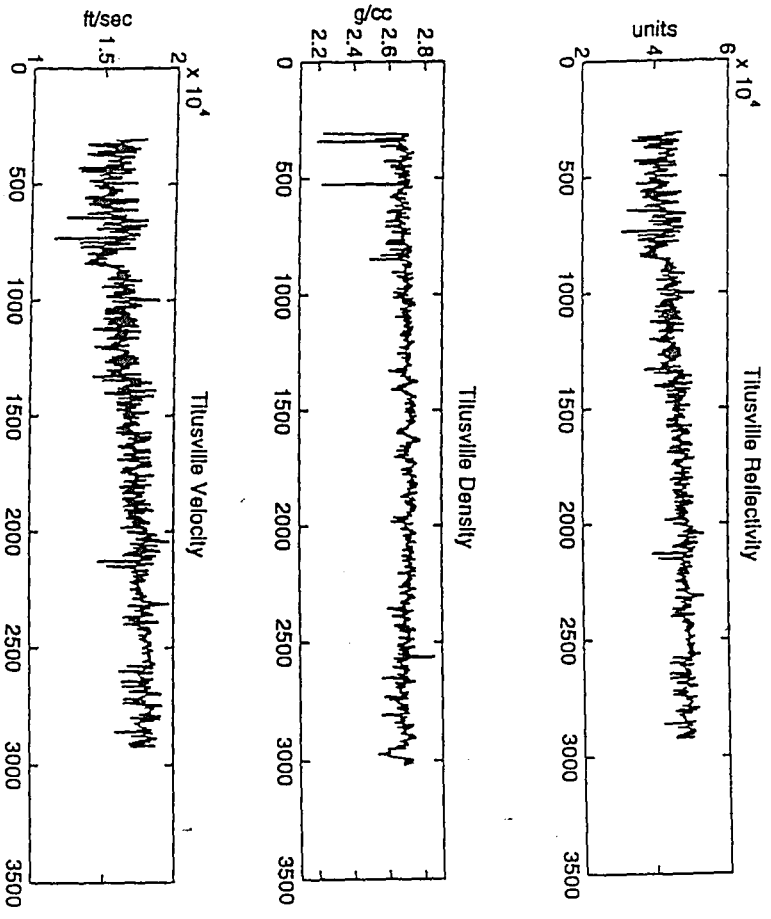

FIGURE 68: Titusville plots of the velocity (right) and density (center) logs provided by the Lamont-Doherty Earth Observatory; and the calculated reflectivity (left). The vertical scale is depth in feet.

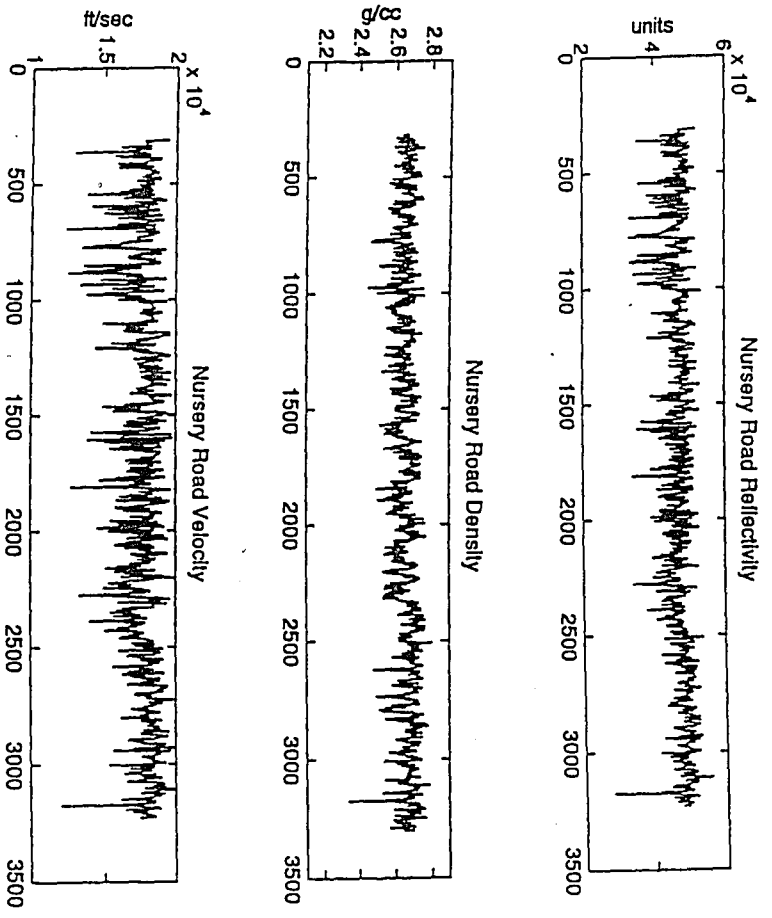

FIGURE 69: Nursery Road plots of velocity (right) and density (center) logs provided by the Lamont-Doherty Earth Observatory; and the calculated reflectivity (left). The vertical scale is depth in feet.

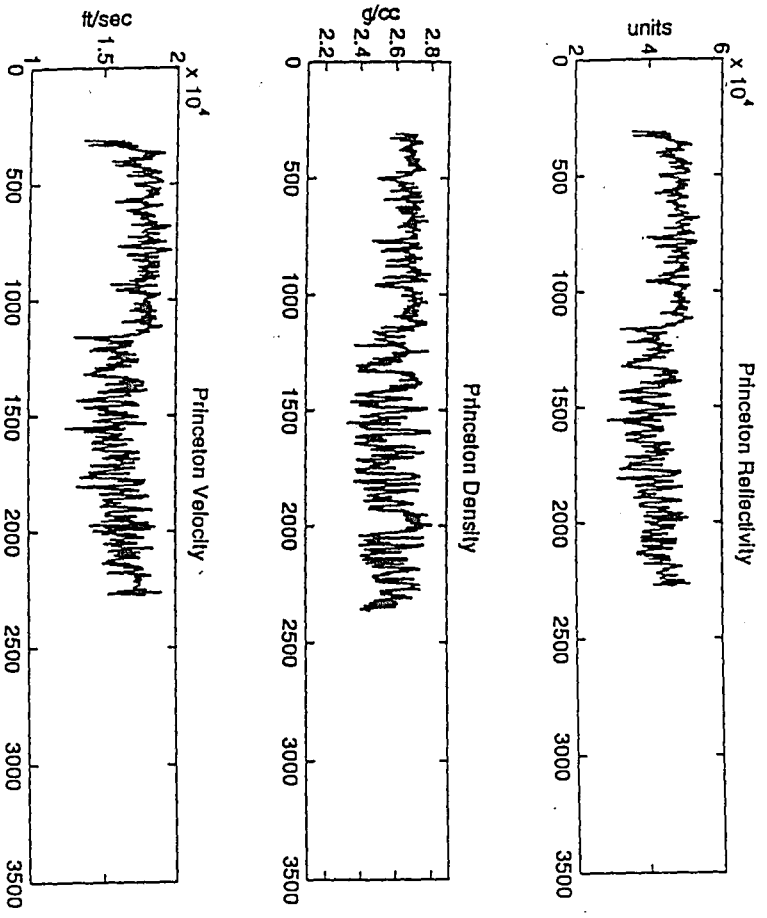

FIGURE 70: Princeton plots of velocity (right) and density (center) logs provided by the Lamont-Doherty Earth Observatory; and the calculated reflectivity (left). Vertical scale is depth in feet.

FIGURE 71: Plots of synthetic seismograms from the Titusville reflectivity series. From left to right: **1**) Unfiltered synthetic seismogram of primary reflections associated with the Titusville reflectivity series. Note the prominant amplitude excursions. Scaled by a factor of 110. **2**) Synthetic seismogram representing a low frequency source with frequencies of 5 Hz to 160 Hz. Scaled by a factor of 118 . **3**) Synthetic siesmogram for a medium-frequency source with frequencies from 10 to 240 Hz. Scaled by a factor of 115. **4**) Synthetic seismogram representing a high frequency source with frequencies of 50 Hz to 420 Hz. Scaled by a factor of 112. **5**) Synthetic seismogram of Titusville correlating to the amplitude spectra seen in Washington Crossing Line 2, with frequencies from 5 to 160 Hz. Scaled by a factor of 118. **6**) Synthetic seismogram of Titusville representing a frequency content of 5 to 160 Hz, with a S/N ratio of 2. Scaled by a factor of 118. The visibility of reflectors with a S/N ratio of 2 suggests that if there were no near surface problems, reflection would be recorded in the field records given the same parameters used in the Washington Crossing and Princeton experiments.

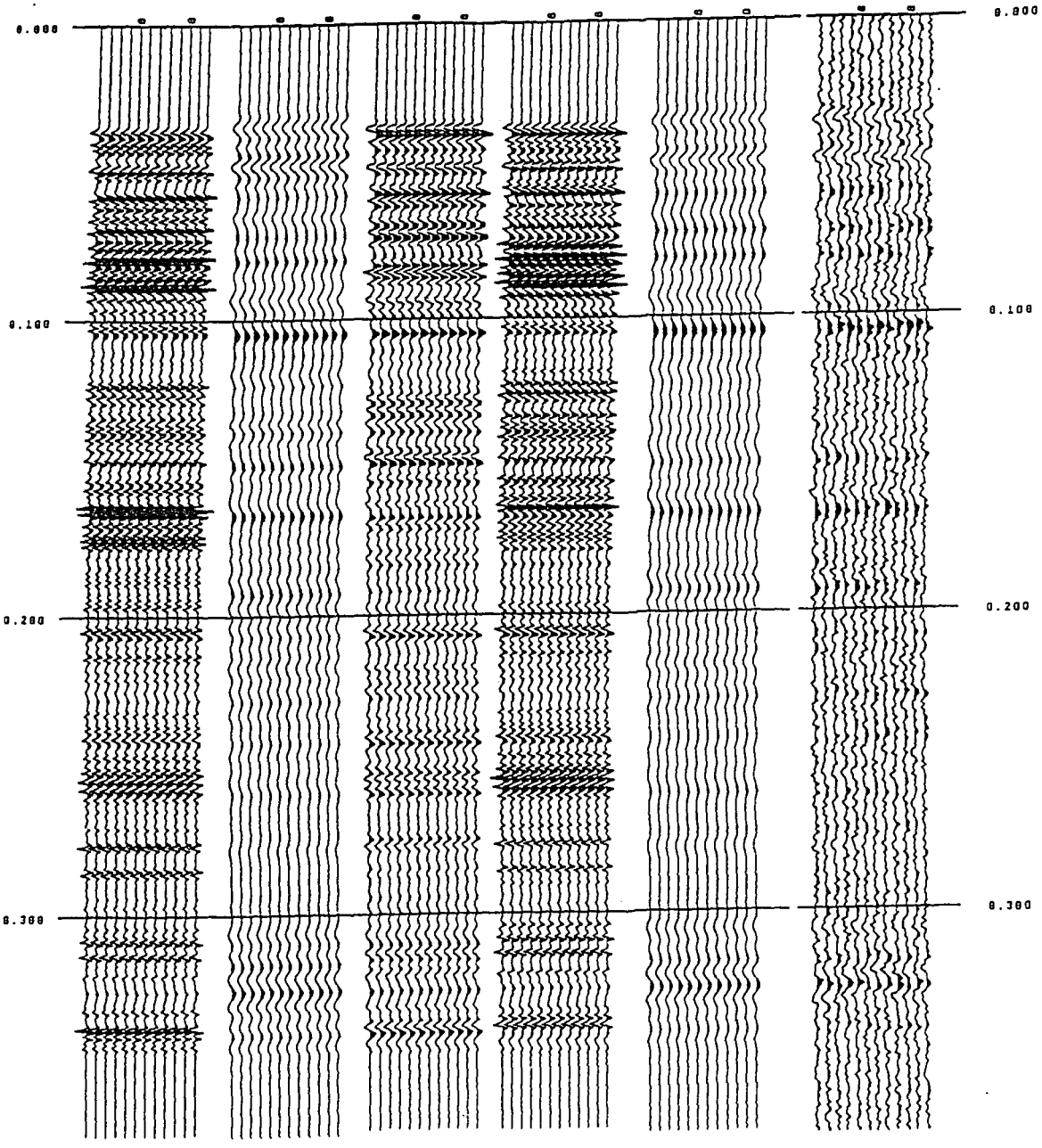
0.000
0.100
0.200
0.300
0.000
0.100
0.200
0.300

FIGURE 72: Plots of synthetic seismograms from the Nursery Road reflectivity series. From left to right: **1**) Unfiltered synthetic seismogram of primary reflections associated with the Nursery Road reflectivity series. Note the prominant amplitude excursions. Scaled by a factor of 110. **2**) Synthetic seismogram representing a low frequency source with frequencies of 5 Hz to 160 Hz. Scaled by a factor of 118 . **3**) Synthetic siesmogram for a medium-frequency source with frequencies from 10 to 240 Hz. Scaled by a factor of 115. **4**) Synthetic seismogram representing a high frequency source with frequencies of 50 Hz to 420 Hz. Scaled by a factor of 112. **5**) Synthetic seismogram correlating to the amplitude spectra seen in Washington Crossing Line 2, with frequencies from 5 to 160 Hz. Scaled by a factor of 118. **6**) Synthetic seismogram representing a frequency content of 5 to 160 Hz, with a S/N ratio of 2. Scaled by a factor of 118. The visibility of reflectors with a S/N ratio of 2 suggests that if there were no near surface problems, reflection would be recorded in the field records given the same parameters used in the Washington Crossing and Princeton experiments.

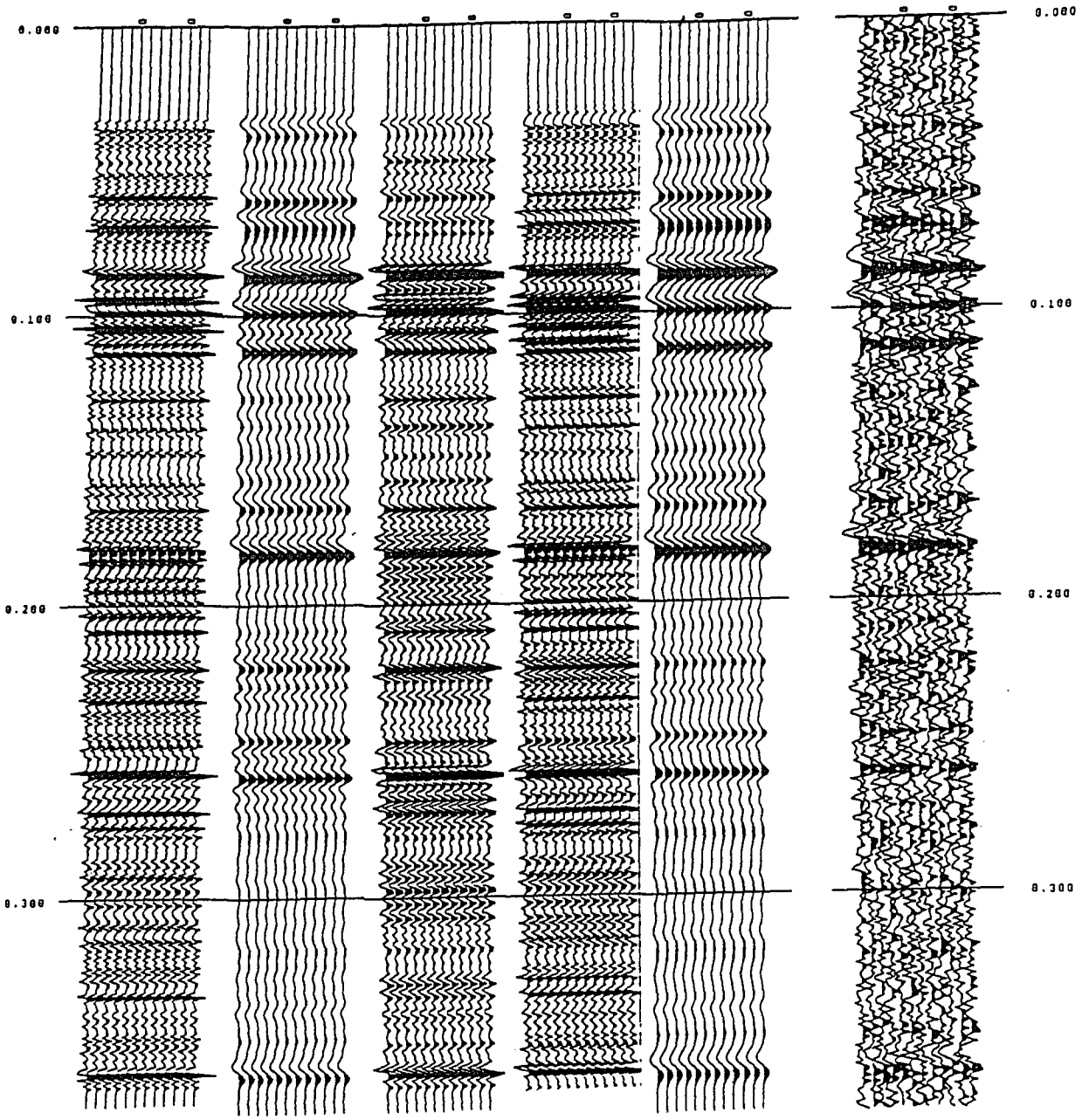
0.000
0.100
0.200
0.300
0.000
0.100
0.200
0.300

FIGURE 73: Plots of synthetic seismograms from the Princeton reflectivity series. From left to right: **1**) Unfiltered synthetic seismogram of primary reflections associated with the Princeton reflectivity series. Note the prominant amplitude excursions. Scaled by a factor of 110. **2**) Synthetic seismogram representing a low frequency source with frequencies of 5 Hz to 160 Hz. Scaled by a factor of 118 . **3**) Synthetic siesmogram for a medium-frequency source with frequencies from 10 to 240 Hz. Scaled by a factor of 115. **4**) Synthetic seismogram representing a high frequency source with frequencies of 50 Hz to 420 Hz. Scaled by a factor of 112. **5**) Synthetic seismogram correlating to the amplitude spectra seen in Princeton Line 2, with frequencies from 5 to 160 Hz. Scaled by a factor of 118. **6**) Synthetic seismogram representing a frequency content of 5 to 160 Hz, with a S/N ratio of 2. Scaled by a factor of 118. The visibility of reflectors with a S/N ratio of 2 suggests that if there were no near surface problems, reflection would be recorded in the field records given the same parameters used in the Washington Crossing and Princeton experiments.

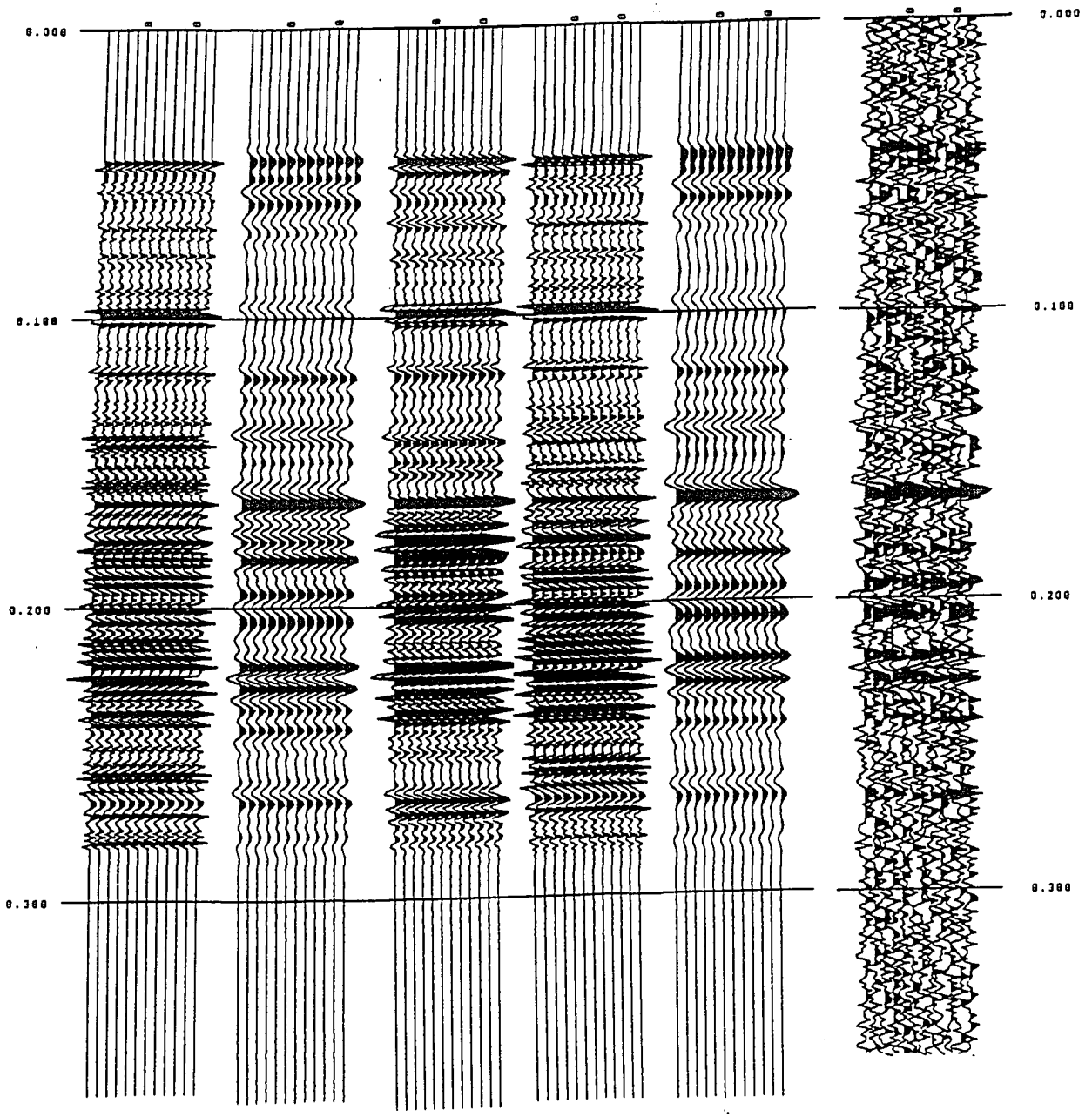
0.000
0.100
0.200
0.300
0.000
0.100
0.200
0.300

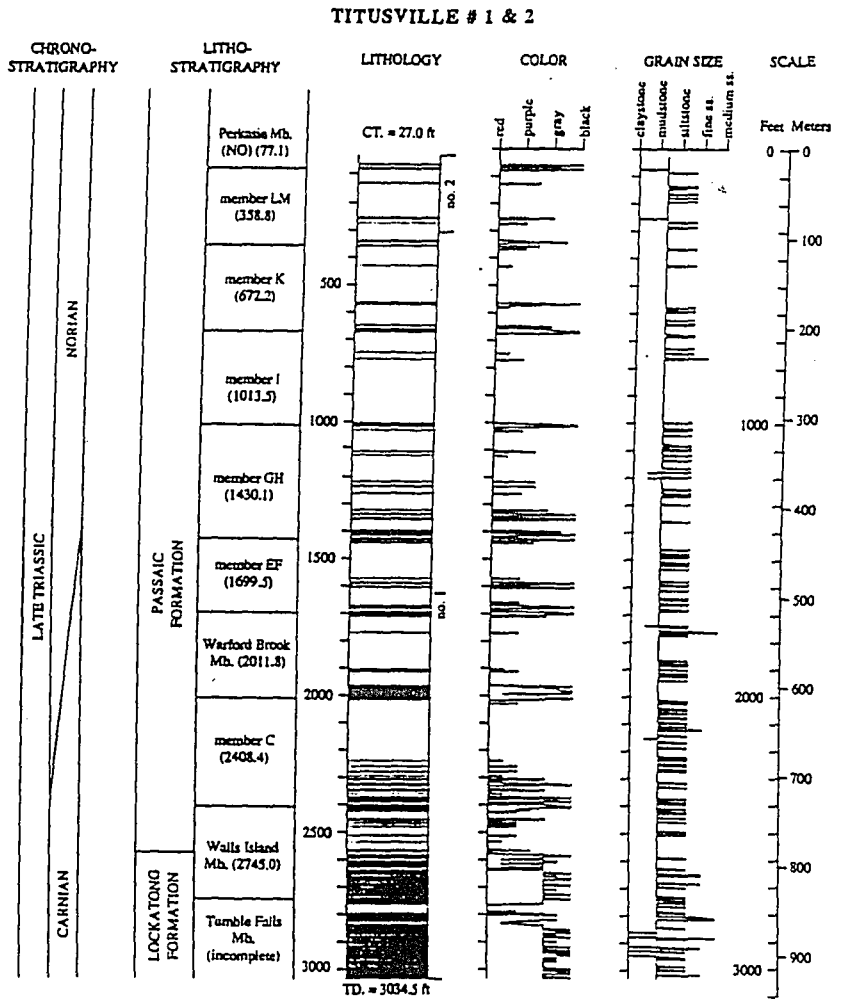

FIGURE 74: Chrono-stratigraphy, lithostratigraphy, Depth Rank (black = 6), color and grain size for the Titusville cores (from Olsen, per. comm.). Titusville #2 represents the upper section of th core hole which was drilled in a weathered zone, and then cased. Titusville #1 is the data used in this study. The lithology is a representation of depth rank, with darker colors representing deeper lake levels.

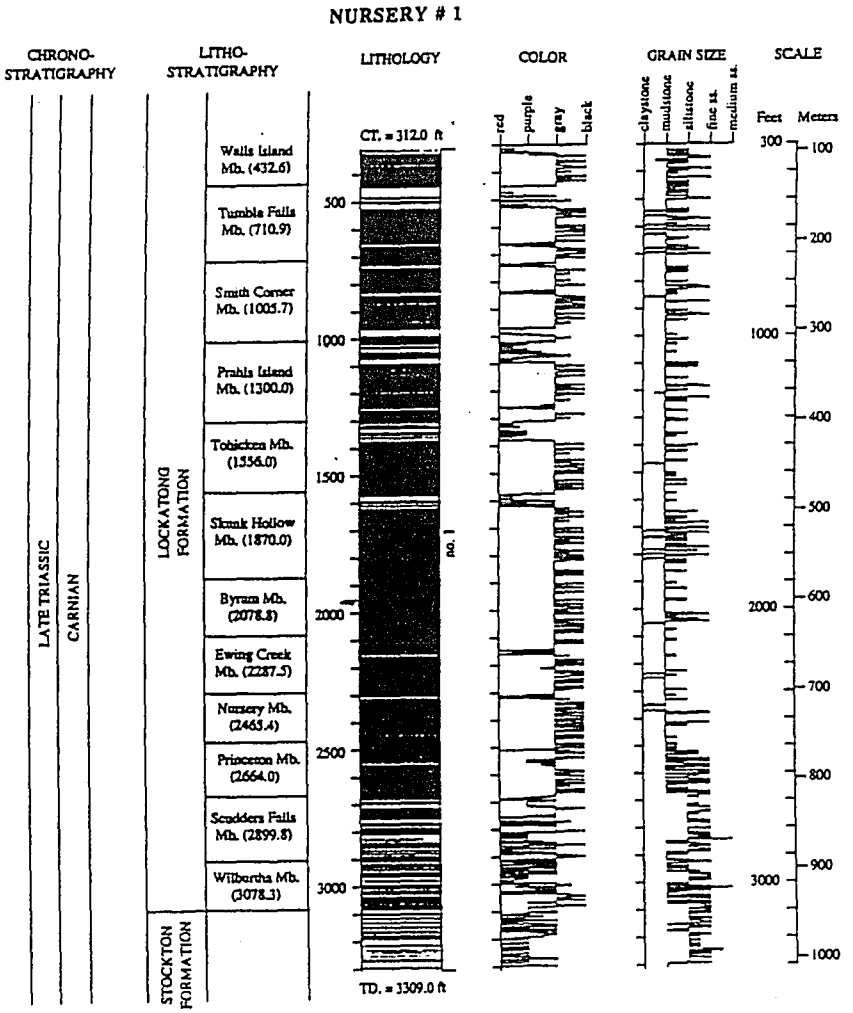

FIGURE 75: Chrono-stratigraphy, lithostratigraphy, Depth rank (black = 6), color and grain size for the Nursery Road cores (from Olsen, per. comm.). The lithology is a representation of depth rank, with darker colors representing deeper lake levels.

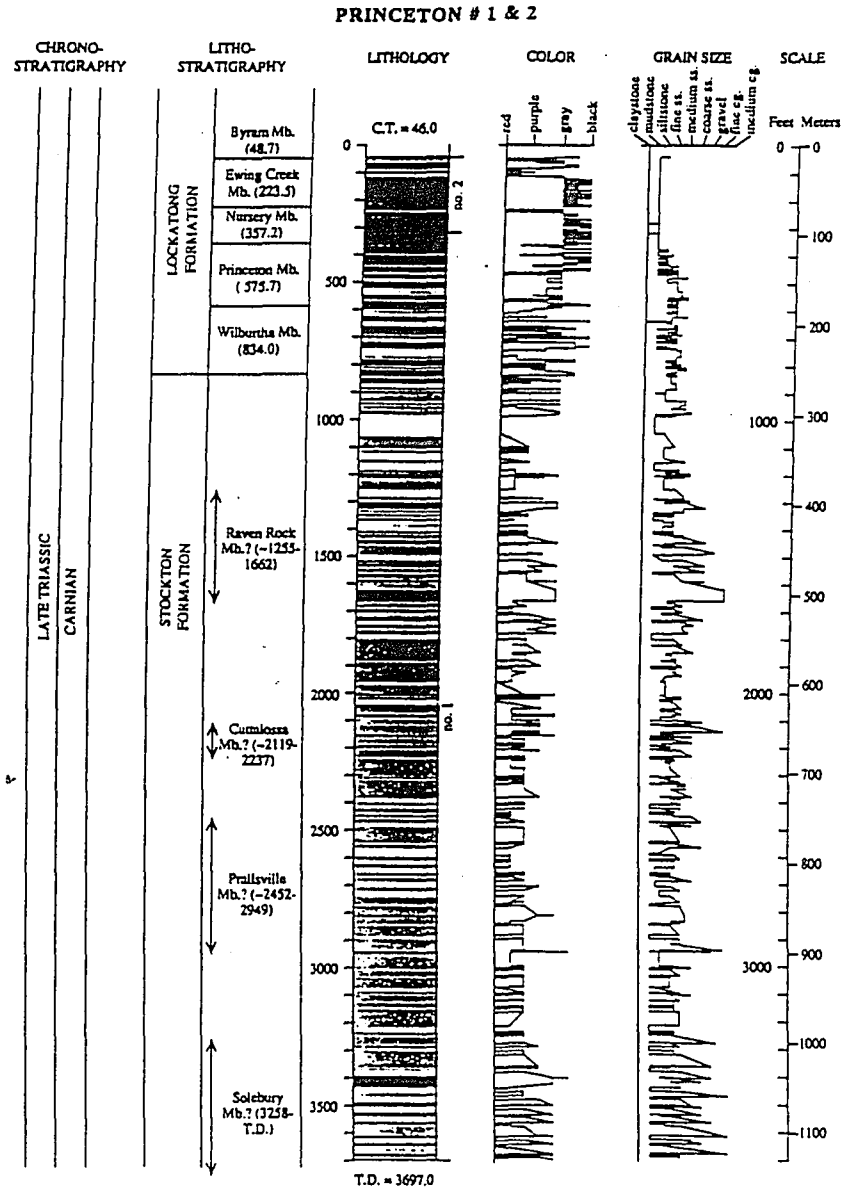

FIGURE 76: Chrono-stratigraphy, lithostratigraphy, Depth Rank (black = 6), color and grain size for the Princeton cores (from Olsen, per. comm.). Princeton #2 represents the upper section of th core hole which was drilled in a weathered zone, and then cased. Princeton #1 is the data used in this study. The lithology is a representation of depth rank, with darker colors representing deeper lake levels.

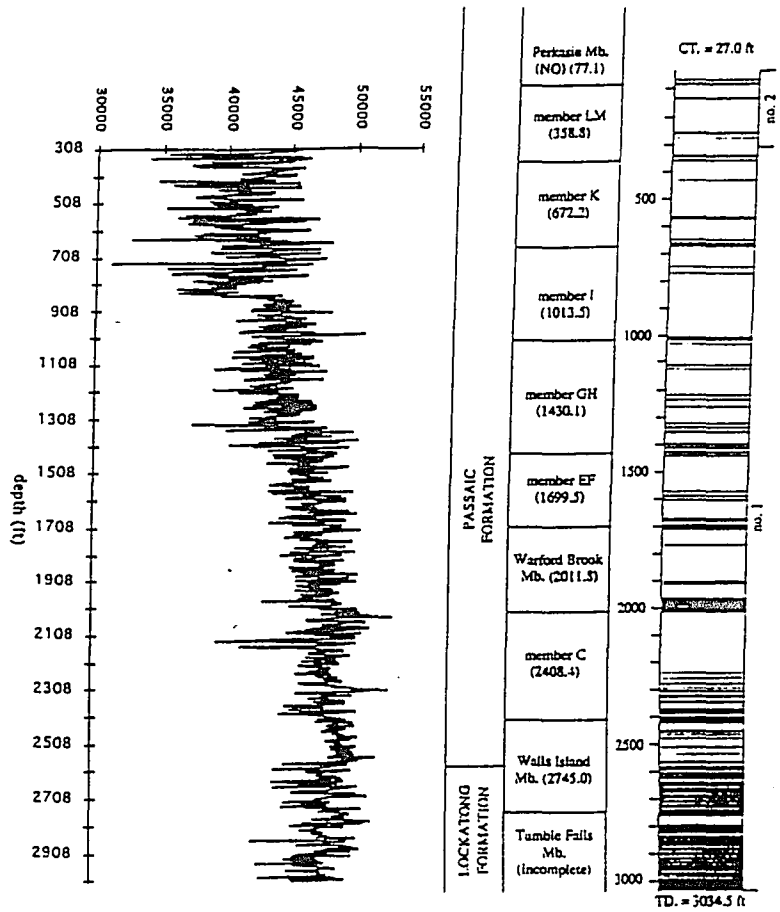

FIGURE 77: A plot comparing the reflectivity series generated from the sonic velocity and density log data with depth rank for the Titusville core, which records the Passaic Formation and the extreme upper Lockatong. The darker shades represent deeper lake depth. Vertical depth scale is in feet.

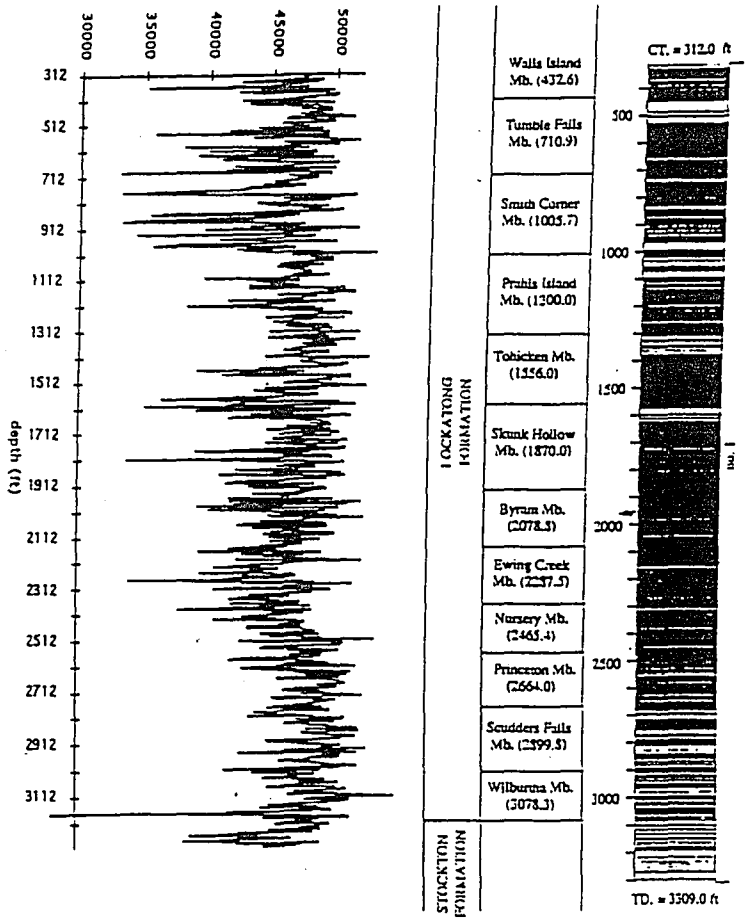

FIGURE 78: A plot comparing the reflectivity series generated from the sonic velocity and density log data with depth rank, for the Nursey Road core, which records the Lockatong Formation. The darker shades represent deeper lake depth. Vertical depth scale is in feet.

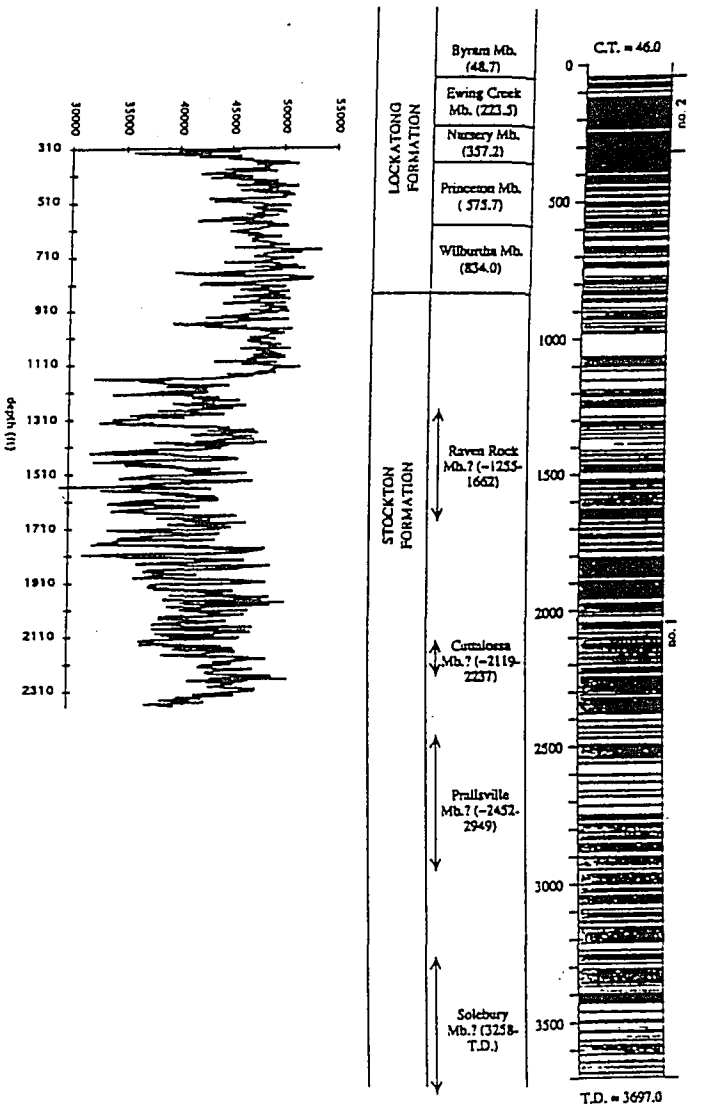

FIGURE 79: A plot comparing the reflectivity series generated from the sonic velocity and density log data with depth rank for the Princeton core, which records the lowest Lockatong Formation and the Stockton Formation. The darker shades representing deeper lake depth. Vertical depth scale is in feet.

FIGURE 80: A plot of litho-stratigraphy (from Olsen, submitted) correlated to the synthetic seimogram from the Titusville reflectivity series generated with a filter to match the expected frequencies seen in the Washington Crossing Lines as per **Figure 71** (5 to 160 Hz). Correlation provided by matching depth from reflectivity series with depth of litho-stratigraphy. Note the excellent correlation between positive excursions on the synthetic seismogram and deepest lake level represented on the lithology column by the darkest shades.

TITUSVILLE # 1 & 2

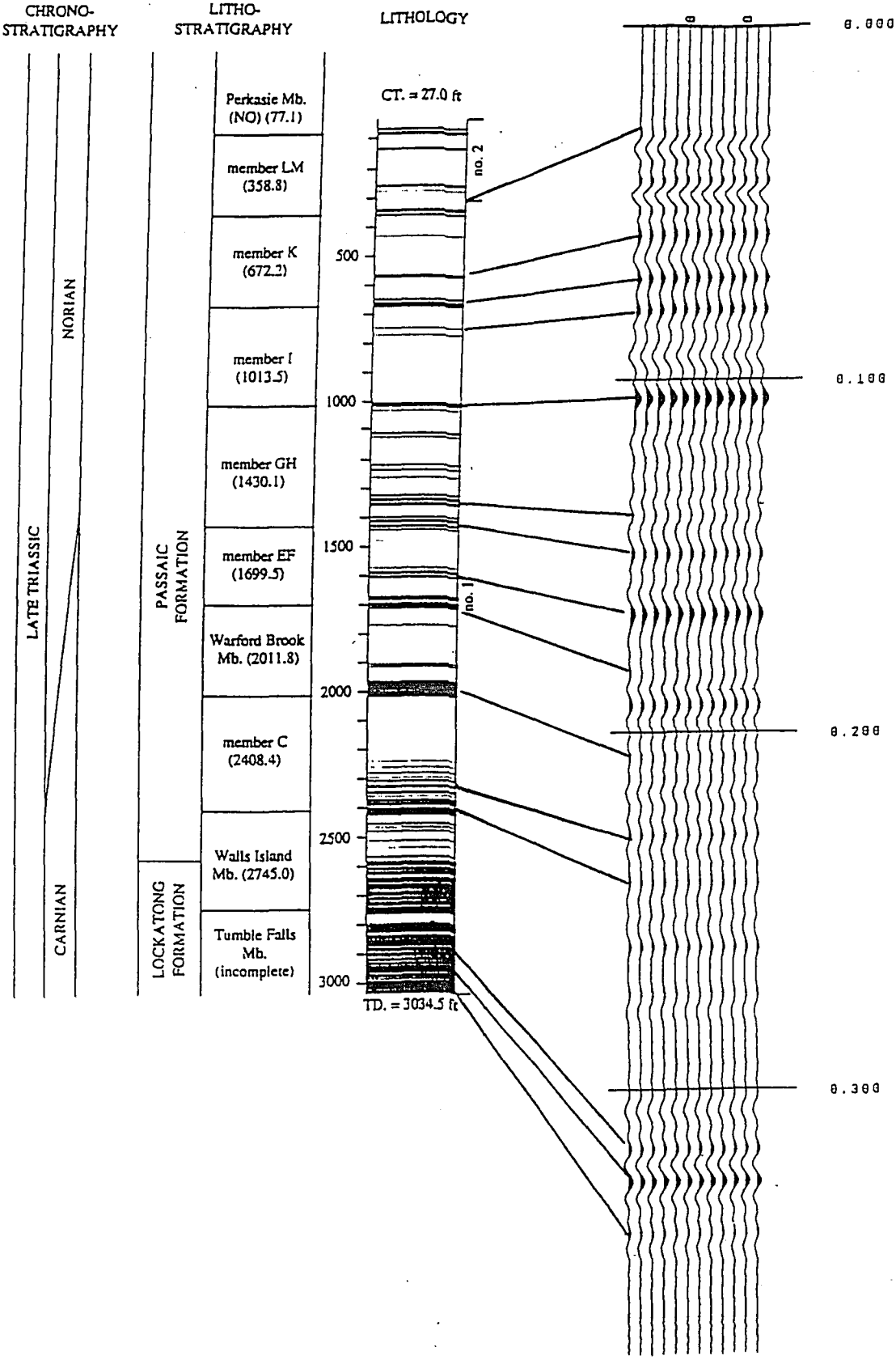

FIGURE 81: A plot of litho-stratigraphy (from Olsen, submitted) correlated to the synthetic seimogram from the Nursery Road reflectivity series generated with a filter to match the expected frequencies seen in the Washington Crossing Lines as per **Figure 72** (5 to 160 Hz). Correlation provided by matching depth from reflectivity series with depth of litho-stratigraphy. Note the excellent correlation between positive excursions on the synthetic seismogram and deepest lake level represented on the lithology column by the darkest shades.

NURSERY # 1

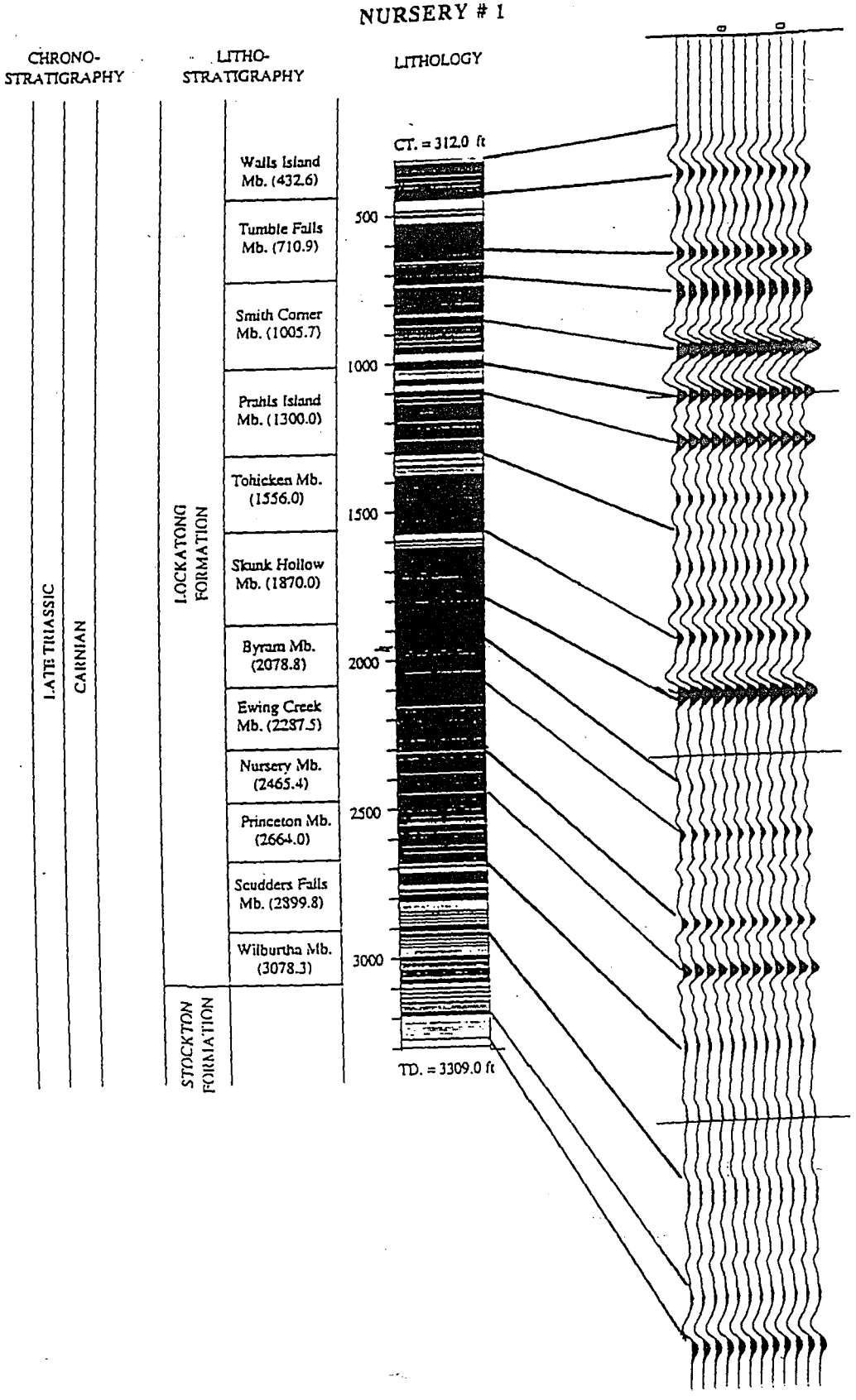
CHRONO-STRATIGRAPHY
LITHO-STRATIGRAPHY
LITHOLOGY
LATE TRIASSIC
CARNIAN
LOCKATONG FORMATION
STOCKTON FORMATION
Walls Island Mb. (432.6)
Tumble Falls Mb. (710.9)
Smith Corner Mb. (1005.7)
Prahls Island Mb. (1300.0)
Tohicken Mb. (1556.0)
Skunk Hollow Mb. (1870.0)
Byram Mb. (2078.8)
Ewing Creek Mb. (2287.5)
Nursery Mb. (2465.4)
Princeton Mb. (2664.0)
Scudders Falls Mb. (2899.8)
Wilburtha Mb. (3078.3)
CT. = 312.0 ft
500
1000
1500
2000
2500
3000
TD. = 3309.0 ft

FIGURE 82: A plot of litho-stratigraphy (from Olsen, submitted) correlated to the synthetic seimogram from the Princeton reflectivity series generated with a filter to match the expected frequencies seen in the Princeton Lines as per **Figure 73** (5 to 160 Hz). Correlation provided by matching depth from reflectivity series with depth of litho-stratigraphy. Note the excellent correlation between positive excursions on the synthetic seismogram and deepest lake level represented on the lithology column by the darkest shades.

PRINCETON # 1 & 2

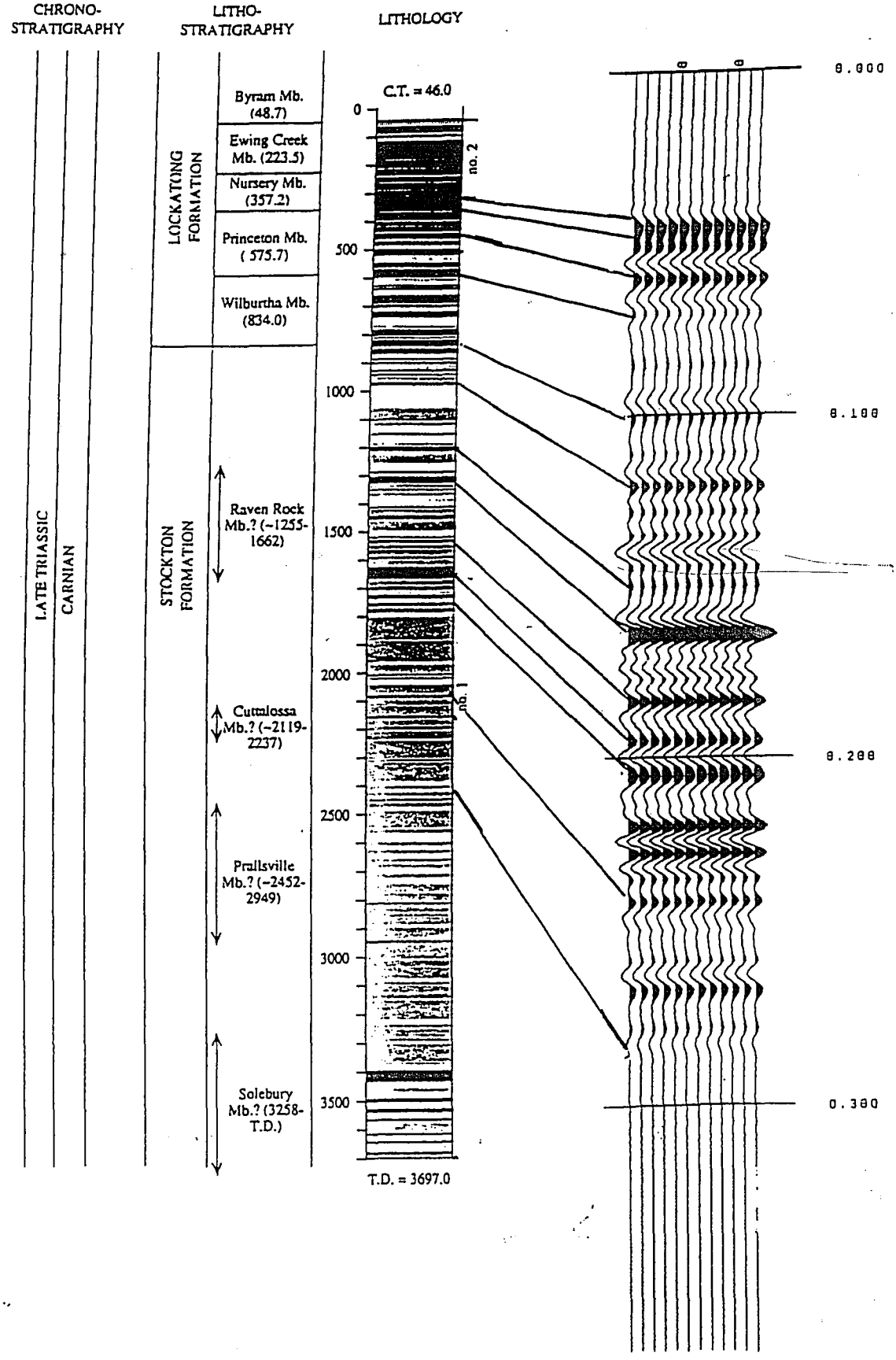

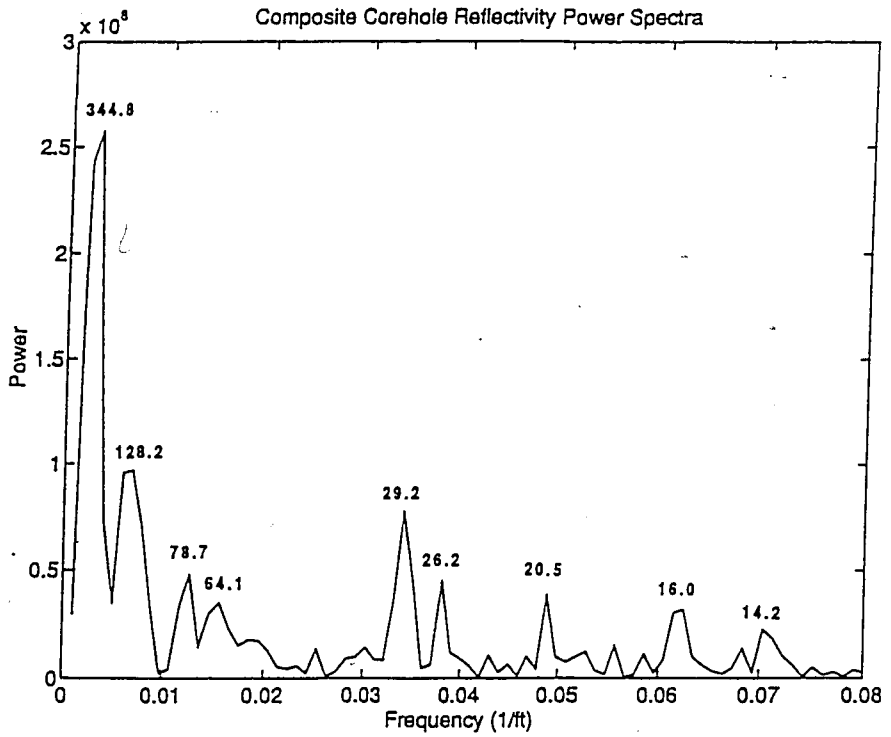

FIGURE 83: Spectral analysis of the reflectivity series generated by combining the Titusville, Nursery Road, and Princeton logs. The numerated peaks represent periodic signal in the reflectivity series with the given depth. Converting periodicities in depth to time using a constant sedimentation rate of 0.7283 ft/ky (from Olsen, 1986) yields close matches with orbital periodicities (see text).

FIGURE 84: Plots of the Titusvilles reflectivity series with 30 ft, 100 ft and 300 ft smoothing windows. The bold-faces depth and time in each plot represents the corresponding value of the bars matching peaks in the reflectivity series. Overlap or spacing between bars suggests deviations in the 0.7283 ft/ky (22.2 cm/ky) sedimentation rate used to scale the bars.

Titusville Reflectivity

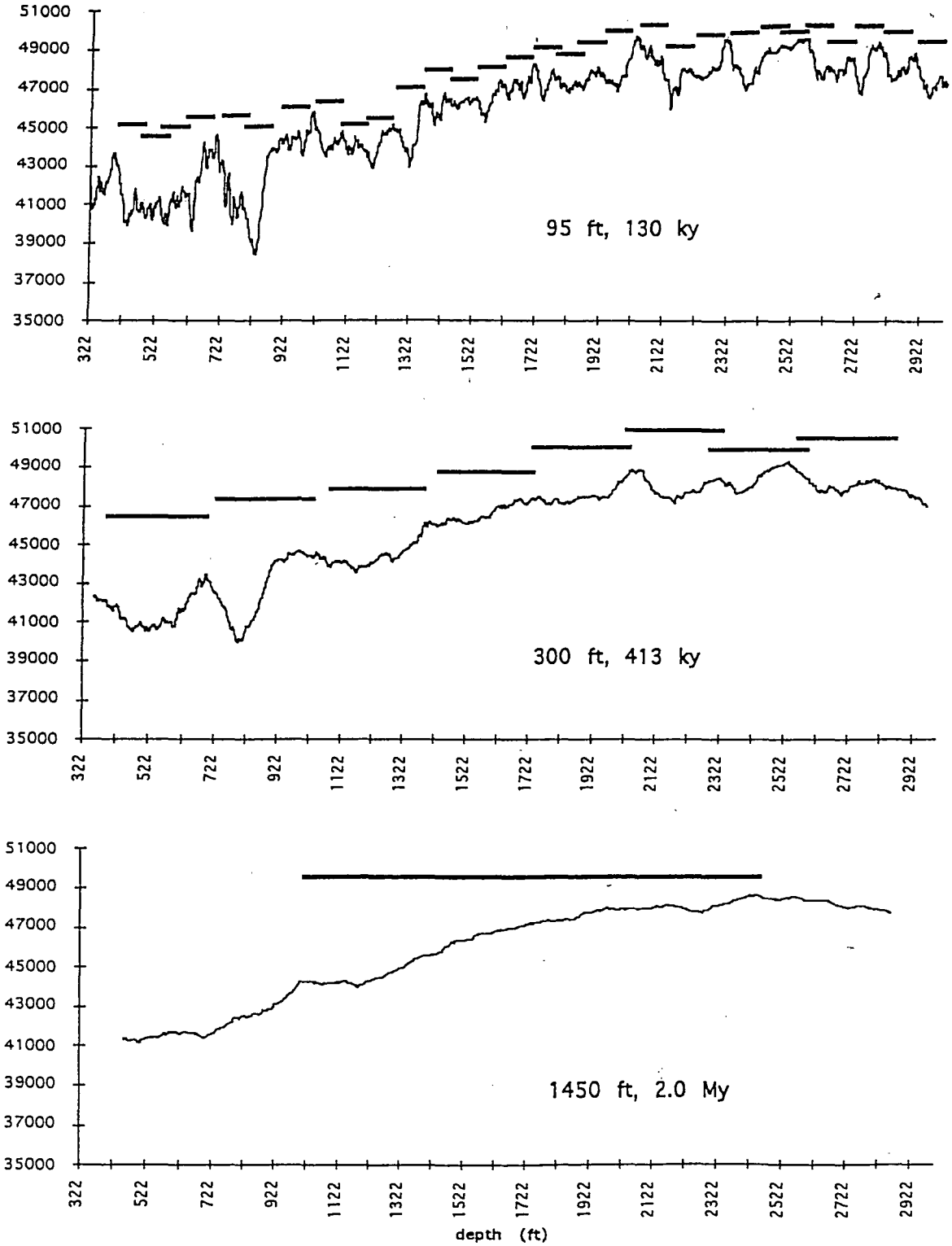

FIGURE 85: Plots of the Nursery Road reflectivity series with 30 ft, 100 ft and 300 ft smoothing windows. The bold-faces depth and time in each plot represents the corresponding value of the bars matching peaks in the reflectivity series. Overlap or spacing between bars suggests deviations in the 0.7283 (22.2 cm/ky) sedimentation rate used to scale the bars.

Nursery Road Reflectivity

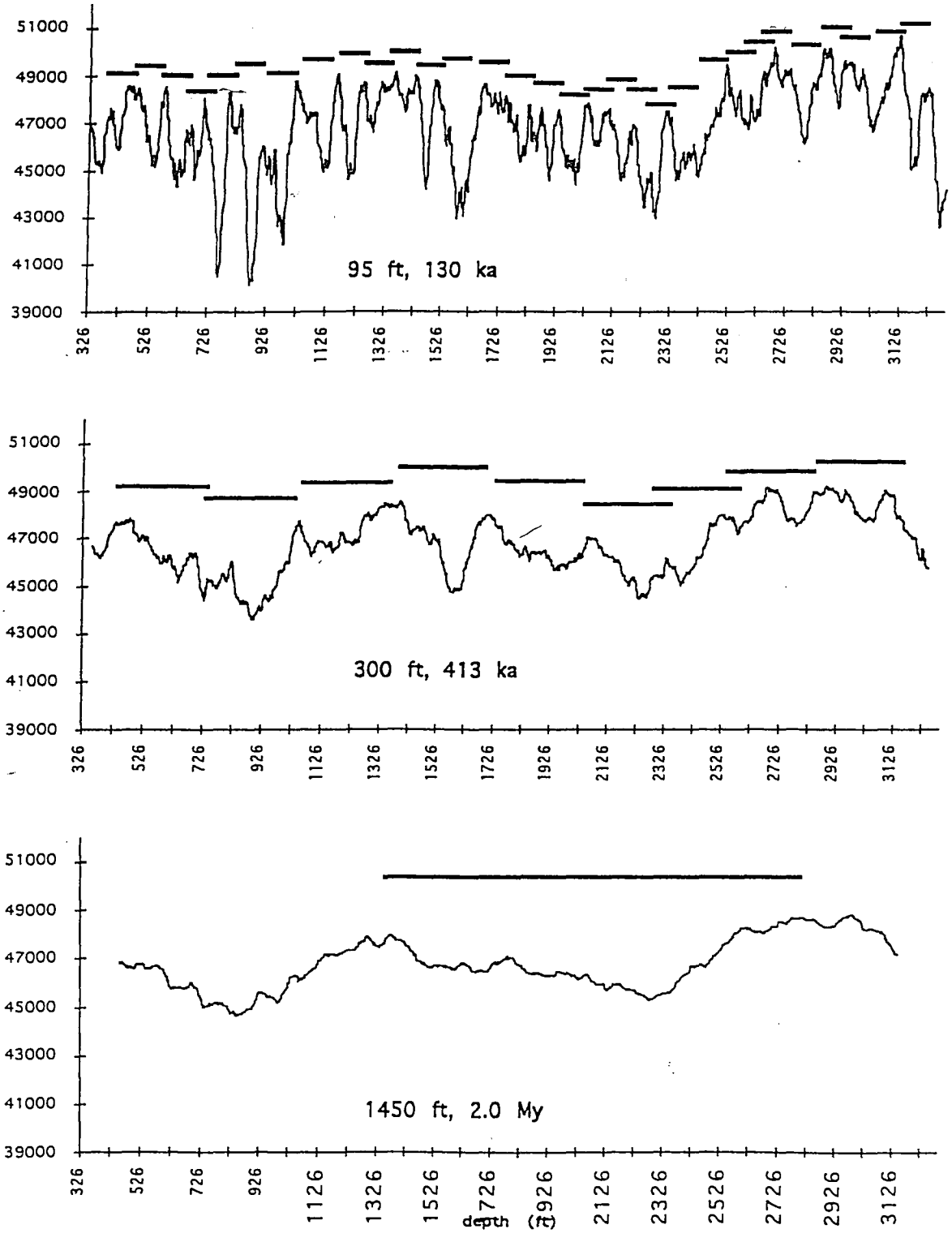

FIGURE 86: Plots of the Princeton reflectivity series with 30 ft, 100 ft and 300 ft smoothing windows. The bold-faces depth and time in each plot represents the corresponding value of the bars matching peaks in the reflectivity series. Overlap or spacing between bars suggests deviations in the 0.7283 (22.2 cm/ky) sedimentation rate used to scale the bars.

Princeton Reflectivity

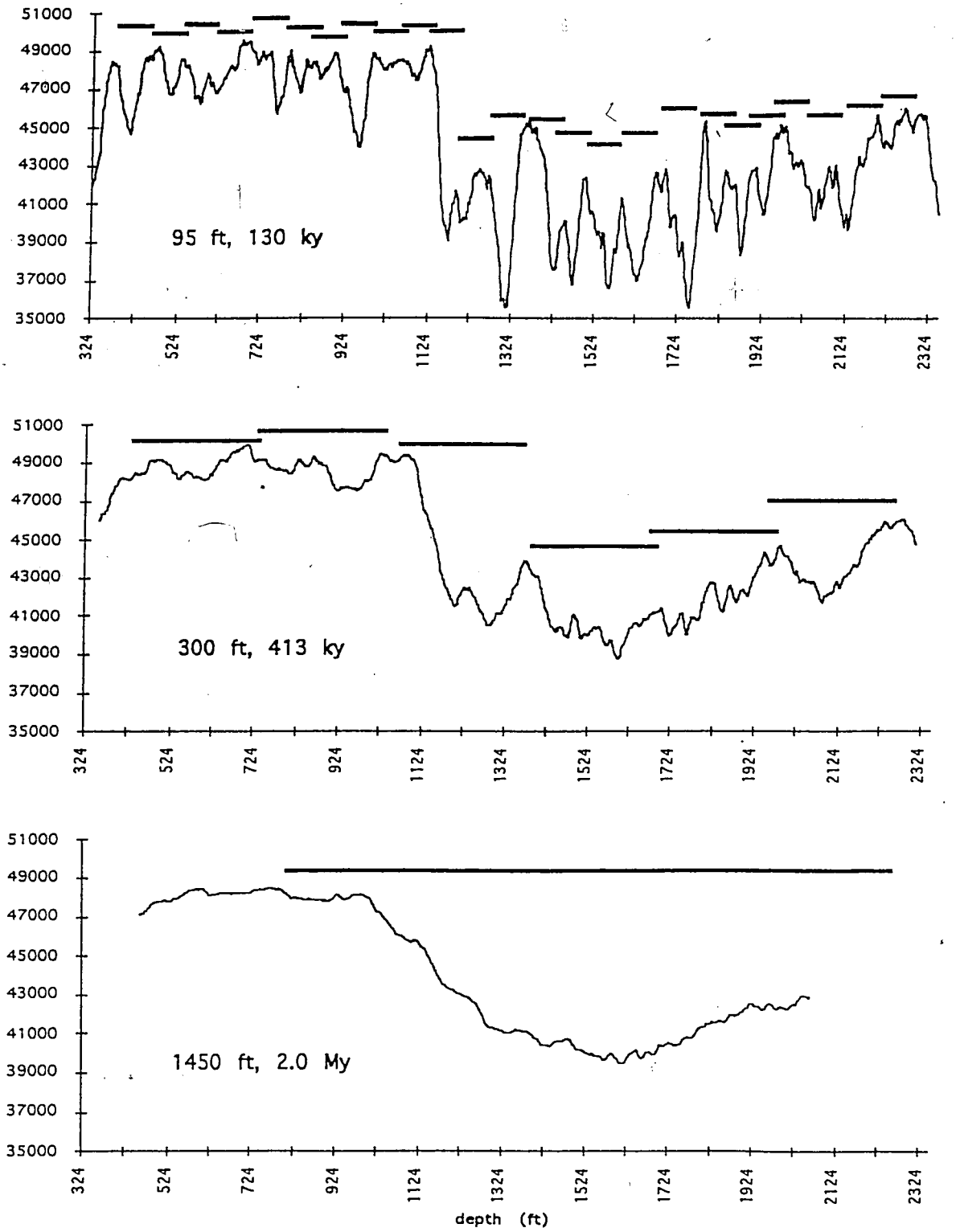

FIGURE 87: Plots of the compound reflectivity series with 100 ft and 300 ft smoothing windows. The bold-faces depth and time in each plot represents the corresponding value of the bars matching peaks in the reflectivity series. Overlap or spacing between bars suggests deviations in the 0.7283 ft ky (22.2 cm/ky) sedimentation rate used to scale the bars.

Compound Corehole Reflectivity

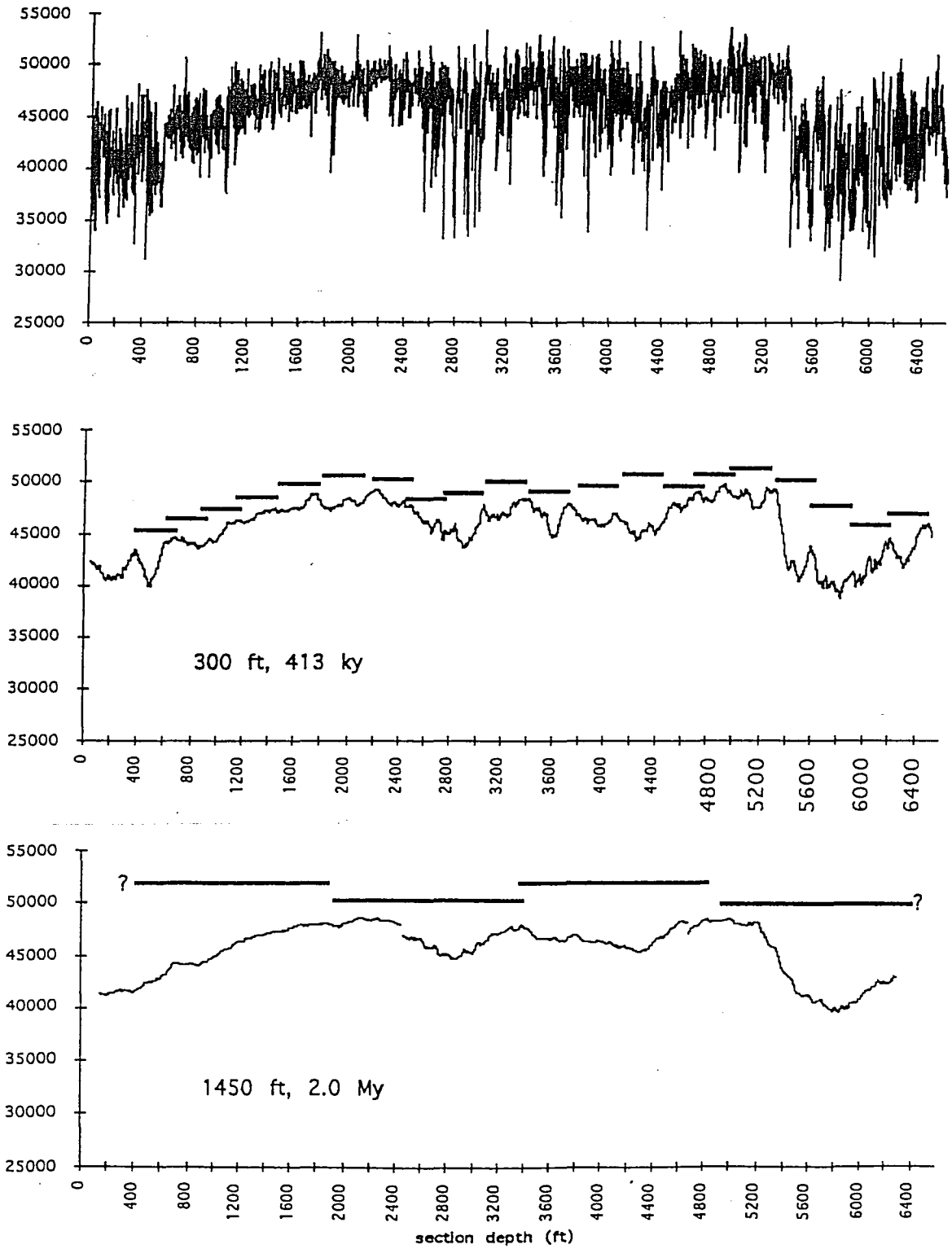

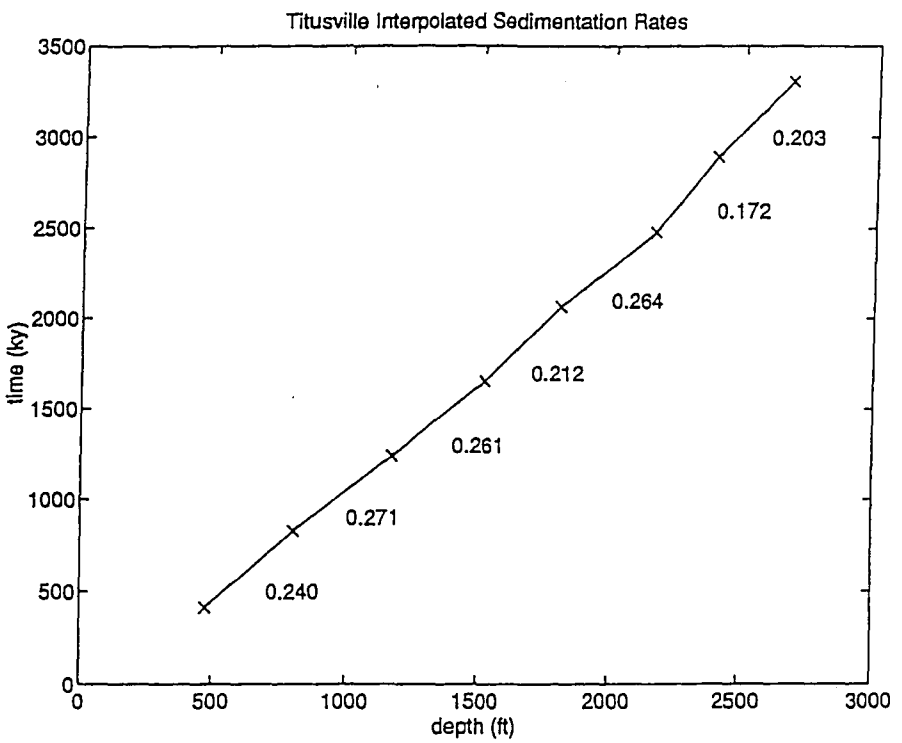

FIGURE 88: Sedimentation rates in mm/yr calculated by fixing the peaks associated with the 413 ky cycles at a regular spacing of 413 ky for the Titusville reflectivity series.

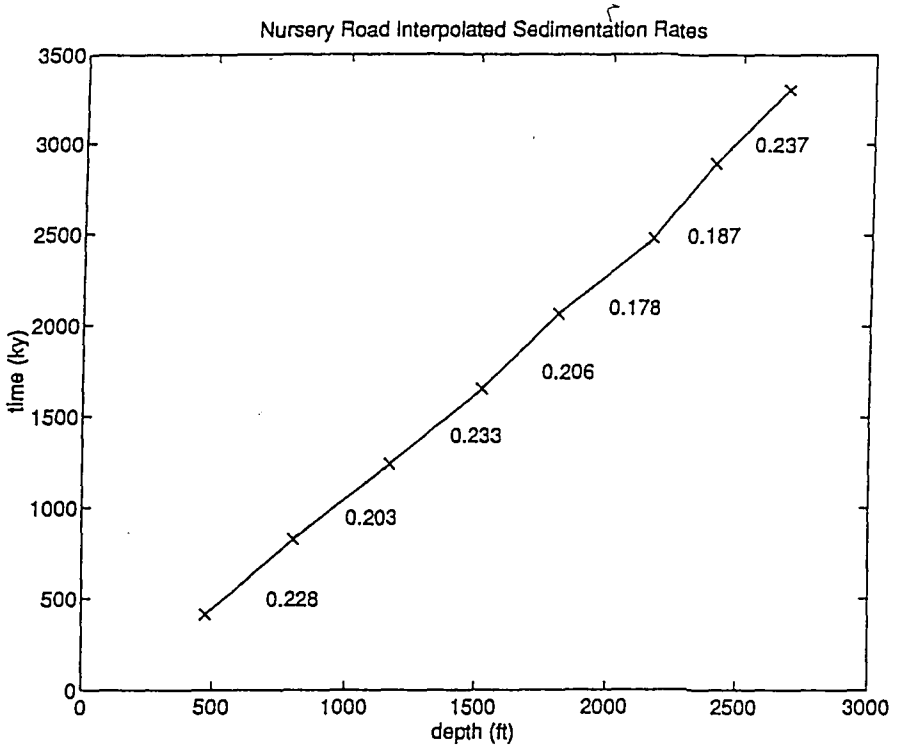

FIGURE 89: Sedimentation rates in mm/yr calculated by fixing the peaks associated with the 413 ky cycles at a regular spacing of 413 ky for the Nursery Road reflectivity series.

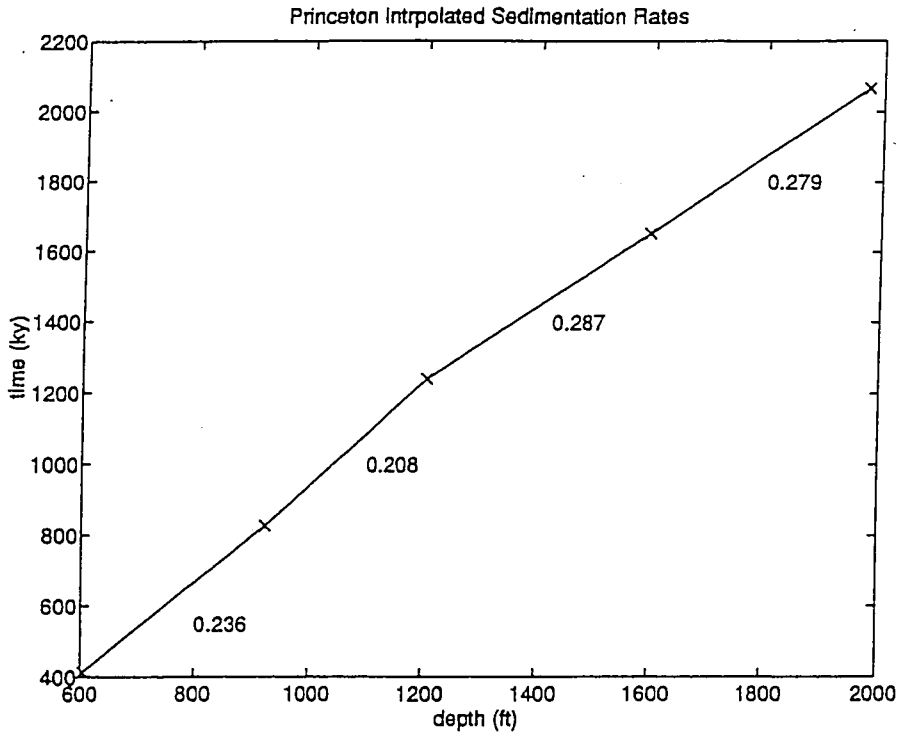

FIGURE 90: Sedimentation rates in mm/yr calculated by fixing the peaks associated with the 413 ky cycles at a regular spacing of 413 ky for the Princeton reflectivity series.

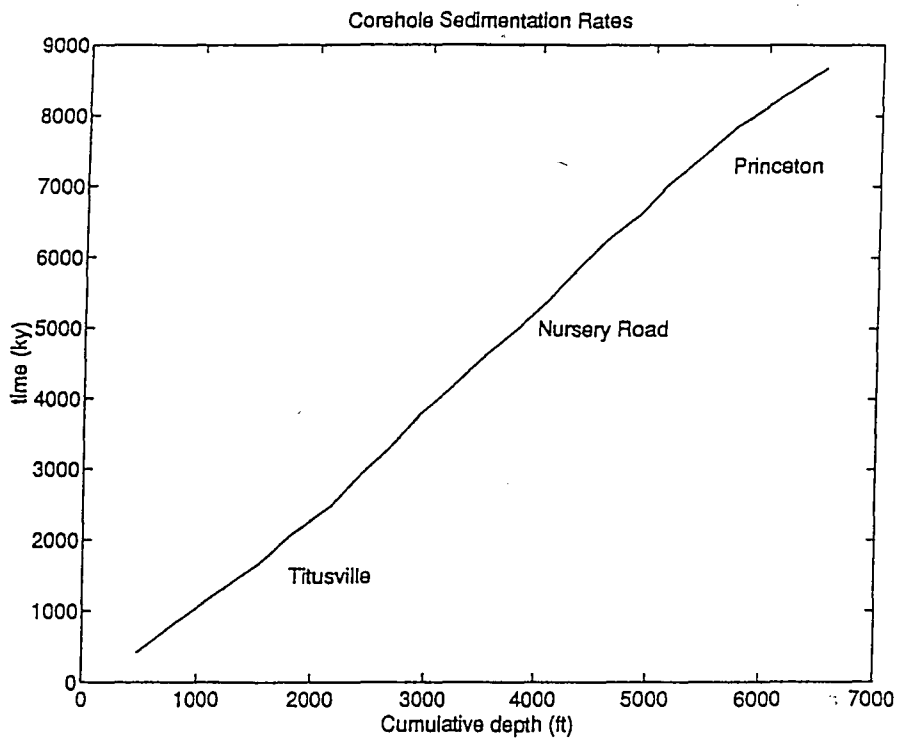

FIGURE 91: A plot of the compound core sedimentaion rates infered from the 413 ky cycles. A linear regression of this compound section yields a sedimentation rate of 0.7316 ft ky (22.3 cm/ky) with an r = 0.966 correlation coefficient.

References

Benson, L.V., D.R. Currey, and R.I. Dorn, 1990, Chronology of expansion and contraction of four Great Basin lake systems during the past 35,000 years: Paleogeography, Paleoclimatology, Paleoecology, v. 78, p. 241.

Berger, A., 1977, Support for the astronomical theory of climate change: Nature, v. 268, p 44-45.

Berger, A., and M.-F. Loutre, 1989, Pre-Quaternary Milankovitch frequencies: Nature, v. 342, p 133.

Cornet, B., and P.E. Olsen, 1985, A summery of the biostratigraphy of the Newark Supergroup of eastern North America, with comments on early Mesozoic provinciality: In R. Weber (ed.) Symposio Sobre Flores del Triasico Tardio st Fitografia y Paleoecologia, Memoria. Proc. II) Latin-American Congress on Paleontology (1984), Instituto de Geologia Universidad Nacional Autonoma de Mexico, p. 67-81.

Costain, J.K., C. Coruh, 1989, Tectonic setting of Triassic half grabens in the Appalachians: Seismic data, acuisition, processing and results, in Tankard, A.J., and H.R. Balkwill, eds., Extentional tectonics and stratigraphy of the North American margins: AAPG Memoir 46, p. 155-174.

Crowley, T.J., and G.R. North, 1991, Paleoclimatology: Oxford University Press, 339 p.

Crowley, T.J., K. Kim, J.G. Mengel, and D.A. Short, 1992, Modeling 100,000-year climate fluctuations in pre-Pleistocene time series: Science v. 255, p 705-707.

Frakes, L.A., and J.E. Francis, 1988, A guide to cold polar climates from high-latitude rafting in the Cretaceous: Nature, v. 333, p 547-549.

Froelich, A.J., and P.E. Olsen, 1984, Newark Supergroup, a revision of the Newark Group in eastern North America: USGS Bulletin 1537A, p. A55-A58.

Hallam, A., and K. Perch-Nielsen, 1990, The biotic record of events in the marine realm at the end of the Cretaceous: calcareous, siliceous, and organic-walled microfossils and macroinvertebrates: Tectonophysics, v.171, p. 347.

Hansen, H.J., 1988, Buried rift basin underlying coastal plain sediments, central Delaware Peninsula, Maryland: Geology, v. 16, p. 729-782.

Kent, D.V., and P.E. Olsen, 1992, The Newark Basin Coring Project, International Geological Congress, Kyoto, Abstracts, v.1, p 30.

Kutzbach, J.E., and F.A. Street-Perrott, 1985, Pangean climates: megamonsoons of the megacontinent: Journal of Geophysical Research, v.94, p.233-244.

Laskar, J., 1990, The chaotic motion of the Solar System: a numerical estimate of the size of the chaotic zones: Icarus, v.88, p 266-291.

Meltzer, A.S., J. Louie, and S. McGeary, 1992, High-resolution seismic imaging of Triassic cyclostratigraphy in the Newark rift basin from vertical seismic profiling: Poster.

Olsen, P.E., 1986, A 40-million-year lake record of Early Mesozoic climatic forcing: Science v.234, p.842-848.

Olsen, P.E., 1988, Continuity of strata in the Newark and Hartford Basins of the Newark Supergroup: in Froelich, A.J., and G.R. Robinson, Jr., eds., Studies of the early Mesozoic basins in the eastern U.S.: USGS Bulletin 1776, p. 6-18.

Olsen, P.E., S. Fowell, B. Cornet, and W.K. Witte, 1991, Calibration of a Late Triassic-Early Jurassic Time Scale Based on Orbitally Induced Lake Cycles, International Geological Congress, Abstracts, 1990, 2, 2-547-548.

Olsen, P.E., and D.V. Kent, 1990, Continental Coring of the Newark Rift: EOS, Transactions of the Americal Geophysical Union, v.71, p 385,394.

Olsen, P.E., D.V. Kent, and B. Cornet, 1991, Thirty million year record of tropical orbitally-forced climate change from continental coring of the Newark early Mesozoic rift basin, Abstract: American Geophysica Union, EOS, v.72, n.17, p.269.

Olsen, P.E., D.V. Kent, B. Cornet, W.K. Witte, and R.W. Schlische, in press, Stratigraphy of the Newark Rift Basin (Early Mesozoic, Eastern North America): Results of the Newark Basin Coring Project, for Geological Society of American Bulletin.

Olsen, P.E., R.W. Schlische, and J.W. Gore, eds., 1989, Tectonic, depositional and paleocological history of early Mesozoic rift basins of eastern North America: Field trip guidebook T351, 28th International Geological Congress, Washington D.C., 174p.

Ratcliffe, N.M., and W.C. Burton, 1985, Fault reactivation models for the origin of the Newark basin and studies related to U.S. eastern seismicity, in G.R. Robinson, Jr., and A.J. Froelich, eds., Proceedings of the second U.S.G.S. workshop on the Early Mesozoic basins of the eastern United States: USGS Circular 946, p.36-45.

Ratcliffe, N.M., W.C. Burton, R.M. D'Angelo, and J.K. Costaine, 1986, Low-angle extentional faulting, reactivated mylonites, and seismic reflection geometry of the Newark basin margin in eastern Pennsylvania: Geology, v.14, p. 766-770.

Reynolds, D.J., 1994, Sedimentary Basin Evolution: Tectonic and Climatic Interaction, Ph.D. Thesis, Columbia University.

Robinson, E.S. and C. Coruh, 1988, Basic Exploration Geophysics: John Wiley & Sons, New York, 561 p.

Rossignol-Strict, M., and N. Planchais, 1983, Climate patterns revealed by pollen and isotope records of a Tyrrhenian sea core: Nature, v. 303, n. 46, p. 413.

Schlische, R.W., 1992, Structural and stratigraphic development of the Newark extentional basin, eastern North America: Evidence for the growth of the basin and its bounding structures, GSA Bulletin, v.104, p. 1246-1263.

Schlische, R.W., and P.E. Olsen, 1988, Structural evolution of the Newark basin, in J.M. Husch, and M.J. Hozic, eds., Geology of the central Newark basin - Field guide and proceedings: Geological Association of New Jersey Fifth Annual Meeting, p. 44-65.

Schlische, R.W., and P.E. Olsen, 1990, Quantitative filling model for continental extentional basins with applications to early Mesozoic refts of eastern North America: Journal of Geology, v.98, p.135-155.

Snedecor, G.W, and W,G, Cochran, 1989, Statistical Methods: Iowa State University Press, Ames, 503 p.

Unger, J.D., 1988, A simple technique for analysis and migration of seismic reflection profiles from the Mesozoic basins of eastern North America, in Froelich, A.J., and G.R. Robinson, Jr., eds., Studies of the early Mesozoic basins in the eastern U.S.: USGS Bulletin 1776, p.229-235.

Van Houten, F.B., 1962, Cyclic sedimentation and the origin of analcime-rich Upper Triassic Lockatong Formation, west-central New Jersey and adjacent Pennsylvania, American Journal of Science, v.260, p 561-576.

Van Houten, F.B., 1964, Cyclic lacstrine sedimentation, Upper Triassic Lockatong formation, central New Jersey and adjacent Pennsylvania: Kansas Geological Survey Bulletin, v.169, p.497-531.

Van Houten, F.B., 1977, Triassic-Jurassic deposits of Morocco and eastern North America: a comparison: AAPG Bulletin, v.61, p.79-99.

Webster, P.J., 1985, The elementary monsoon: In Fein, J.S. and P.L. Stephens (eds.) Monsoons, John Wiley and Sons, p 3-32.

Vita

Gregory S Baker was born June 27, 1970, in Philadelphia, Pennsylvania to Roger William Baker, Jr., and Sylvia Dornblaser Baker. He recieved his B.S. degree in Geological Sciences from Lehigh University in 1992, graduating with departmental honors and receiving the D. Foster Hewitt Award for excellence in geology. He spent his Junior year abroad studying geology at the University of Edinburgh, Scotland. His Senior undergraduate Thesis delt with paleomagnetic investigations of Fransiscan rocks at Point San Pedro, CA. The summer after receiving his B.S. degree, he spent six weeks in southeastern Missouri working with the U.S. Geological Survey, and co-authored a GSA abstract in 1992 entitled *Deformation associated with the Ste. Genevieve Fault Zone and Mid-continent tectonics.* During his graduate tenure at Lehigh, Gregory was a teaching assistant for Environmental Geology, Geology for Engineers, Introduction to Geophysics, and Evolution of Life through Time. After receiving his M.S. degree in 1994, Gregory will assist at Lehigh University's Summer Geology Field Camp.

END

OF

TITLE